1. AGENCY USE ONLY (Leave Blank)	2. REPORT DATE	3. REPORT TYPE AND DATES COVERED
	29 JUNE 1992	Ph.D. DISSERTATION JUNE 1989 - JUNE 1992

4. TITLE AND SUBTITLE

OPTICAL OVERSAMPLED ANALOG-TO-DIGITAL CONVERSION

5. FUNDING NUMBERS

(2)

6. AUTHOR(S)

BARRY L. SHOOP

7. PERFORMING ORGANIZATION NAME(S) AND ADDRESS(ES)

STANFORD UNIVERSITY
DEPARTMENT OF ELECTRICAL ENGINEERING
INFORMATION SYSTEMS LABORATORY
STANFORD, CA 94305-4055

8. PERFORMING ORGANIZATION REPORT NUMBER

9. SPONSORING/MONITORING AGENCY NAME(S) AND ADDRESS(ES)

U.S. ARMY
UNITED STATES MILITARY ACADEMY
WEST POINT, NY 10996

10. SPONSORING/MONITORING AGENCY REPORT NUMBER

11. SUPPLEMENTARY NOTES

12a. DISTRIBUTION/AVAILABILITY STATEMENT

UNLIMITED

12b. DISTRIBUTION CODE

13. ABSTRACT (Maximum 200 words)

SEE ATTACHED

14. SUBJECT TERMS	15. NUMBER OF PAGES
OPTICAL INFORMATION PROCESSING, ANALOG-TO-DIGITAL CONVERSION, OVERSAMPLED ANALOG-TO-DIGITAL CONVERSION	129
	16. PRICE CODE

17. SECURITY CLASSIFICATION OF REPORT	18. SECURITY CLASSIFICATION OF THIS PAGE	19. SECURITY CLASSIFICATION OF ABSTRACT	20. LIMITATION OF ABSTRACT
U	U	U	UNLIMITED

OPTICAL OVERSAMPLED ANALOG-TO-DIGITAL CONVERSION

A DISSERTATION
SUBMITTED TO THE DEPARTMENT OF ELECTRICAL ENGINEERING
AND THE COMMITTEE ON GRADUATE STUDIES
OF STANFORD UNIVERSITY
IN PARTIAL FULFILLMENT OF THE REQUIREMENTS
FOR THE DEGREE OF
DOCTOR OF PHILOSOPHY

By
Barry L. Shoop
June 1992

I certify that I have read this thesis and that in my opinion it is fully adequate, in scope and in quality, as a dissertation for the degree of Doctor of Philosophy.

Joseph W. Goodman
(Principal Advisor)

I certify that I have read this thesis and that in my opinion it is fully adequate, in scope and in quality, as a dissertation for the degree of Doctor of Philosophy.

Lambertus Hesselink

I certify that I have read this thesis and that in my opinion it is fully adequate, in scope and in quality, as a dissertation for the degree of Doctor of Philosophy.

Bruce A. Wooley

Approved for the University Committee on Graduate Studies:

To my family who mean everything to me,
especially

My wife Linda,
my son Brandon, my daughter Aubrey,
and my parents
Roy and Ruth Shoop

Abstract

A NEW APPROACH TO OPTICAL ANALOG-TO-DIGITAL (A/D) CONVERSION based on oversampling and error diffusion coding techniques is proposed. This new approach combines the high resolution capabilities of classical oversampled A/D conversion with the high speed of optical processing technology to extend the resolution and conversion rates beyond those currently possible with other electronic or optical converters. The optical approach is device independent, requiring only optical thresholding, subtraction, and digital logic for implementation. The underlying concept is to trade bandwidth for improved amplitude resolution using advanced signal processing techniques.

This new approach to optical A/D conversion differs from classical Nyquist rate optical A/D conversion in that each signal sample is not necessarily quantized to the closest reconstruction level. The analog input signal is first optically sampled at a frequency much greater than the Nyquist frequency and is then quantized by a modulator which incorporates one-bit quantizers and linear filters in a negative feedback architecture for the purpose of reducing the quantization noise within the signal baseband. This in-band noise reduction is accomplished by spectrally shaping the quantization noise, forcing most of the noise power to frequencies above the signal's cutoff frequency. The output of the modulator, which is a high-rate, single-bit digital optical word, is subsequently processed by a digital decimation filter which removes the out-of-band noise and generates a high resolution digital approximation to the input analog signal at the signal's Nyquist rate.

In this dissertation, the theory, design, analysis, and implementation of an optical oversampled A/D converter are addressed. The theory of oversampled A/D

conversion is first presented and then extended to the design of an optical implementation of an oversampled converter. Next, sources of error specific to the optical architecture are investigated to determine their impact on overall converter performance. Proof-of-concept operation is demonstrated through the design, implementation and evaluation of a first-order noninterferometric optical modulator using multiple quantum well devices. Finally, multidimensional extensions of this one-dimensional optical approach are presented and applications and advantages are discussed.

Acknowledgements

I AM DEEPLY INDEBTED TO THE MANY PEOPLE WHO HAVE MADE IMPORTANT contributions to this research and who have made my experience at Stanford both enjoyable and rewarding. In particular I am grateful to Professor Joseph W. Goodman, for his guidance and encouragement throughout the research that preceded this dissertation. His approach to research and his intuition about complicated issues, his insistence on high-quality research, and his willingness to allow me the freedom to define and direct this research have all made my tenure under him educational and rewarding. I am thankful to Professor Robert Gray for many helpful discussions on the subject of quantization noise spectra and for serving as a member of my orals committee. I am also thankful to Professor David Bloom for serving as the chairman of my oral examination committee. I am extremely appreciative of Professors Lambertus Hesselink and Bruce Wooley for their expeditious review of and valuable comments to this manuscript.

I am indebted to Professor James Harris, Jr. for several discussions on the theory of GaAs semiconductor devices and the use of his laboratory where the experimental demonstrations were conducted. I owe special thanks to Dr. Bardia Pezeshki for many stimulating discussions on the theory and operation of the asymmetric Fabry-Perot multiple quantum well modulators and for help in the experimental demonstrations. Louis Williams deserves special recognition for numerous discussions on conventional oversampled A/D conversion techniques and for providing the custom simulation package MIDAS which was used to verify analytic results throughout this thesis. Likewise, Sang Ju Park provided a critical review of the quantization noise analysis presented in Chapter 4.

I would also like to thank Professor John Cioffi for his early guidance and several candid discussions on graduate education and the Stanford educational experience.

The members of Professor Goodman's research group and my other colleagues at Stanford deserve special mention for without them my experience at Stanford surely would have been diminished. To Ireena, Rich, Bob and Bill with whom I ran and shared an occasional *café-mocha*. Special thanks also go to Ireena for proofreading the original manuscript and providing indispensable comments. To Takashi for the transfer characteristic curves on page 39, and the many discussions concerning quantum well modulators as well as general American-Japanese relations. And to Karin, Paul, Haldun, Mike, Jane, and Bob for their camaraderie.

There are others, not affiliated with Stanford, who also contributed to my educational experience and this research. Dr. D. A. B. Miller of AT&T Bell Labs, with whom I had numerous helpful discussions concerning the basic theory of the quantum confined Stark effect and the operation of the self electrooptic effect devices. Professor Demetri Psaltis of Cal Tech took special interest in and encouraged my pursuit of the multidimensional extensions of the basic oversampled converter.

I am very grateful to the members of the Memorial Church Choir and particularly to the Choir Director, Gregory Wait. Through my participation in this organization I was able to include in my educational experience *left-half brain* education and expand my appreciation of early choral music, initially much to my reluctance.

I am appreciative to the United States Department of the Army and the United States Military Academy at West Point, New York, for providing the funding which made this portion of my graduate education possible.

Finally and most of all, I owe my family a great debt of gratitude. To my best friend and wife, Linda, whose continuous love and encouragement enabled me to confront the many challenges associated with graduate student life. To my son Brandon and my daughter Aubrey who gave me a new perspective on *Life* and taught me the true meaning of family (and sleep deprivation!). And finally to my parents Roy and Ruth Shoop who instilled in me from an early age the importance of God, family, and education.

Stanford, California
June, 1992
BARRY L. SHOOP

This dissertation was typeset by the author using TEX[1] and LATEX[2].

Contents

List of Figures

Chapter 1

Introduction

OPTICS HAS LONG HELD THE PROMISE OF HIGH-SPEED, HIGH-THROUGHPUT parallel information processing. The focus of its early applications was on analog signal processing techniques such as the optical Fourier transform, matrix-vector processors, and correlators. During this period, optics was used almost exclusively for front-end, pre-processing of wide-bandwidth, high-speed analog signals which were subsequently digitally processed using electronic techniques. Digital signal processing provides higher resolution, improved flexibility and functionality, and increased noise immunity over its analog counterparts and therefore is the preferred method for accurate signal processing. Since the majority of signals encountered in nature are continuous in both time and amplitude, the analog-to-digital (A/D) interface is generally considered to be the most critical part of the overall signal acquisition and processing system. Because of the difficulty in achieving high-resolution and high-speed A/D converters, this A/D interface has been and continues to be a barrier to the realization of high-speed, high-throughput systems. Until recently, digital optical information processing was believed to be a technology whose time had not yet come, but someday might. Since the early 1980's, however, optical device technology has enjoyed tremendous progress as a result of technological breakthroughs which have made possible numerous practical optical devices, some of which produce nonlinear effects, the requisite function for digital processing. As the optics community embraces digital optical computing and the

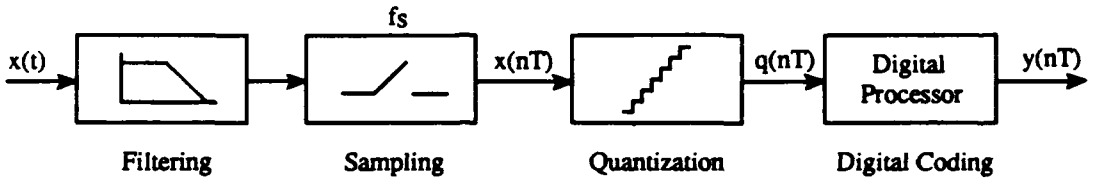

Figure 1.1: Typical analog-to-digital converter block diagram.

electronics industry continues to develop smaller and faster digital processors, the need for a high-speed A/D interface becomes increasingly important. The focus of this research is to investigate the use of optical techniques to improve the performance of this interface and thereby benefit not only electronic but also future optical digital signal processing systems.

1.1 Background and Motivation

A/D conversion is the process by which a continuous-time, continuous-amplitude signal is converted to a discrete-time, discrete-amplitude or digital signal. This process typically employs the four functions depicted in Figure 1.1. The analog input signal $x(t)$ is first bandlimited to the range $0 \leq f_x \leq f_B$ (Hz) by an analog filter to ensure protection against aliasing that could occur during the ensuing sampling operation. The sampling operation in a conventional Nyquist rate A/D converter is chosen to satisfy the minimum Nyquist criterion: $f_S = f_N = 2f_B$, where f_S is the sampling frequency, f_N is the Nyquist frequency, and f_B is the constrained signal bandwidth. The output from the sampler is $x_n \equiv x(nT_S)$ where T_S is the uniform sampling period $T_S = 1/f_S$. The scalar quantization process maps each continuous-amplitude input x_n to one value in a discrete-amplitude ensemble q_n. Based on the results of this mapping, the digital processor generates the digital code of the level that most closely approximates the input signal level.

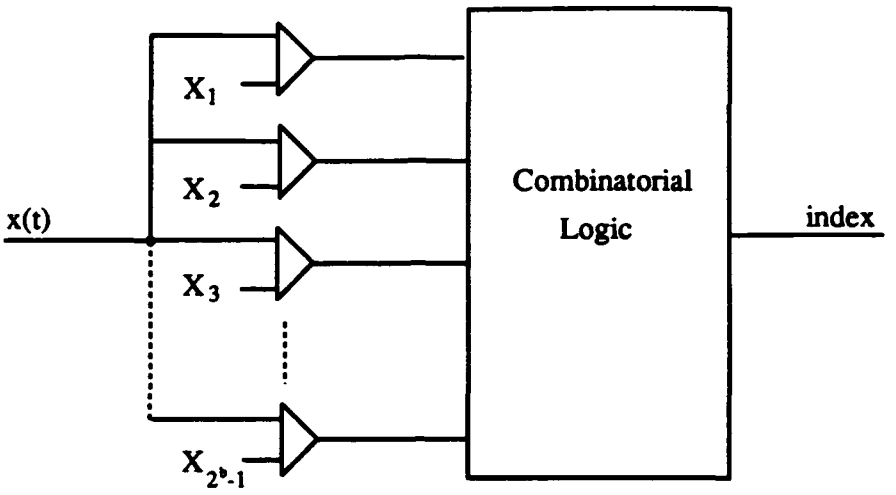

Figure 1.2: Structure of a fully-parallel or flash quantizer.

1.1.1 Nyquist Rate Conversion

There are several different types of uniform scalar quantizer structures available for A/D conversion. In a fully-parallel or *flash* quantizer, the analog input to the quantizer is simultaneously compared to $2^b - 1$ different reference levels, where b is the resolution of the quantizer in bits. Figure 1.2 shows the structure of a fully-parallel quantizer. Here, X_k, $k = 1, 2, ...2^b - 1$ are the reference levels associated with the $2^b - 1$ different comparators. Although achieving the fastest conversion rates possible [3, 4], these converters are exponentially complex, with the number of comparators doubling for each additional bit of resolution. For example, a high-resolution 16 bit parallel A/D converter requires $2^{16} - 1 = 65,535$ different reference levels. For an input with a dynamic range of 0 to 5 volts, this requires that adjacent reference levels differ by only 76 μV. This precision exceeds the capability of current very large scale integration (VLSI) processing. Although laser trimming and self-calibration techniques can be employed to extend the resolution of these converters [5], these approaches result in increased fabrication complexity and cost. For these reasons, flash converters are limited to approximately 8 to 10 bits resolution and are therefore not generally suitable for high-resolution A/D conversion.

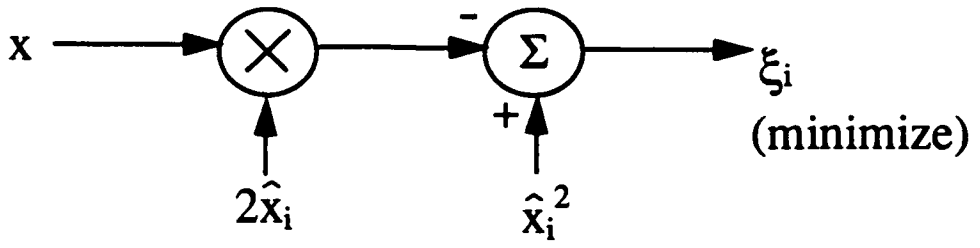

Figure 1.3: Structure of a full-search quantizer.

A converter which can produce medium resolution on the order of 12 to 14 bits is the *half-flash* converter, also called a subranging, or two-pass, converter. Here, the overall resolution is broken down into two, lower resolution conversions, each of which is performed by a flash converter. Higher resolution can be achieved with this technique, but at the cost of conversion speed.

The *full-search* quantizer is similar to the flash converter but instead of performing a direct comparison with $2^b - 1$ different threshold levels, uses an optimization routine to determine the reference level closest to the input. Figure 1.3 shows a schematic of the full-search operation. In this case, the algorithm uses the inner products $(x - \hat{x}_i)^2 = x^2 - 2x\hat{x}_i + \hat{x}_i^2$ and therefore, given the input x, finds the reference level $\hat{x}_i$ that minimizes $(\hat{x}_i^2 - 2x\hat{x}_i)$ for all i. This type of quantizer requires $2^b - 1$ products and $2^b - 1$ comparisons for each quantization decision.

One method of further reducing the complexity of the converter is to use a *successive approximation* quantizer. In this approach, a tree-structured search routine is used which successively improves the digital approximation of the analog input signal. Figure 1.4 shows the operations associated with the successive approximation routine. Figure 1.4(a) shows the tree-structured search routine for a 3-bit quantizer. The x_i, $i = 1, 2, 3$ inside the boxes represent the reference levels, and the digital bits above each path represent the bit assigned by each decision. Figure 1.4(b) shows the steps associated with the successive approximation approach. Here, the input is first compared to the reference level x_3 and found to be greater. Therefore the first bit assigned is a '1'. During step 2, the input is determined to be less than x_5 and therefore a '0' is assigned. This process then continues until the

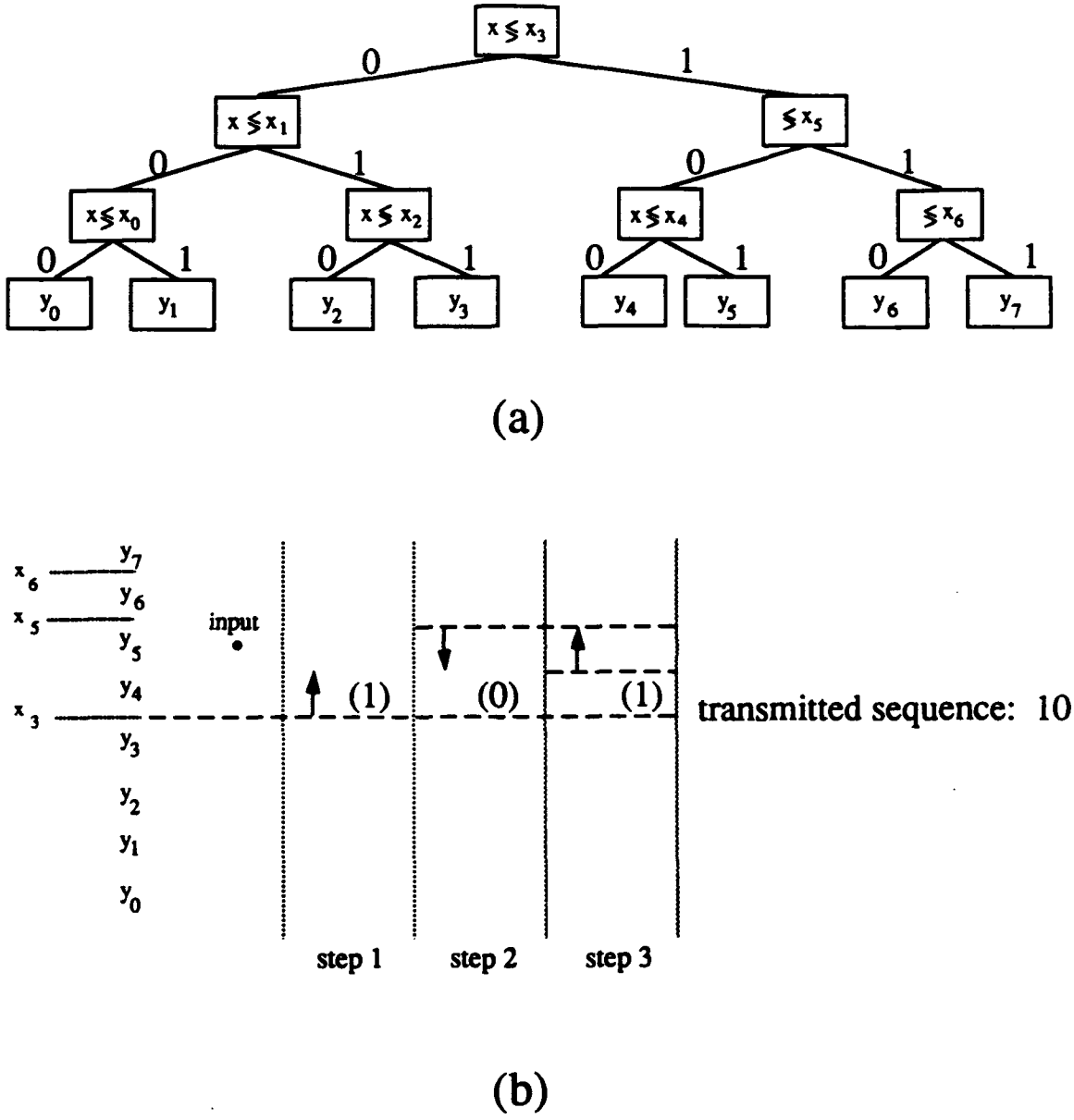

Figure 1.4: Structure of a successive approximation quantizer (a) tree-structured search routine for a 3-bit quantizer (b) steps associated with the successive approximation quantization.

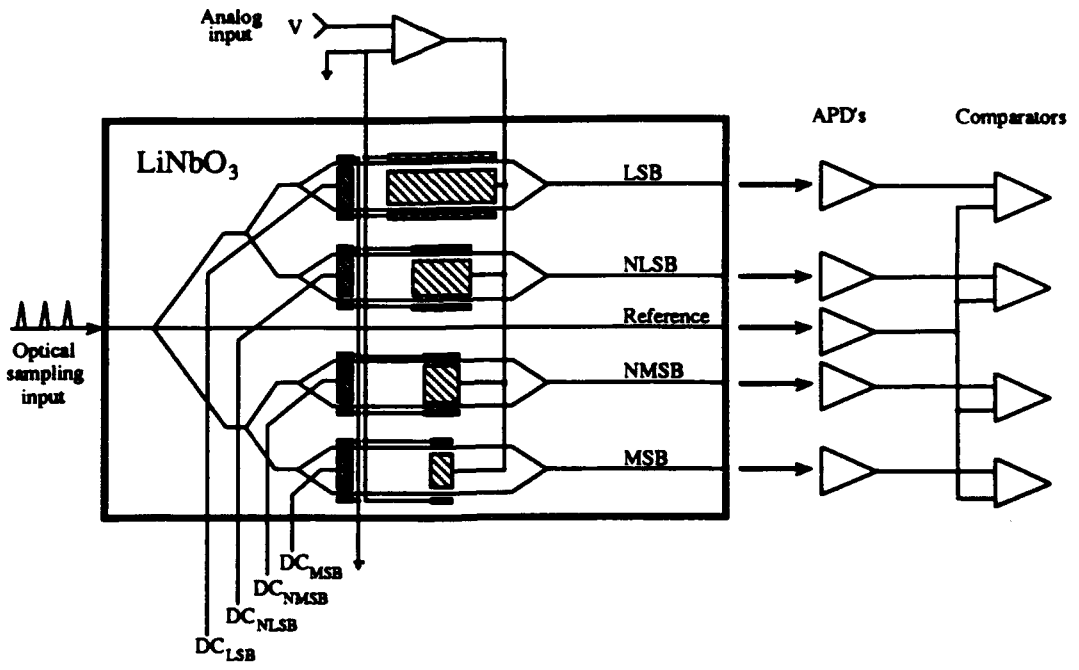

Figure 1.5: Schematic diagram of a 4-bit electrooptic A/D converter.

full resolution of the converter is achieved. This type of converter is slower than the flash converter, but requires less hardware for implementation. The successive approximation quantizer also achieves linear hardware complexity.

In this section, we have presented a brief overview of some of the techniques used for A/D conversion and their associated advantages and disadvantages. Next, we will discuss some of the optical methods that have been used to implement A/D conversion.

1.1.2 Optical A/D Conversion

Probably the most successful optical A/D conversion technique was developed by Taylor in 1975 [6]. He recognized that the periodicity of the output of an interferometric electrooptic modulator with applied voltage was homomorphic to the periodic variation of a binary representation of an analog quantity. A 4-bit implementation of this concept is shown in Figure 1.5 [7].

The basic optical component used in this architecture is a channel waveguide

version of a Mach-Zehnder interferometric modulator. The interferometer consists of an electrooptic crystal containing a single-mode input optical waveguide which branches at a 'Y' to split the optical power into two equal components. The light in the two paths then travels an equal distance before recombining at the second 'Y' and exiting the crystal. In most cases of practical interest, the crystal is either $LiTaO_3$ or $LiNbO_3$. The input analog voltage is applied to one arm of the interferometer through the coplanar electrodes shown in the figure. In the absence of an applied field, the light from the two paths recombines in phase and produce a maximum in the output intensity. With an electric field applied to the electrode, the phase velocity of the light propagating in that arm is changed as a result of the linear electrooptic effect. It is easily shown that the output intensity of a single interferometer varies as

$$I = I_0 \cos^2 \left(\frac{\phi}{2} + \frac{\psi}{2} \right), \tag{1.1}$$

where ψ is the static phase difference between the two paths and ϕ is the electrooptic phase difference given by

$$\phi = 2\pi L \left(\frac{\Delta n}{\lambda} \right) = kLV. \tag{1.2}$$

Here, Δn is the refractive index change, V is the applied voltage, L is the modulator length, and k is a constant which depends on the electrooptic parameters of the crystal, the electrode spacing, and optical wavelength.

In Figure 1.5, the analog input signal V is applied in parallel to one arm of each of the four modulators, one for each bit of resolution. The optical output from each modulator is detected by an avalanche photodiode (APD) which converts the optical signal to an electronic signal and also provides amplification. The electronic signal from each modulator is then compared to a reference signal, obtained from the common light source. The output of each comparator is either a binary '1' or '0', depending on whether the modulator output intensity is greater than or less than $I_0/2$, respectively. The output of the top modulator represents the least significant bit (LSB) in the digital word and that of the bottom modulator is the most significant bit (MSB). The output intensity, the threshold, and the corresponding binary representation for each modulator are shown in Figure 1.6. The Gray-code

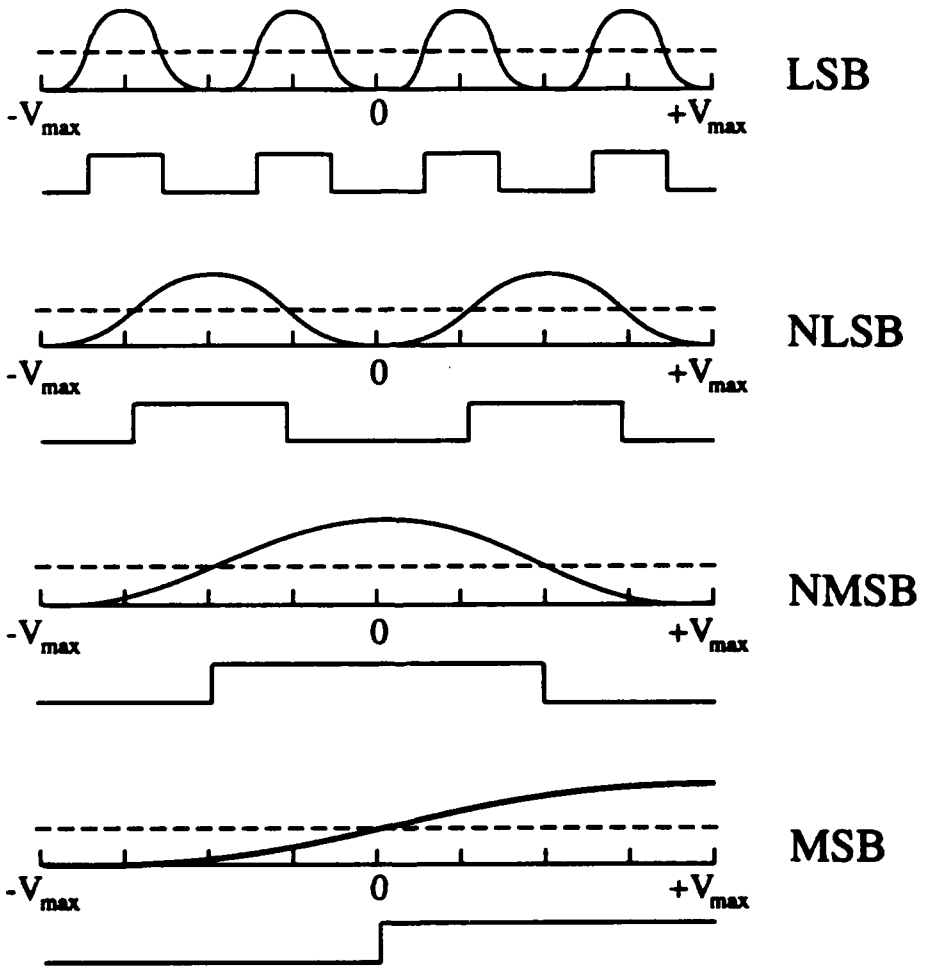

Figure 1.6: Intensity versus voltage for a 4-bit electrooptic A/D converter with a Gray-code output.

representation in Figure 1.6 is achieved by controlling the static phase difference in each modulator by applying the appropriate dc biases shown in Figure 1.5.

This electrooptic A/D converter provides several distinct advantages. Like the successive approximation converter discussed in Section 1.1.1, this optical converter is linear in complexity. Another important advantage is the decoupling of the analog sampled signal from the optical sampling signal. This eliminates the distortion effects common to diode-bridge sampling circuits which tend to couple the sampling signal into the converter circuitry. A limitation of this type of converter is that each additional bit of resolution requires a doubling of the electrode length of the least significant bit modulator. In $LiNbO_3$, this produces a transit-time limitation on performance of approximately 6 bits at 1 GHz. Other electrooptic crystals exist which produce larger refractive index changes and therefore could improve the performance of this transit-time limit. However, most of these crystals also have larger loss mechanisms and therefore would produce loss-limited performance instead. The development of crystals with large electrooptic coefficients and low losses is currently an active research area.

Other types of optical A/D converters have also been investigated, but with much less success than Taylor's electrooptic converter. Most were limited by speed, complexity, or resolution and therefore did not warrant further investigation. For example, Tsunoda proposed optical A/D conversion based on a matrix-multiplication formalism [8]. In this implementation, an astigmatic optical processor [9] was used with the electronic analog input signal driving an optical beam deflector. This method of optical A/D conversion was limited by the speed capacity of the deflector, $C = K/\tau$, where K is the number of resolvable spots addressable and τ is the time required for random access to a specific location. Other methods of optical A/D conversion can be found in [10, 11, 12, 13, 14, 15].

1.1.3 Oversampled A/D Converters

From the above background we can make some general observations regarding Nyquist rate electronic and electrooptic A/D converters. The performance of Nyquist

rate electronic A/D converters continues to improve as new, more advanced processing techniques improve circuit integration and thereby increase circuit speed. Their performance, however, is ultimately limited by the number and spacing of the reference levels that can be generated and resolved. Conventional integrated electrooptic A/D converters have typically used guided-wave structures which are either loss or transit-time limited in performance.

A technique which has become popular in the audio industry is that of oversampled A/D conversion or oversampled sigma-delta ($\Sigma\Delta$) modulation. The basic architecture of an oversampled A/D converter, which consists of a quantizer, two differencing nodes, and a single discrete-time delay element, was first introduced in 1960 by C. C. Cutler [16]. In this patent, Cutler described this system as a "quantizer with a single step of error compensation". Inose and Yasuda [17] later introduced a slightly different form of this architecture which contained a quantizer, one differencing node, and a discrete-time integrator. They called their architecture a "Delta-Sigma" modulator. The modern popularity, much of the original analysis, and the name "Sigma-Delta" modulation can be directly attributed to Candy and his colleagues [18, 19, 20, 21]. A fully equivalent A/D conversion technique which uses the same architecture as that proposed by Cutler, called error diffusion coding, was later developed by Floyd and Steinberg [22] for use in the field of image halftoning. In this case, the digital representation of the input image is bilevel. These two techniques have recently been shown to obey a common, underlying theoretical basis [23], which we will use in developing our optical architectures.

Oversampled A/D converters provide several distinct implementation advantages which account for their recent popularity. Oversampled converters use low resolution quantizers which makes them more robust against circuit imperfections than conventional Nyquist rate flash or successive approximation converters, since circuit errors can be made small compared to the quantizer error. Also, by definition, the sampling frequency is large relative to the Nyquist frequency of the sampled signal and therefore the complexity of the anti-aliasing filter used to bandlimit the input signal can be reduced. For electronic applications, these converters also lend themselves to small VLSI circuit area.

1.2 Scope of This Dissertation

The focus of this research is to improve the performance of the A/D interface by using optical technology and oversampling techniques. Once the fundamental concepts have been developed, we will analyze the operation and performance, and demonstrate proof-of-concept operation of the oversampled optical A/D converter. As a result of this research, we hope to introduce a new method of optical A/D conversion based on oversampling techniques which can extend the resolution and conversion rates beyond those currently possible with other electronic or electrooptic A/D conversion techniques.

In Chapter 2, the basic concepts and underlying theory of oversampled A/D conversion are first introduced. The operation and analysis of the modulator and digital postprocessor, the two key components of any oversampled A/D converter, are the focus of this chapter. Several different classifications of oversampled modulators are introduced and contrasted according to the way each spectrally shapes the quantization noise and input analog signal. The operation of the modulator is then described according to a set of difference equations, and the concept of spectral noise shaping is formalized. The digital postprocessor, which consists of a digital low pass filter and a decimator, is then described and performance estimates are developed for the overall oversampled A/D converter in terms of signal-to-quantization-noise ratio (SQNR).

The theory of operation of one particular optical device, the multiple quantum well (MQW) modulator, and its application to several different optical oversampled converter architectures is the topic of Chapter 3. Here, we describe how the MQW modulator can be used to implement the optical functional requirements necessary for both the modulator and digital postprocessor. Speed and energy requirements of the constituent optical devices and the overall converter are also examined.

In Chapter 4, we investigate sources of error in the oversampled error diffusion modulator resulting from linear arithmetic errors, non-white quantization noise characteristics, and stage-to-stage matching tolerances. Converter performance degradations are quantified in terms of fractional reduction in the SQNR.

An experimental demonstration of one specific realization of a noninterferometric optical oversampled modulator using MQW modulators is presented in Chapter 5. The proof-of-concept operation of this optical modulator is compared to the characteristics developed in Chapters 3 and 4, and some general comments about the operation and performance of the optical oversampled modulator are made.

One of the benefits that optics provides to the oversampled A/D converter implementation is parallel processing. In Chapter 6, we present multidimensional optical extensions of the basic 1-D temporal optical error diffusion architecture presented in Chapter 3. In this case, 2-D temporal, 2-D spatial, and 3-D temporal and spatial error diffusion architectures are presented and the applications and specific advantages associated with each are discussed.

Finally, in Chapter 7 we conclude by summarizing the results of this research, presenting specific contributions, and proposing open issues and future areas of investigation.

Chapter 2

Oversampled A/D Conversion

OVERSAMPLED A/D CONVERSION RELIES ON A ONE-DIMENSIONAL, TEMporal form of error diffusion coding, whereby a large error associated with a single sample is *diffused* over many subsequent samples. In oversampled A/D converters, the error to be diffused is generated by a low resolution quantizer, and the diffusion is implemented by embedding the quantizer and a linear filter in a feedback architecture. Figure 2.1 shows a generalized block diagram of an oversampled A/D converter. The analog signal $x(t)$ is first bandlimited to the range $0 \leq f_x \leq f_B$ (Hz) by an anti-aliasing filter and is then sampled at a rate $f_S \gg f_N$, where f_S is the sampling frequency, $f_N = 2f_x$ is the Nyquist frequency of the sampled signal, and $f_B \leq f_S/2$ is the constrained signal bandwidth . The output of the sampler is then fed to the modulator which provides coarse amplitude quantization

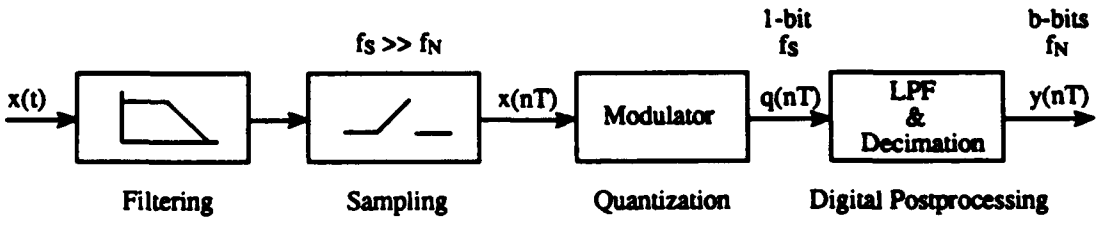

Figure 2.1: Generalized block diagram of an oversampled A/D converter.

and spectral shaping of the quantization noise. The digital postprocessor, which consists of a digital low pass filter (LPF) and a decimator, removes the quantization noise which was spectrally shaped by the modulator, provides anti-aliasing protection, and reduces the rate to the original sampled signal's Nyquist rate by trading word rate for word length.

The recent popularity of oversampled A/D converters can be attributed primarily to a maturing of silicon processing technology. VLSI CMOS and BiCMOS processes are capable of producing sub-micron integration which, in turn, provides the capability for higher speed operation. The majority of oversampled A/D conversion applications to date have been in the audio industry, where the analog input signal bandwidth is small compared to the operating speeds of the VLSI circuits. One of the obvious advantages of oversampled A/D converters is a relaxing of the requirements on the anti-aliasing filter used to bandlimit the analog input signal. Since the sampling frequency is much higher than the Nyquist frequency of the input signal, the cutoff characteristics of the anti-aliasing filter are not as severe as those used with conventional Nyquist rate converters, and therefore the filter complexity and consequently cost are reduced. Another advantage is that high resolution A/D conversion can be achieved without precision component matching or self-calibration techniques. Oversampled A/D converters also provide scalable resolution; the amplitude resolution of the oversampled converter can be increased *without* increasing the number of levels of the quantizer, by simply including more samples in the local averaging process of the postprocessor, making higher resolution possible without increased converter complexity.

We now proceed to discuss the theory and operation of the oversampled A/D modulator and digital postprocessor.

2.1 The Modulator

The function of the modulator in an oversampled A/D converter is to quantize the analog input signal and reduce the quantization noise within the signal baseband. This is accomplished through the use of a low-resolution quantizer, oversampling,

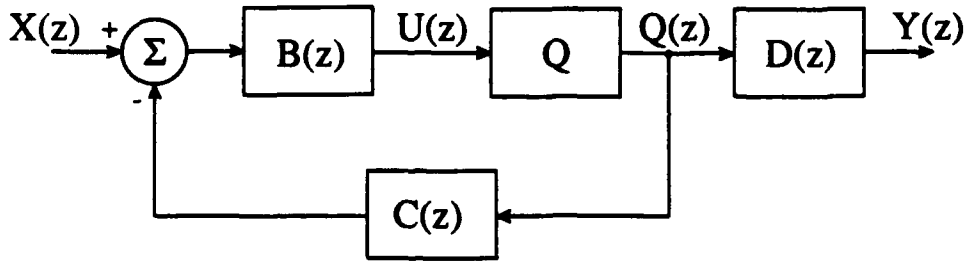

Figure 2.2: General linear feedback coder and decoder.

negative feedback, and linear filtering.

2.1.1 Classification

There are two general coding (modulation) techniques associated with oversampling modulators which are classified according to the location of the linear filters within the feedback structure and whether or not the signal is spectrally altered by the filters: predictive and noise shaping coding. A description of these coding techniques follows [24] and can be extended to include $\Sigma\Delta$ modulation, interpolative coding, and combinations of linear predictive and noise shaping coding. If the quantizer is modeled as an additive noise source with the noise being added to the input sample, and linear transform theory is applied, the general linear feedback coder and decoder structure has the form shown in Figure 2.2. Here Q is the quantizer, and $B(z), C(z)$, and $D(z)$ represent the z-transforms of the feedforward, feedback, and decoding filters, respectively. $X(z), U(z), Q(z)$, and $Y(z)$ represent the z-transforms of the input sample sequence x_n, the quantizer input sample sequence u_n, the coder output sample sequence q_n, and the system output sample sequence y_n, respectively. The output of the coder can be described by

$$Q(z) = \frac{B(z)X(z) + E(z)}{1 + B(z)C(z)}, \tag{2.1}$$

where $E(z)$ is the z-transform of the quantizer error sequence $\varepsilon_n = q_n - u_n$. The purpose of the decoder is to compensate for any distortion of the signal introduced

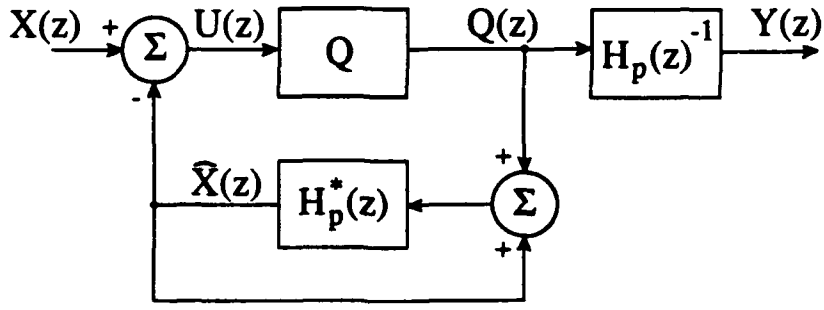

Figure 2.3: General predictive coder and decoder.

by the coder and is therefore necessarily described by

$$D(z) = \frac{1 + B(z)C(z)}{B(z)}. \tag{2.2}$$

The output of the overall coder-decoder system is then

$$Y(z) = D(z)Q(z) = X(z) + \frac{E(z)}{B(z)}. \tag{2.3}$$

Predictive coders reduce the dynamic range of the quantizer input by subtracting an estimate of the input $\hat{x}_n$ from the input sample sequence x_n. The quantizer step size is then adjusted to this new, reduced range and therefore the magnitude of the quantizer error is directly reduced. As a result of this process, the input signal is spectrally shaped by this differencing operation. For the general class of predictive coders, the z-transforms satisfy the following relations

$$Q(z) = H_p(z)\left[X(z) + E(z)\right], \tag{2.4}$$

where

$$H_p(z) = \frac{1}{1 + C(z)} \quad \text{and} \quad D(z) = 1 + C(z). \tag{2.5}$$

Figure 2.3 shows a block diagram of a general predictive coder and decoder. Here $H_p^*(z) = 1 - H_p(z) = C(z)/1 + C(z)$. Delta modulation [25] and differential

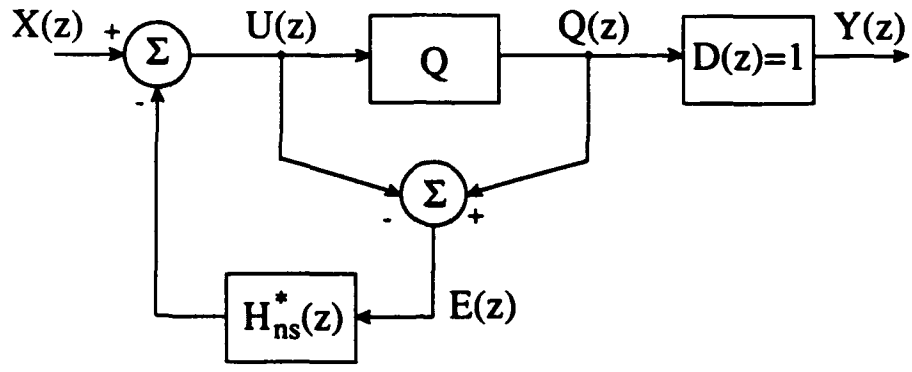

Figure 2.4: General noise shaping or error diffusion coder and decoder.

pulse code modulation (DPCM) are the most common forms of predictive coding. In delta modulation, $H_p^*(z) = z^{-1}$, the coder differentiates the input signal x_n, $D(z) = 1/1 - z^{-1}$, and therefore the decoder integrates the coder output sequence q_n. Consequently, y_n degrades due to enhanced noise and channel error accumulation. For rapidly varying input signals, predictive coders are also known to exhibit slope overload errors.

Noise shaping or error diffusion coding does not reduce the magnitude of the quantizer noise directly, but instead spectrally shapes the noise such that the noise that falls within the signal baseband is reduced and forced to higher frequencies where it can be subsequently removed through low pass filtering. The general class of noise shaping coders satisfy the relation

$$Q(z) = X(z) + H_{ns}(z)E(z), \tag{2.6}$$

where

$$H_{ns}(z) = 1 - C(z) \quad \text{and} \quad D(z) = 1. \tag{2.7}$$

It is clear from Equations (2.6) and (2.7) that no spectral shaping of the signal occurs with noise shaping coding. The block diagram of the general noise shaping coder and decoder is shown in Figure 2.4. Here $H_{ns}^*(z) = 1 - H_{ns}(z) = C(z)$. Interpolative coding and $\Sigma\Delta$ modulation are both examples of noise shaping coding.

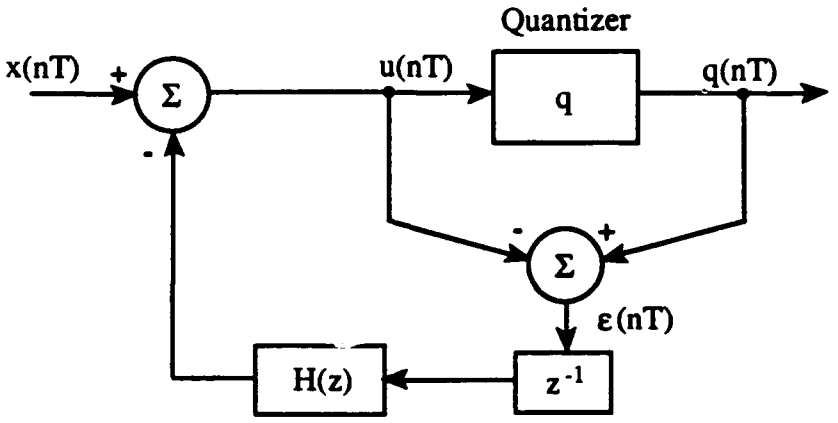

Figure 2.5: Block diagram of recursive error diffusion modulator.

The single-loop $\Sigma\Delta$ modulator can be considered a special case of an interpolative modulator with the linear filter $H_{\Sigma\Delta}(z) = 1/H^*_{ns}(z)$ specialized to an ideal infinite impulse response (IIR) filter and implemented in the feedforward path of the coder. The error diffusion coding architecture shares a homomorphic relationship with the $\Sigma\Delta$ architecture (see Appendix A for details), but implements a finite impulse response (FIR) filter $H^*_{ns}(z)$ in the feedback path making it preferable for optical implementation. We will focus on the operation and application of the error diffusion coding architecture exclusively throughout the remainder of this dissertation and will therefore drop the noise shaping subscript on the feedback filter transfer function. We will also explicitly include a unit delay element from $H(z)$ to represent the time delay associated with the quantization process.

2.1.2 Operation

Figure 2.5 shows the block diagram of a generalized recursive error diffusion modulator. Here, $H(z)$ represents the z-transform of a causal, unity dc gain filter and z^{-1} is a unit sample delay. The unity gain criterion is necessary to ensure complete diffusion of the error signal ϵ_n. In the simplest case of first-order error diffusion, $H(z) = 1$, and the architecture of Figure 2.5 can be equivalently represented as the

traditional single-loop $\Sigma\Delta$ modulator [18].

The input to the modulator, x_n, is generated by oversampling the analog input signal $x(t)$ at $f_S \gg f_N$. The input is assumed to be in the range $x_n \in [-b, b)$, where we use the usual definition of the half-open interval $[a, b) = \{x : a \leq x < b\}$. The difference between the modulator input and a delayed version of the quantizer error, ε_{n-1}, is quantized by the binary quantizer, where the quantizer error is defined as the difference between the output and the input to the quantizer, $\varepsilon_n \equiv q(u_n) - u_n$. For $H(z) = 1$ the nonlinear difference equation describing this modulator is

$$u_n = x_n - \varepsilon_{n-1} = x_n + u_{n-1} - q(u_{n-1}); \;\; n = 1, 2, \ldots \tag{2.8}$$

The memoryless uniform binary quantizer assigns the digital output level according to

$$q(u_n) = \begin{cases} +\frac{\Delta}{2} & \text{if } u_n \geq 0 \\ \\ -\frac{\Delta}{2} & \text{otherwise} \end{cases} \tag{2.9}$$

where Δ is the quantizer step size and u_n is the quantizer input. It is easy to show that choosing $\Delta = 2b$ ensures that the quantizer does not overload as long as the input remains within its range. Since $u_n = x_n - \varepsilon_n$, Equation (2.8) can be written as

$$q(u_n) = \underbrace{x_n}_{\textit{signal}} + \underbrace{\varepsilon_n - \varepsilon_{n-1}.}_{\textit{quantization error}} \tag{2.10}$$

In Equation (2.10), the quantity ε_n is the quantization error that would be seen at the modulator output *if there were no feedback loop.* However, as a result of the negative feedback, the first-order difference or discrete-time derivative of the error, $\varepsilon_n - \varepsilon_{n-1}$, appears at the output instead. The hope is that this difference signal is concentrated at high frequencies and can be removed by the digital low pass filter in the postprocessor. If the quantization noise can be shown to be uncorrelated with the input signal and have statistical moments consistent with a uniform white process, we can justifiably refer to this operation as noise shaping, since only the quantization noise will be affected by the filtering operation. Gray [26] has shown that the quantization noise spectrum of a single-loop $\Sigma\Delta$ modulator is in fact correlated with the input and is *not* white but contains discrete spectral components

whose amplitudes can have a significant impact on modulator performance. He has also shown that higher-order modulators, such as multi-loop and multi-stage modulators, generate quantization noise which is asymptotically uncorrelated and has white statistics making the noise shaping characterization appropriate for these modulators. In Chapter 4 we extend Gray's analysis and show that these same results hold for the error diffusion modulator.

To demonstrate the operation of a first-order modulator with a dc input, consider Figure 2.6. Here $x_n = x = 0.1$ and the quantizer takes on values $q_n \in \{-0.5, +0.5\}$. Figure 2.6(a) shows a first-order error diffusion modulator and Figure 2.6(b) shows the numerical evaluation of each of the variables in Figure 2.6(a) for ten consecutive sample intervals. By examining the quantizer output sequence q_n, it is clear that the sample mean of the modulator output equals the dc input x. Therefore, the modulator maintains the output sample average at the value of the input. This is demonstrated in Figure 2.6(b) using analog averaging: $1/10 \sum_{n=1}^{10} q_n = 0.1$. Figure 2.7 shows how the sample average of the quantizer output converges to the dc input as the number of samples in the averaging process increases. Under normal operation, the output of the quantizer is fed to the digital postprocessor which performs this averaging function digitally. A dc input can be considered as an approximation to a slowly varying input and therefore represents the operation expected in the case of a large oversampling ratio where $f_S \gg f_N$.

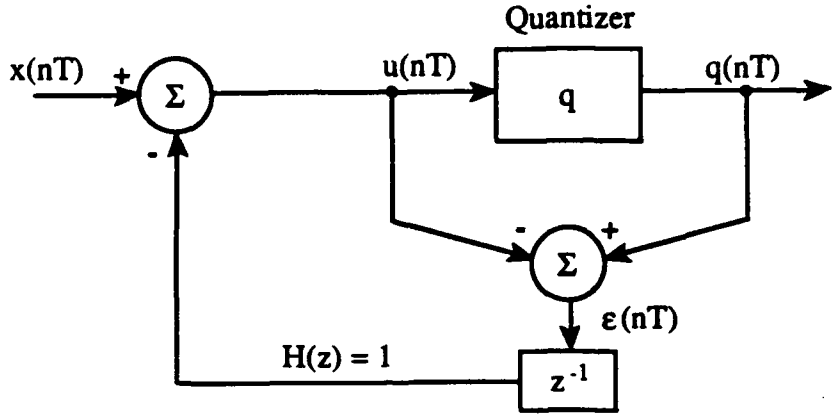

(a)

x_n	ε_n	u_n	q_n
	0.4	0.1	0.5
0.1	-0.2	-0.3	-0.5
0.1	0.2	0.3	0.5
0.1	-0.4	-0.1	-0.5
0.1	0.0	0.5	0.5
0.1	0.4	0.1	0.5
0.1	-0.2	-0.3	-0.5
0.1	0.2	0.3	0.5
0.1	-0.4	-0.1	-0.5
0.1	0.0	0.5	0.5
			1.0 / 10 = 0.1

(b)

Figure 2.6: Example of first-order modulator operation (a) first-order error diffusion modulator (b) numerical evaluation of each variable for ten consecutive sample intervals with a dc input of 0.1 units.

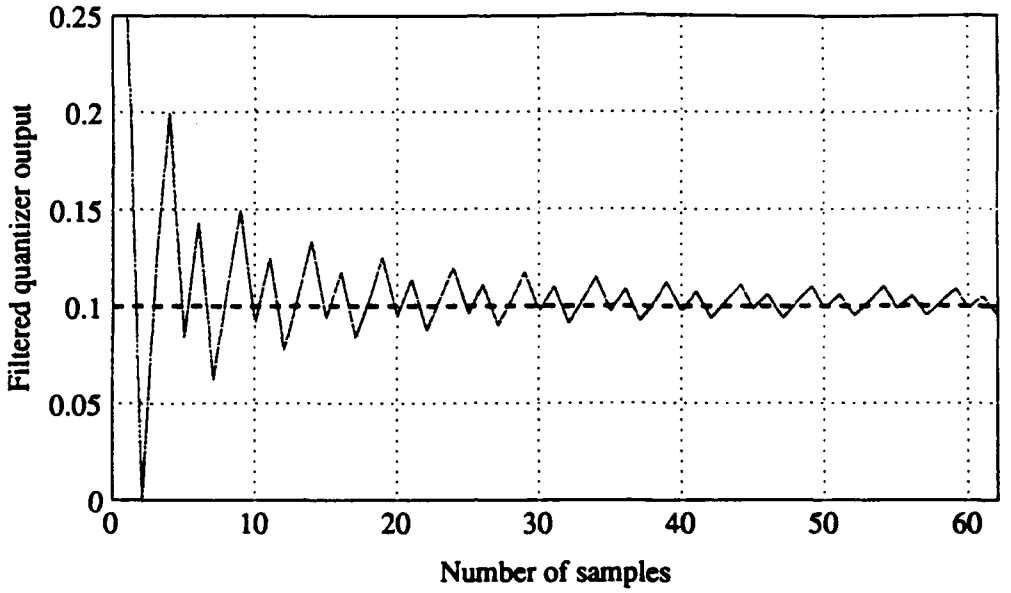

Figure 2.7: Plot of quantizer output sample average for $x_n = 0.1$.

If we assume white quantization noise characteristics and use z-transform techniques, the variables in Figure 2.5 can be recast in terms of spectral noise shaping as follows:

$$E(z) = Q(z) - U(z) = Q(z) - X(z) + z^{-1}E(z)H(z). \tag{2.11}$$

Next, the quantization error of the entire modulator, $\hat{\epsilon}_n \equiv q(u_n) - x_n$, can be related to the quantizer error, $\epsilon_n = q(u_n) - u_n$, by

$$G(z) \equiv \frac{\hat{E}(z)}{E(z)} = 1 - z^{-1}H(z), \tag{2.12}$$

where $\hat{E}(z)$ and $E(z)$ are the z-transforms of $\hat{\epsilon}_n$ and ϵ_n, respectively. From Equation (2.12) it becomes clear that the overall modulator quantization error is a filtered or spectrally shaped version of the quantizer error. The higher the order N of the filter $H(z)$, the more in-band noise suppression can be expected. Figure 2.8 shows the noise shaping characteristics for first- and second-order noise shaping filters. For an N^{th}-order transversal filter that satisfies the unity gain criteria and generates N

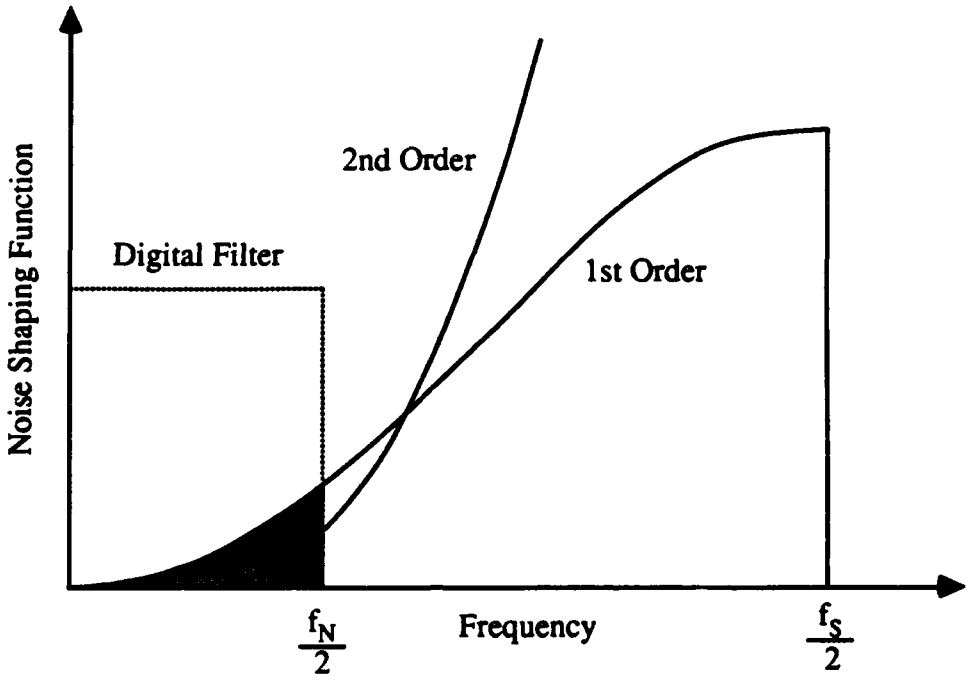

Figure 2.8: Noise shaping characteristics for first- and second-order filters.

zeros in the transfer function at $z = 1$, the filter weights are given by the binomial coefficients

$$w_i = -(-1)^i \begin{pmatrix} N \\ i \end{pmatrix} \qquad \text{for i} = 1, 2, \ldots, \text{N}, \tag{2.13}$$

where the expression

$$\begin{pmatrix} n \\ r \end{pmatrix} \equiv \frac{n!}{(n-r)!r!} \tag{2.14}$$

is the *binomial coefficient*.

An N^{th}-order error diffusion modulator which uses a transversal filter with coefficient weighting described by Equation (2.13) is shown in Figure 2.9. For modulators with $N > 2$ and filter weights described by Equation (2.13), stability of the feedback loop is an issue that must be addressed [27].

An alternate method of achieving higher order noise shaping and avoiding stability problems is to use a cascade of single-loop modulators, called a multi-stage architecture [28, 29, 30], shown in Figure 2.10 for the case $N = 2$. This method of

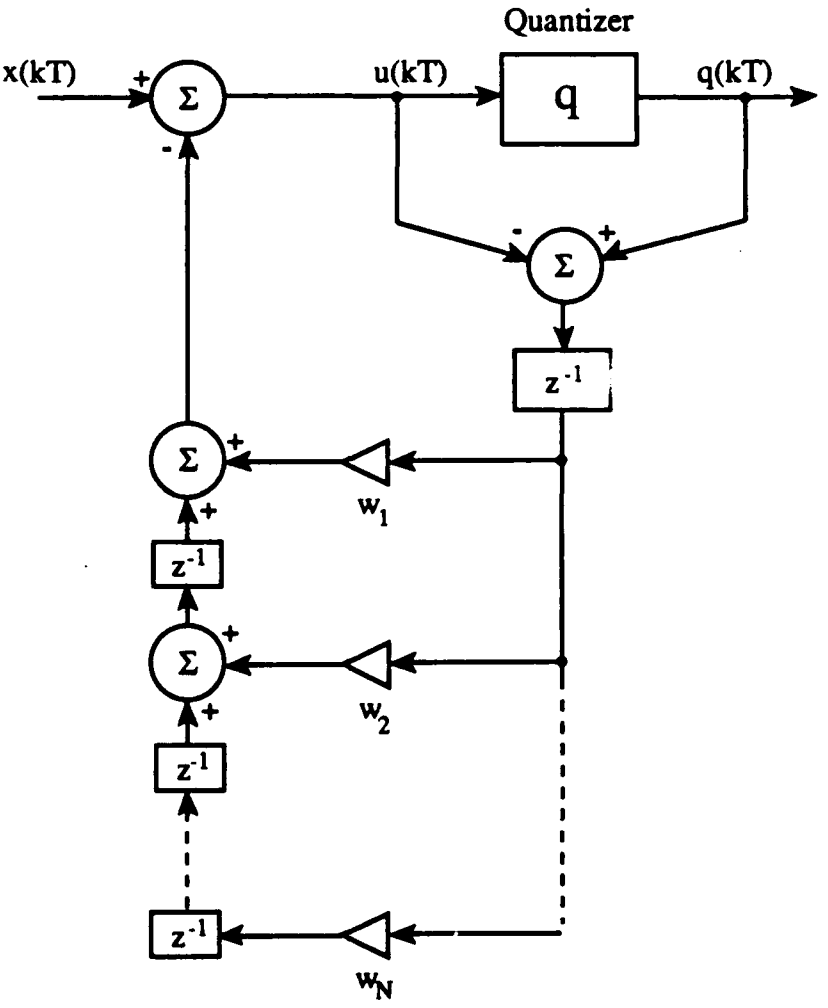

Figure 2.9: Block diagram of an N^{th}-order error diffusion modulator.

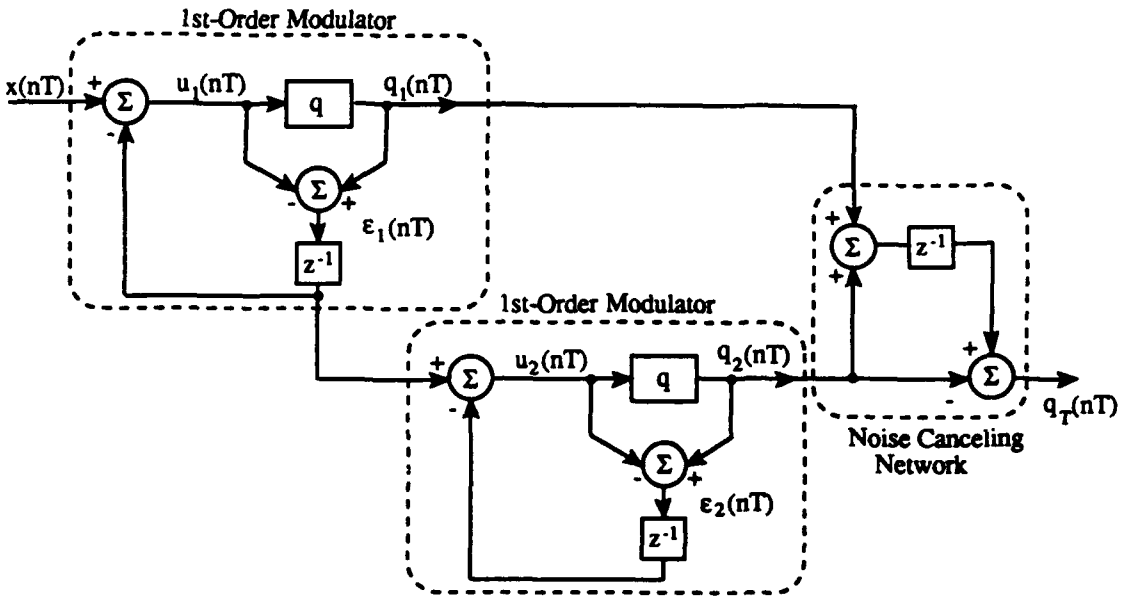

Figure 2.10: Two-stage error diffusion architecture.

implementing higher-order modulators is guaranteed to be no-overload stable, however, care must be taken to ensure proper gain matching between the individual first-order sections. In Chapter 4 we will evaluate these gain matching tolerances for the architecture shown in Figure 2.10.

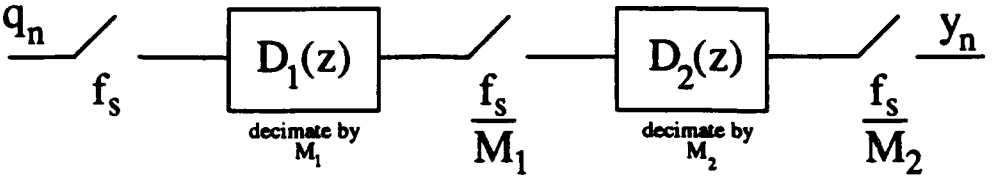

Figure 2.11: Two-stage decimation filter.

2.2 The Postprocessor

As discussed earlier, the function of the postprocessor is to digitally filter and decimate the output of the modulator such that the quantization noise that was spectrally shaped by the modulator is removed through low-pass filtering and the output digital signal is decimated to the Nyquist rate of the original sampled signal. An ideal low-pass filter with cutoff frequency f_B is generally used to quantify limiting case performance. Since the ideal low-pass filter can only be approximated in practice, other practical filters have been investigated for this application [31]. A popular decimation filter, shown in Figure 2.11, consists of a $\text{sinc}^k(f)$ filter which down-samples the signal to four times the Nyquist frequency, followed by a low-pass baseband filter which further down-samples the signal to the Nyquist frequency [32]. This technique of successively reducing the sampling rate by a factor of two can also be extended to include more than two filter stages.

The $\text{sinc}^k(f)$ filter is comprised of a cascade of comb filters and can be described by the z-transform

$$D_1(z) = sinc^k(z) \equiv \left[\frac{1}{M_1} \cdot \frac{1 - z^{-M_1}}{1 - z^{-1}}\right]^k \tag{2.15}$$

which has the frequency response

$$H_1(f) = sinc^k(f) \equiv \underbrace{\left[\frac{sinM_1\pi fT}{M_1 sin\pi fT}\right]^k}_{magnitude} \cdot \underbrace{\frac{e^{-j\pi fTM_1}}{e^{-j\pi fT}}}_{phase}, \tag{2.16}$$

where M_1 is the decimation factor of the filter. Candy has shown that for $k = N+1$, the sinc^k(f) filter is a practical alternative to the ideal low-pass filter in terms of the trade-offs between the quantization noise power and the oversampling ratio [21]. The filter described by Equation (2.15) is also hardware efficient and can be realized in two sections without multipliers or the storage of the filter coefficients. The first section, which implements the denominator of $D_1(z)$, is comprised of a cascade of k discrete-time integrators operating at the original sampling rate, f_S. The second section, which implements the numerator of $D_1(z)$, is a cascade of k discrete-time differentiators operating at the reduced rate f_S/M_1 due to the resampler. Modulo arithmetic is used within the sinc^k(f) filter to suppress register overflow. As an example of the hardware efficiency of this particular filter structure, for $k = 2$, $f_S = 256$ kHz and an intermediate sampling frequency of 8 kHz, the sinc^2(f) filter requires only four adders, four 1-bit storage registers, and a multiply-by-eight circuit that is implemented by a 3-bit shift [33]. The second-stage baseband filter $D_2(z)$ is usually selected based on application specific requirements such as passband linearity, width of the transition band, and rejection of spurious signals in the stop band. In many cases, a simple linear phase transversal filter is used for the second stage.

2.3 System Performance

A convenient measure by which to compare an A/D converter's performance is the maximum signal-to-quantization noise ratio (SQNR$_{max}$). SQNR$_{max}$ is defined as the ratio of the output power at the frequency of a full-scale input sinusoid to the quantization noise power within the signal baseband [34]. In the case of an oversampled A/D converter, analytic evaluation of this expression requires knowledge of the quantizer error spectrum and the postprocessor filter transfer function. If

we assume white quantization noise characteristics and an ideal low pass filter with cutoff frequency f_B, the SQNR_{max} for an N^{th}-order modulator with a full-scale input range of $\pm\Delta/2$ can be shown to be

$$\text{SQNR}_{max}(M,N) = \frac{3}{2} \cdot \left[\frac{2N+1}{\pi^{2N}}\right] \cdot M^{2N+1}, \tag{2.17}$$

where N represents the order of the modulator and M is the oversampling ratio, defined as

$$M \equiv \frac{f_S}{f_N}. \tag{2.18}$$

For comparison, the SQNR_{max} of a conventional Nyquist rate uniform quantizer with b bits resolution can be shown to be [35]

$$\text{SQNR}_{max}(b) = 3 \cdot 2^{2b-1}. \tag{2.19}$$

Equations (2.17) and (2.19) provide a complete description of the relationship between the modulator order, oversampling ratio, SQNR_{max}, and number of equivalent bits resolution. If we know the modulator sampling rate and the input analog signal bandwidth, the upper bound resolution of the converter can be calculated using these two equations. Figure 2.12 shows the theoretical SQNR_{max}(M,N) and equivalent resolution for first- through fourth-order oversampled modulators as a function of oversampling ratio. Results for $N = 1$ are also included because, although the additive noise model does not predict the spectral characteristics of the quantization noise, it does yield accurate results for the SQNR_{max} [26]. The case of no noise shaping represents the SQNR_{max} that can be expected if the same quantizer, embedded in the feedback loop of the oversampled modulator, were simply oversampled and digitally filtered. The slope of this curve is 3 dB per octave and is included only for comparison. The slope of the $N = 1$ curve is 9 dB per octave and that of the $N = 2$ curve is 15 dB per octave, showing the significant advantage achieved by using a noise shaping modulator.

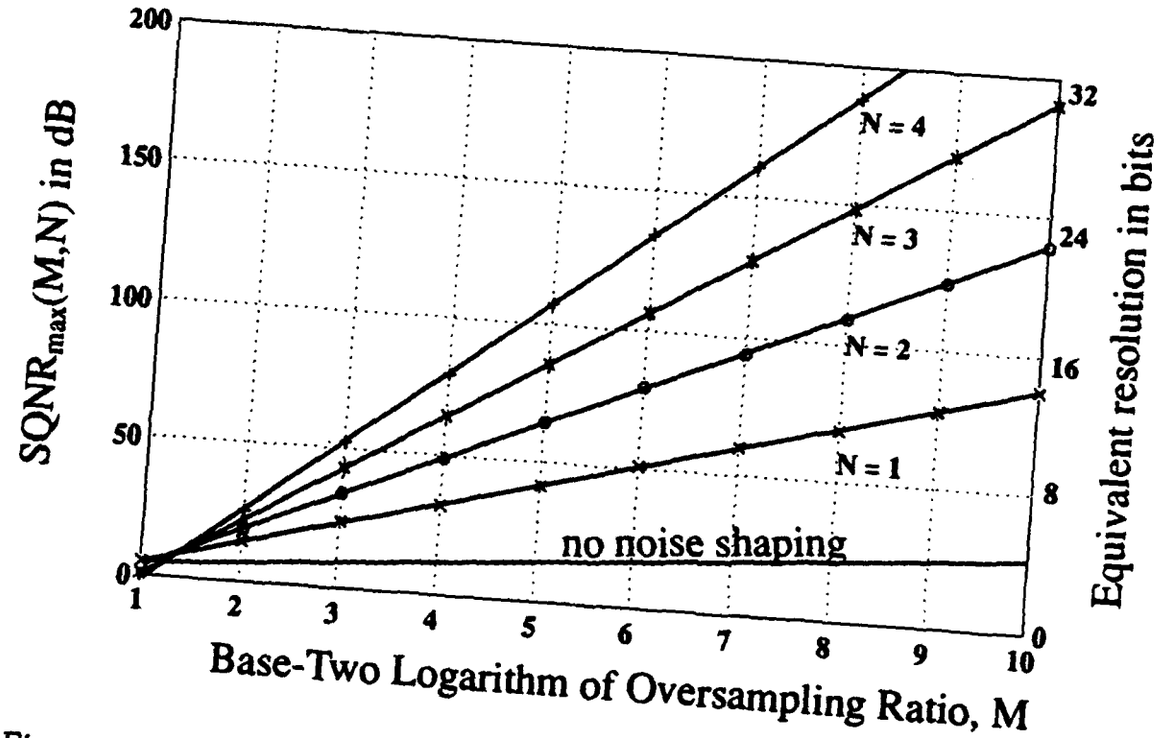

Figure 2.12: Maximum signal-to-quantization noise ratio of N^{th}-order modulators.

2.4 Summary

In this chapter, we have introduced the concepts necessary to the understanding of oversampled A/D conversion. The principal components of an oversampled A/D converter are a modulator and a digital postprocessor. The sampling frequency of such a converter is, by definition, much greater than that required by the Nyquist criterion.

There are two general coding techniques associated with the oversampled modulator, predictive and interpolative coding. Predictive coders spectrally shape both the analog input signal *and* the quantizer noise, but they suffer from channel error accumulation and slope overload. Interpolative or noise shaping coders spectrally shape *only* the quantization noise and are much more robust against noise and signal dynamics.

The function of the modulator is twofold: to quantize the input analog signal using a low resolution quantizer and to spectrally shape the quantization noise such that the noise power falling within the baseband is reduced and reshaped to frequencies above the signal cutoff. This is accomplished using oversampling, negative feedback, and linear filtering techniques.

The function of the digital postprocessor is to remove the quantization noise above the signal baseband using a low pass filter, provide anti-aliasing protection, and reduce the rate to the Nyquist rate of the sampled signal by trading word rate for word length. Many different filter architectures are currently available which perform this function, with the most popular being the $\mathrm{sinc}^k(f)$ filter. This filter is a practical alternative to the ideal low-pass filter in terms of the trade-offs between the quantization noise power and the oversampling ratio and is also hardware efficient and can be realized without multipliers or the storage of the filter coefficients.

The combined operation of modulation and decimation filtering makes 16 bit resolution possible using only a two-level quantizer. This is a fundamentally different approach from classic Nyquist rate quantizers, in which the resolution is determined by the number and spacing of reference levels in the quantizer.

Chapter 3

Optical Oversampled A/D Conversion

AN OPTICAL IMPLEMENTATION OF AN OVERSAMPLED A/D CONVERTER can provide several advantages specifically associated with optical technology. First, optical sampling rates exceed electronic sampling rates, making larger oversampling ratios and therefore higher resolution possible. Similarly, for a given oversampling ratio, the higher optical sampling rate allows conversion of larger bandwidth input signals. Another advantage associated with optical sampling is the decoupling of the sampled and sampling signals, achieved when the sampling signal is optical and the sampled signal is electronic. Alternatively, an all-optical A/D converter would provide compatibility between an input analog optical signal and an output digital optical signal and is therefore desirable for future all-optical computing applications. The inherent parallelism that optics provides can also be used to extend this A/D conversion technique to multidimensional applications.

3.1 Multiple Quantum Well Devices

In this section, we focus on the optical devices necessary to implement an optical oversampled A/D converter. From the theoretical development in Chapter 2, there are two principal functions which require optical implementation: the modulator and the digital postprocessor. The requisite functionality of the optical devices used in the modulator will depend on the specific modulator architecture. If the N^{th}-order error diffusion modulator of Figure 2.9 is chosen, then the functions necessary are optical quantization, subtraction, and transversal filtering. If the multi-stage modulator of Figure 2.10 is chosen instead, then only optical quantization and subtraction are required. An optical realization of the digital postprocessor will require digital optical logic to implement the multi-bit full adders and storage registers.

The optical oversampled modulators considered in this research use low resolution, one-bit quantizers, which are elementary threshold devices. Any optically bistable device can serve in this capacity. A wide range of optical devices and techniques which can provide the desired functionality are currently available. A good review of optical bistability and existing devices can be found in [36, 37, 38]. Our goal in developing an optical oversampled A/D converter is to extend the resolution and conversion rates beyond those currently possible with other electronic or optical converters. In order to accomplish this goal, high speed optical devices are required. We will focus on a new optical device which has become popular in optical signal processing applications because of its high-speed and low power consumption operation: the multiple quantum well modulator.

Multiple quantum well (MQW) devices consist of alternating thin layers of two semiconductor materials, the most studied to date being GaAs and AlGaAs. The thin crystal layers are typically grown using advanced growth techniques such as molecular beam epitaxy (MBE) or metal-organic chemical vapor deposition (MOCVD), which have the ability to grow these layers with atomic precision. The operation of these devices can be understood by considering the effect of the layered structure on the electrons and holes within the material. The electrons and holes in the semiconductor material see a minimum energy in the GaAs 'well' material

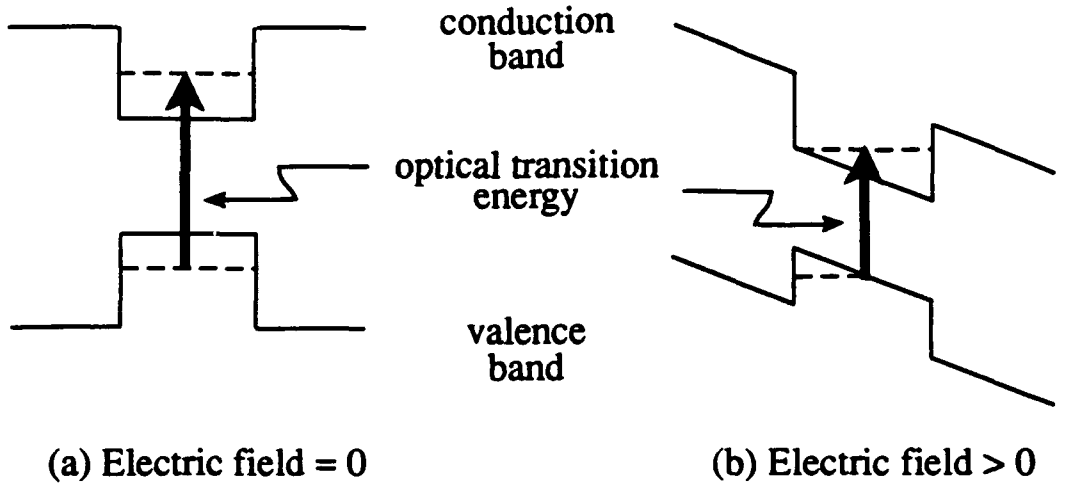

Figure 3.1: Energy band diagrams of quantum well devices (a) with no applied field (b) with electric field applied perpendicular to the layers.

and therefore the AlGaAs material on either side appears as a 'barrier'. Because the semiconductor layers are so thin, the electrons and holes behave as 'particles in a box', just as in elementary quantum mechanics problems. The resulting quantum confinement causes discrete energy levels of the electrons and holes. One important consequence of this energy discretization is that very strong absorption peaks called *exciton absorption peaks* appear at the edges of these steps, even at room temperature. When an electric field is applied perpendicular to the layers, the electrons and holes move to lower energies, and the optical transition energy decreases, resulting in a shift in the wavelength of the absorption peak. This can be understood with the aid of the energy band diagrams shown in Figure 3.1. Figure 3.1(a) shows the energy band diagram under conditions of no applied electric field. The optical transition energy is represented here by the length of the arrow. When an electric field is applied, the bands tilt as shown in Figure 3.1(b), both the electron and hole move to lower energies, and the optical transition energy is decreased. Since photon energy is inversely proportional to wavelength, this decrease in optical energy corresponds to an increase or red-shift in the wavelength of the absorption peaks.

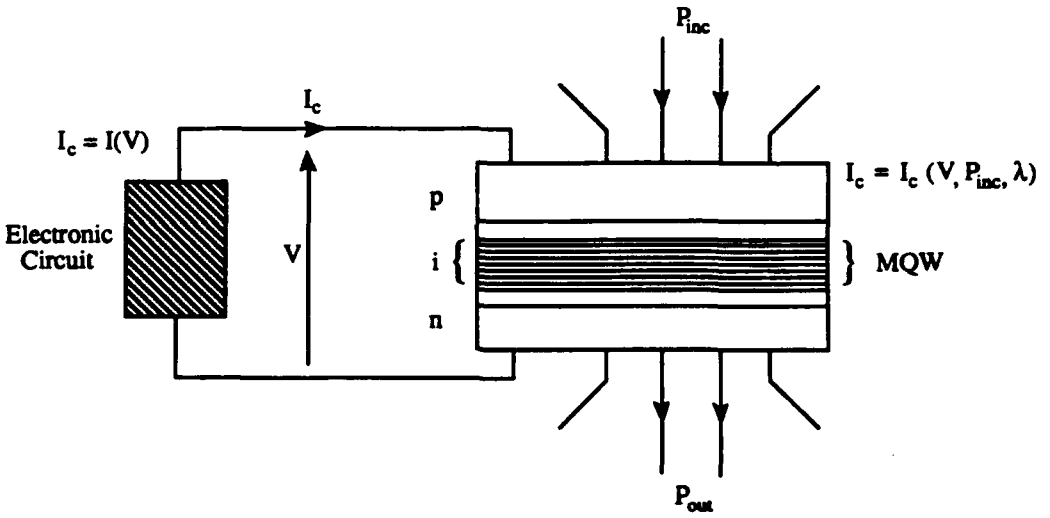

Figure 3.2: General schematic for a transmissive-type QCSE modulator.

This shifting of the absorption peaks is the underlying principle of the quantum confined Stark effect (QCSE) [39, 40]. The basics of QCSE modulators have been extensively reviewed elsewhere [41, 42, 43], and therefore we only present a brief summary of the theory and operating characteristics necessary to understand the application of these devices to the optical oversampled A/D converter.

Since a change in optical absorption at a specific wavelength can be affected by a change in the applied electric field, QCSE or electroabsorptive modulators can be produced. In most instances, the structure used in these modulators is a *p-i-n* diode. Figure 3.2 shows the circuit schematic for a general transmissive-type QCSE modulator. The quantum well layers are placed within the intrinsic region of the *p-i-n* diode. The modulator (diode) is externally connected to an electronic biasing circuit that controls the electric field across the device. An important advantage associated with this type of structure is that the *p-i-n* diode is operated in a reverse bias configuration and therefore, very low operating energies can be achieved while maintaining large electric fields across the quantum wells. With the configuration shown in Figure 3.2, true optoelectronic feedback is produced. Since the modulator structure is basically a photodiode, optical energy incident on the diode produces

a photocurrent. The photocurrent flows through the electronic biasing circuit producing a change in the voltage across the diode which, in turn, changes the optical absorption of the modulator, thereby completing the feedback loop.

Another important class of QCSE modulators is the reflective-type modulator. In this type of modulator, a highly reflective mirror is grown on the back of the device and therefore, the incident light passes through the MQW material twice before exiting the modulator. Larger optical absorption can be achieved with the same applied field as in the transmissive-type modulators using this technique. If a partially-reflecting mirror is grown on the front of the reflection-type modulator, then a Fabry-Perot étalon is created around the MQWs. The cavity causes an increase in the field strength at the Fabry-Perot wavelength which produces larger shifts of the exciton absorption peaks than in a modulator without an étalon. This particular modulator structure, sometimes called a reflection electroabsorption modulator (REAM) or an asymmetric Fabry-Perot modulator, has gained considerable attention recently because of its lower insertion loss, higher contrast ratios, and lower operating voltages [44, 45, 46, 47, 48].

The operating characteristics of the modulator greatly depend on the electronic biasing circuit and the sign of the feedback. In general, the feedback can be described by two simultaneous relations. The first describes the operation of the quantum well device as a photodetector and can be written as

$$I_c = I_c(V, P_{inc}, \lambda) = S(V, \lambda) \cdot P_{inc}, \tag{3.1}$$

where I_c is the current through the modulator, V is the voltage across the modulator, P_{inc} is the incident optical power, λ is the wavelength of the incident light, and S is the responsivity of the detector measured in amperes per watt. The second relation necessary to describe the feedback comes from the operation of the electronic biasing circuit

$$I_c = I_c(V), \tag{3.2}$$

where the current I_c is a function of the biasing circuit parameters such as supply voltage and circuit component values.

From a linearized stability analysis of Equations (3.1) and (3.2), we can deduce

the sign of the feedback and therefore describe the operation of the MQW modulator. If we assume that the MQW device is modeled as a capacitor with capacitance C, and consider the change in voltage v about the equilibrium point, we obtain to first-order the equilibrium solutions [43]

$$C\frac{\mathrm{d}v}{\mathrm{d}t} = \left[\frac{\mathrm{d}I_c}{\mathrm{d}V} - P_{inc}\frac{\mathrm{d}S}{\mathrm{d}V}\right] v, \tag{3.3}$$

assuming current flow in the direction shown in Figure 3.2. Equation (3.3) has the form of a classic first-order differential equation which has as its solutions exponential terms, with characteristics defined by the term in the square brackets. If this term is positive, the feedback will be positive creating unstable operating conditions and causing the solution to grow without bound. If the term is negative, the feedback will also be negative and the solution is stable. Under most operating conditions, the electronic biasing circuit has positive slope resistance and therefore $\mathrm{d}I_c/\mathrm{d}V < 0$. From this analysis we can now identify the sign of the feedback based on these parameters

$$\begin{aligned} P_{inc}\tfrac{\mathrm{d}S}{\mathrm{d}V} < \tfrac{\mathrm{d}I_c}{\mathrm{d}V}; &\quad \text{positive feedback} \\ \tfrac{\mathrm{d}S}{\mathrm{d}V} > 0; &\quad \text{negative feedback.} \end{aligned} \tag{3.4}$$

Figure 3.3 shows the responsivity of a specific QCSE modulator, the self electro-optic effect device (SEED) [43], as a function of wavelength. Two operating wavelengths which satisfy the two feedback conditions described in Equation (3.4) are identified in Figure 3.3. Point A corresponds to conditions under which increasing voltage produces decreasing responsivity, and therefore, this operating point is unstable. At point B, the responsivity increases with increasing voltage and therefore this operating point is stable.

We now describe the operation of the MQW modulators required to implement the optical oversampled A/D converter.

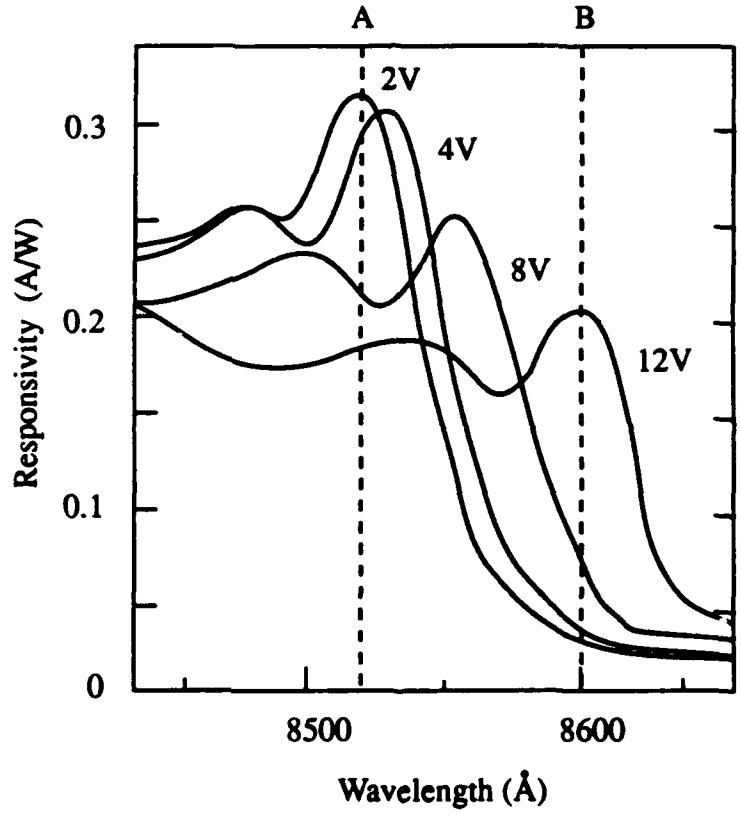

Figure 3.3: Responsivity curves for self electrooptic effect device. Point A represents an unstable operating point since $\mathrm{d}S/\mathrm{d}V < 0$. Point B represents a stable operating point because $\mathrm{d}S/\mathrm{d}V > 0$.

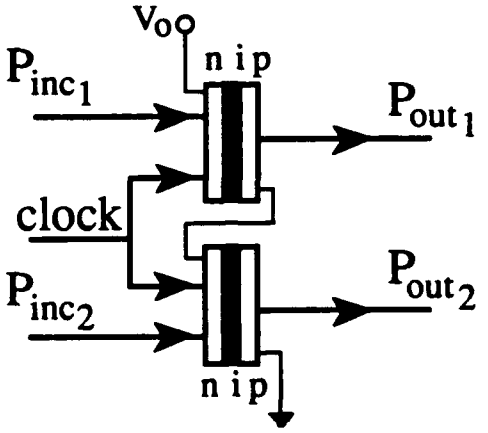

Figure 3.4: Schematic diagram of a transmissive-type symmetric self electrooptic effect device (S-SEED).

3.1.1 Optical Bistability

The principle function required in any A/D converter is quantization. In the oversampled A/D converter, a one-bit quantizer or simple threshold device is frequently used. One method of achieving optical thresholding is to use a device with optically bistable characteristics. If the MQW modulator feedback is positive, corresponding to operation at an unstable operating point, optical bistability can be achieved. A series of two MQW modulators, called a symmetric modulator, produces improved bistable characteristics over those of a single device and also provides some additional benefits which include optical gain, tolerance to optical power variations, and non-critical biasing [49].

Figure 3.4 shows a schematic diagram of a transmissive-type symmetric SEED (S-SEED). This configuration is bistable in the ratio of the incident optical powers P_{inc_1} and P_{inc_2}. Figure 3.5 shows the transfer characteristics for both P_{out_1} and P_{out_2} versus P_{inc_1}, with the input P_{inc_2} held constant. These curves were generated using the reflectivity data from [50] and the techniques described in [43]. In order to achieve one bit quantization with these characteristics, we use one-half of the P_{out_2}

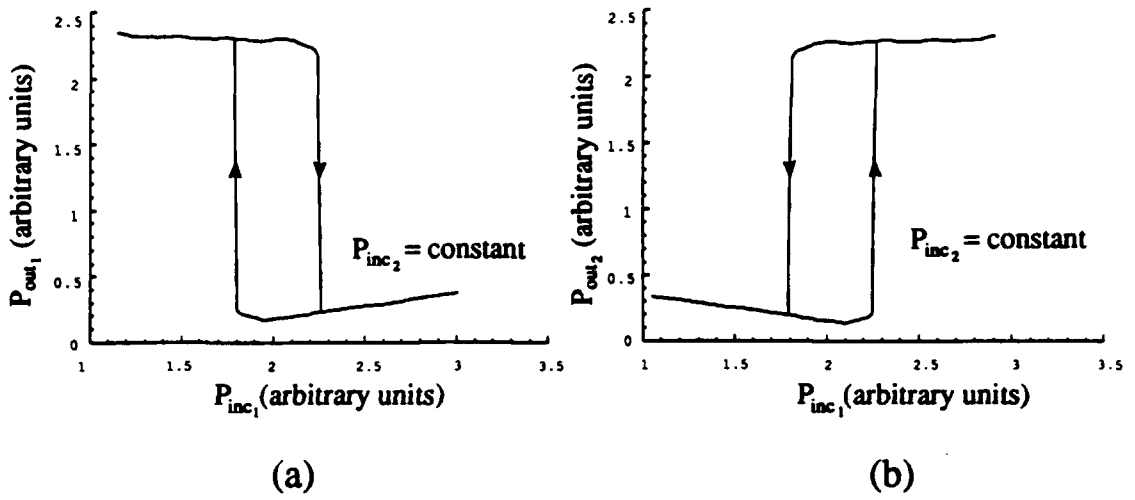

Figure 3.5: Transfer characteristics for a symmetric MQW modulator with constant P_{inc_2} (a) P_{out_1} versus P_{inc_1} (b) P_{out_2} versus P_{inc_1}.

versus P_{inc_1} curve in Figure 3.5(b). By always using the transition from the low-P_{out_2} state to the high-P_{out_2} state, we can achieve the necessary optical thresholding function. The transition back to the low-P_{out_2} state at the end of each clock cycle is achieved using either natural RC decay or by dynamic electrical techniques.

Another advantage of using the configuration in Figure 3.4 is that optical gain can be achieved. This can be understood with the aid of Figure 3.6. By setting the state of the symmetric device with low-power optical signals P_{inc_1} and P_{inc_2}, and subsequently, one clock cycle later, reading the information out with a higher power optical clock, *time sequential gain* [49] can be achieved. This gain mechanism can be used to overcome optical losses in the system as well as to implement an offset bias for the quantizer in the noninterferometric modulator realization to be described later.

3.1.2 Optical Subtraction

Figure 3.7 shows the structure and configuration of a reflection-type MQW modulator, as it is used for noninterferometric optical subtraction.

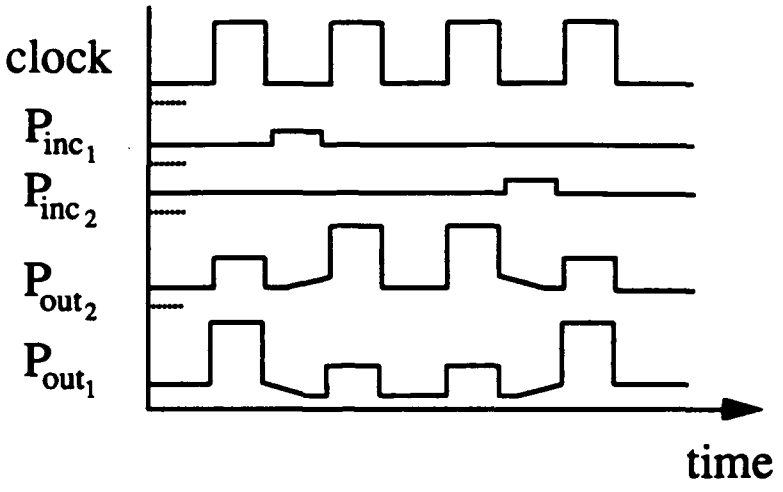

Figure 3.6: Demonstration of time sequential gain using a symmetric MQW modulator.

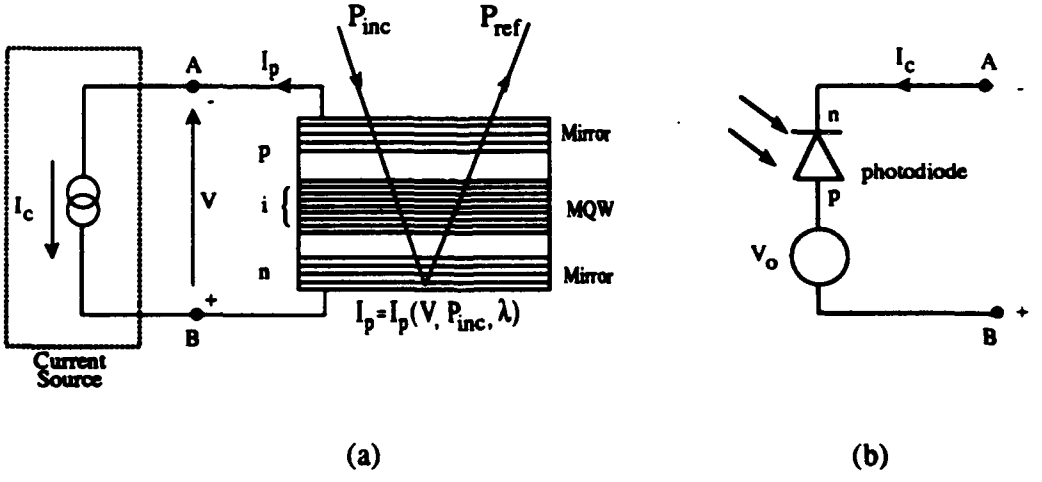

Figure 3.7: Structure and configuration of the reflection electroabsorption modulator for noninterferometric subtraction. (a) idealized circuit with a constant current source, (b) an optical realization of the constant current source.

Noninterferometric optical subtraction using a MQW modulator can be best understood by first considering the optical absorption of the device, which can be described by

$$A = \frac{h\nu}{\eta e} \cdot S, \tag{3.5}$$

where η is the internal quantum efficiency, h is Planck's constant, ν is the optical frequency, e is the electron charge, and S is the responsivity. The absorbed power is $P_a = P_{inc} \cdot A$, where P_{inc} is the incident optical power. The photocurrent is then $I_p = S \cdot P_{inc}$. At any equilibrium state, $I_c = I_p$ and therefore

$$P_a = \frac{h\nu}{\eta e} \cdot I_c. \tag{3.6}$$

By controlling the bias current I_c, the optical power absorbed by the modulator can be linearly controlled and the resulting reflected power P_{ref} can be described by the subtraction relation

$$P_{ref} = P_{inc} - P_a. \tag{3.7}$$

It should be noted that since Equation (3.7) is the result of optical absorption, P_{ref} is necessarily non-negative. Equations (3.6) and (3.7) are the fundamental equations describing the operation of noninterferometric optical subtraction. In order to linearly control the bias current, a constant current source is required. One method of implementing a constant current source which fits the framework of optical processing is shown in Figure 3.7(b). Light falling on the photodiode generates a constant current which is directly proportional to the control light power. An advantage of this constant current structure is that both the modulator and photodiode can be constructed from the same GaAs material and can therefore be monolithically integrated into the same structure providing both high efficiency and speed. The specific application of noninterferometric optical subtraction differs from that of *self-linearized modulation* and *optical level shifting* [43] in that both the electronic current $I_c(t)$ *and* the incident optical signal $P_{inc}(t)$ are explicitly time-varying signals.

3.1.3 Switching Speed and Energy Requirements

In order to make quantitative comparisons between our optical oversampled A/D converter and other converters, the speed and power requirements of the constituent devices must be known. In one realization of the optical oversampled A/D converter, the fundamental building block is the multiple quantum well modulator. Here we analytically present the fundamental relationships between energy and speed for the symmetric MQW modulator as used for *one-bit optical quantization* and the single MQW modulator as used for *noninterferometric optical subtraction.*

One-bit Optical Quantization

Considering Figure 3.4, we can begin with a first-order approximation to the speed by modeling the individual MQW modulators as parallel plate capacitors and computing the time-constant of the circuit. Writing an equation for the circuit current at a point between the two modulators

$$P_{inc_1} S_{MQW_1}(V) - P_{inc_2} S_{MQW_2}(V_o - V) + C_{MQW_1} \frac{\mathrm{d}V}{\mathrm{d}t} - C_{MQW_2} \frac{\mathrm{d}(V_o - V)}{\mathrm{d}t} = 0, \quad (3.8)$$

where $S_{MQW_i}, i = 1, 2$ are the responsivities, and $C_{MQW_i}, i = 1, 2$ are the capacitances of the individual MQW modulators, respectively. Next, assume that the two modulators are identical in construction and therefore $C_{MQW_1} = C_{MQW_2} \equiv C$ and $S_{MQW_1}(V) = S_{MQW_2}(V_o - V) \equiv \overline{S}$, where $\overline{S}$ is the average responsivity assumed to be a constant. If we next assume that the time-rate of change of V is equal to V_o divided by the differential time element Δt, then

$$\frac{\mathrm{d}V}{\mathrm{d}t} = \frac{V_o}{\Delta t}, \quad (3.9)$$

and Equation (3.8) becomes

$$P_{inc_1} \overline{S} - P_{inc_2} \overline{S} + C_T \frac{V_o}{\Delta t} = 0 \quad (3.10)$$

where $C_T = C/2$ represents the total series capacitance of the circuit. From these approximations, the total switching time of this symmetric modulator can be expressed as

$$\Delta t = \frac{C_T V_o}{\overline{S}(P_{inc_2} - P_{inc_1})}. \quad (3.11)$$

Equation (3.11) identifies the device characteristics which fundamentally limit the speed of a symmetric MQW modulator. Both the average responsivity $\overline{S}$ and the capacitance C_T are fixed values, determined by device construction, and therefore can only be changed through scaling and improved manufacturing techniques. In order to reduce the switching time Δt, the difference between the two input optical power levels P_{inc_1} and P_{inc_2} must be increased. However, in order to substantially reduce the switching time, a large power difference is required which changes the fundamental operation of the device from optical bistability to optical switching. The only alternative is to increase the power level of both P_{inc_1} and P_{inc_2} such that the difference is in units of milliwatts or watts instead of microwatts. Therefore, there is a fundamental trade-off between incident optical power and switching speed of these multiple quantum well devices.

It should be noted that this method of first-order approximation of the switching speed has demonstrated good agreement with experimental results. In [51], 33 psec switching time of an S-SEED was demonstrated with an optical switching energy of approximately 6 pJ. This switching energy is currently a factor of 10 higher than that of an electronic device with similar functionality. As manufacturing and scaling techniques improve, we expect MQW switching energies to also improve and become competitive with those of electronic bistable devices.

Noninterferometric Optical Subtraction

Figure 3.7(a) shows the configuration of a reflection-type MQW modulator with a Fabry-Perot cavity used to implement noninterferometric optical subtraction. Figure 3.7(b) shows an optical implementation of the constant current source using a photodetector and voltage source.

If we again begin by modeling both the MQW modulator and the photodetector as parallel plate capacitors, we can write an equation for the circuit current at a point between the modulator and the diode which is identical to Equation (3.8). If we assume that the two devices are identical in construction, $C_D = C_{MQW} \equiv C$ and $S_D(V) = S_{MQW}(V_o - V) \equiv \overline{S}$, then the response time for noninterferometric optical subtraction is also given by Equation (3.11).

The energy requirements and operating speed of optical quantization and noninterferometric subtraction using MQW modulators, therefore, are effectively the same. As a result, no delay devices are required in order to satisfy timing requirements in the implementation of the optical modulator.

3.1.4 Bistability and Noninterferometric Subtraction in a Common Oversampled Modulator

As mentioned earlier, the implementation of the optical oversampled modulator requires the operation of optical thresholding and subtraction. In the next section, we will present one realization of the interferometric modulator using MQW modulators which requires only the operation of bistability for the one-bit quantization process. Optical subtraction is accomplished using beamsplitters (combiners) and interferometric techniques. The noninterferometric realization of the optical modulator, however, requires both bistable and noninterferometric subtraction operations in the same modulator architecture.

From previous discussions on the theory of MQW modulators and Figure 3.3, it is clear that the functions of bistability and noninterferometric subtraction each require a different operating wavelength. In order to satisfy this dual wavelength requirement in a common modulator, we can use one of the following techniques. The entire optical oversampled modulator can be operated at a single wavelength and use a higher applied voltage on the bistable MQW modulator. This technique extends the range of wavelengths over which the MQW device is bistable [43]. Since the operating wavelength of a MQW modulator is determined by its material characteristics, another solution is to fabricate the stable MQW modulators used for subtraction with slightly different width quantum wells compared to the bistable MQW modulators used for thresholding, and again operate the modulator at a single wavelength. The amount of the two different semiconductor materials used in the construction of the MQW device is also a factor which determines the operating wavelength. For example, in a MQW modulator fabricated using GaAs and AlGaAs, the amount of Al compared to GaAs is a parameter that effects the

wavelength of operation and therefore can be used for system level considerations. These techniques can change the MQW operating wavelength over the range of wavelengths that the particular material supports. Different semiconductor materials provide operation over a wide range of wavelengths. For example, GaAs/AlGaAs modulators operate over 0.75 – 0.9 μm, strained or *psuedomorphic* InGaAs on GaAs modulators operate over 0.9 – 1.06 μm, and InGaAs/InAlAs on InP devices operate over the range 1.3 – 1.55 μm.

3.2 Optical Oversampled Modulators

In this section, we describe two different approaches to the implementation of the optical oversampled modulator which are based on MQW devices. We characterize the two architectures as interferometric and noninterferometric. Since both realizations rely on the shift of the exciton peaks in a MQW modulator to cause a change in the optical absorption, they both use highly monochromatic sources. They differ in the way optical subtraction is accomplished. The interferometric modulator processes complex amplitude optical signals and uses classical interferometric techniques to accomplish subtraction. The noninterferometric modulator processes non-negative optical signals and uses the noninterferometric optical subtraction technique described in Section 3.1.2.

3.2.1 The Interferometric Modulator

The interferometric optical error diffusion modulator is the simplest of the optical modulator architectures. Figure 3.8 shows the first-order modulator which is based on the architecture of Figure 2.5 with $H(z) = 1$. The modulator structure shown in Figure 3.8 uses transmissive MQW modulators for the optical quantization function. The nonlinear difference equation which describes the operation of this modulator was given previously as Equation (2.8). Here the quantities within the modulator are optical signals represented as complex field amplitudes. In operation, beamsplitters (combiners) BS_1, BS_3, and BS_5 act as subtraction nodes provided that

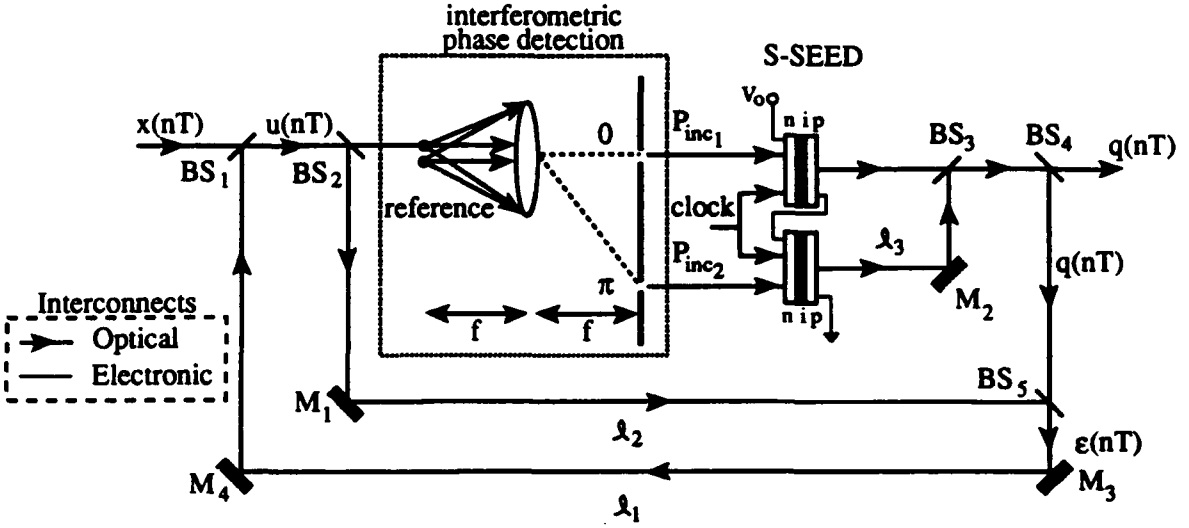

Figure 3.8: First-order interferometric error diffusion modulator.

the pathlengths ℓ_1, ℓ_3, and ℓ_2 are all odd multiples of half-wavelengths, respectively. The coherent reference, lens, and slit arrangement provide for interferometric phase detection (see Appendix B for details), which is necessary for zero-threshold detection in the binary quantizer, implemented here by a symmetric self electrooptic effect device (S-SEED) [49]. The two slits in the phase detector are positioned to select the 0 and π maxima of the interference pattern. The S-SEED provides the binary quantization function as well as the optical gain necessary to overcome system losses. The wavelength (photon energy) is selected such that $dS/dV < 0$ and the operating point is unstable, thereby providing bistability. The threshold is set by the external voltage V_o and the ratio of the two input power levels, P_{inc_1} and P_{inc_2}, where $P_{inc_i} = \int_t^{t+T} A_i f_i(t)dt$, $i = 1, 2$; A_i is the optical pulse amplitude and $f_i(t)$ defines the pulse shape. The binary quantizer levels are $q(u_n) \in \{-\Delta/2, +\Delta/2\}$, the optical threshold is $u_{th} = 0$, and $\Delta = 2b$. If pathlength ℓ_3 is an odd multiple of half-wavelengths, then the output from beamsplitter BS_4 is $+\Delta/2$ if $P_{inc_1} > P_{inc_2}$ and $-\Delta/2$ if $P_{inc_1} < P_{inc_2}$. The rest of the modulator operation follows directly as

described in Chapter 2.

This first-order interferometric modulator can be extended to higher-order using either the cascade approach of Figure 2.10 or the multi-loop architecture of Figure 2.9. By simply replacing mirror M_3 with a beamsplitter and adjusting the S-SEED gain to overcome the additional loss, this first-order architecture can be extended to a second-order cascade modulator. In order to implement a higher-order multi-loop modulator, an interferometric transversal filter like that described in [52] with weights described by Equation (2.13) is placed in the feedback path ℓ_1.

Interferometric optical processing architectures inherently suffer from an intolerance to optical pathlength changes and consequently phase variations. As mentioned earlier, one of the advantages of oversampled modulators is their tolerance to circuit imperfections. The coarse one-bit quantizer absorbs many small circuit imperfections including amplitude errors resulting from phase variations. For example, assume that the S-SEED switching time is 33 psec [49]. At this speed, the optical pathlengths required to satisfy modulator timing requirements in a material such as GaAs can be shown to be on the order of 5 mm. Since these pathlengths are the dominant physical dimension in the modulator, this modulator lends itself to monolithic integration. If the entire modulator is monolithically integrated in GaAs (same as S-SEED material), the thermal tolerance can be shown to be approximately $\pm 1^{o}C$, which is well within current temperature stabilization capabilities. This, of course, assumes an initial temperature and phase calibration of the modulator. As device technology improves, switching speeds will increase making the optical pathlengths in this modulator decrease, thereby increasing the thermal tolerance of the interferometric modulator.

3.2.2 The Noninterferometric Modulator

The block diagram for the first-order noninterferometric optical error diffusion modulator is shown in Figure 3.9. Offset biases $3\Delta/2$ and $\Delta/2$ accommodate the fact that all optical signals within the modulator are non-negative. Figure 3.10 shows the optical implementation of Figure 3.9 using reflection-type MQW modulators. Here, x'_n is the unipolar modulator input generated by sampling $x(t)$ and then biasing

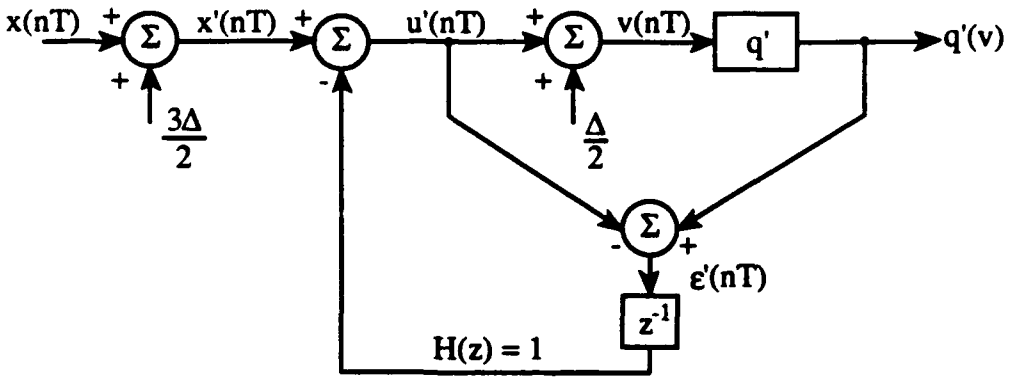

Figure 3.9: Block diagram of a first-order noninterferometric error diffusion modulator.

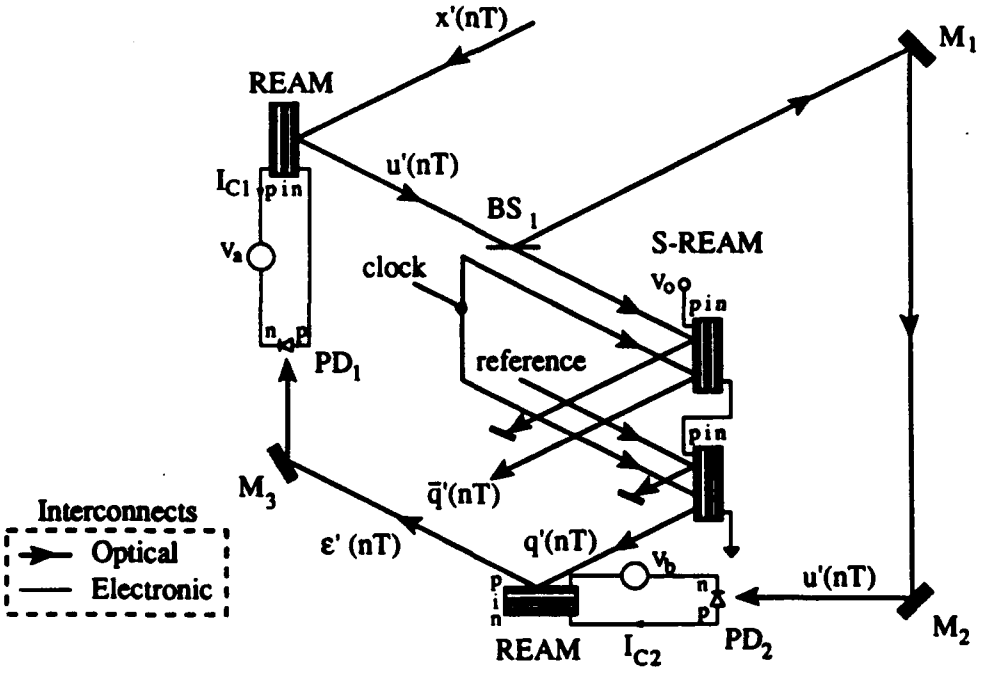

Figure 3.10: First-order noninterferometric error diffusion modulator.

x_n by $3\Delta/2$ to ensure $x'_n \geq 0$. In this configuration, two individual reflection electroabsorption modulators (REAM) are used to implement noninterferometric optical subtraction. These two REAMs are operated at a photon energy such that $dS/dV > 0$, and the operating point is stable. In this mode, the optical absorption of the REAM was previously shown to be directly proportional to the current in the electronic bias circuit, described by Equation (3.6). In this case, the external currents I_{ei}, $i = 1, 2$ are generated by optical signals ε'_{n-1} and u'_n through photodiodes PD_1 and PD_2 respectively, where PD_1 and PD_2 are assumed to be integrated with their respective MQW modulators to ensure maximum efficiency and speed. The S-REAM provides binary quantization and optical gain, but now the threshold is set by the external voltage and the ratio between u'_n and the optical reference. Here the quantizer output levels are $q'(u_n) \in \{\Delta, 2\Delta\}$, the quantizer threshold is $u_{th} = \Delta$, and again $\Delta = 2b$. Time sequential gain is used to shift the bias of $q(u_n)$ by $\Delta/2$, which ensures non-negative signal operation within the modulator. Mathematically, the quantizer error sequences are related by $\varepsilon'_n = \varepsilon_n + \Delta/2$. The dual wavelength requirement between the stable operation of the REAM and the bistable operation of the S-REAM can be satisfied by operating at a single wavelength and using one of the methods discussed in Section 3.1.4. The use of highly monochromatic signals throughout the modulator ensures optimum REAM and S-REAM operation. The rest of the modulator operation follows directly as described in Chapter 2. As in the case of the interferometric modulator, this first-order architecture can also be cascaded to a second-order modulator like that shown in Figure 2.10.

3.3 The Postprocessor

The function of the digital postprocessor is to remove the quantization noise which was spectrally shaped by the modulator and to reduce the rate to the Nyquist rate of the original sampled analog signal. This can be accomplished using either electronic or optical techniques.

3.3.1 Electronic Postprocessing

One method of accomplishing the postprocessing functions is to convert the optical signal to an electronic signal by means of a photodetector and then perform the decimation filtering electronically. In this way, we could make use of existing oversampled A/D converter decimation filters. Many of these decimation filters are currently available in VLSI CMOS (silicon) technology, making integration with the GaAs optical modulators possible. In this case, the converter sampling rate would be determined by the maximum speed of the decimation filter and would therefore probably not utilize the maximum potential of the optical modulator. Faster decimation filters are possible using high-speed bipolar silicon technology or faster materials such as GaAs, and would permit the full potential of the optical modulator to be realized.

An electronic implementation of the postprocessor by no means lessens the advantages gained by the optical modulator. The optical implementation of the modulator provides high-speed operation for the *analog* modulator, while high-speed electronics can easily implement the *digital* functions of the postprocessor. Also, most current applications of A/D conversion require an electronic digital medium as the output format for subsequent electronic digital signal processing.

3.3.2 Optical Postprocessing

Although the simplicity of the decimation filter makes it possible to implement optically, the absence of all-optical digital circuitry which make use of b-bit optical digital words makes it impractical at present. Optics could however be used in the front-end of the postprocessor providing the transition from the high-sampling rate to an intermediate rate, thereby allowing the use of more common electronics in the balance of the postprocessor. Here we suggest one possible approach to the implementation of all or part of the optical digital postprocessor.

Many of the current applications of MQW modulators are in the area of optical digital logic. The basic building block of any digital logic application is the flip-flop. In [49], an optically clocked reset-set (R-S) flip-flop was demonstrated using

an S-SEED and was extended to a photonic ring counter which demonstrates the cascadability to a multi-bit storage register. In this same reference, an S-SEED was also used to demonstrate differential logic operations of *AND, OR, NOR,* and *NAND*, which are the fundamental operations necessary for the realization of an optical full-adder. Other methods of implementing digital optical logic using MQW modulators and threshold logic are also currently being developed [53, 54].

As these and other optical digital logic techniques become more mature, all-optical decimation filters will become realizable, thereby providing an optical digital output alternative.

3.4 Summary

The approach to optical oversampled A/D conversion proposed in this chapter is device independent, requiring only optical thresholding, subtraction and digital logic for implementation. There are many different methods by which to achieve these functions optically. In this chapter, we have focused our attention on the use of MQW modulators for the implementation of the optical oversampled A/D converter. We described the operation of optical quantization and the added benefits derived from using a symmetric configuration of the MQW modulator. The symmetric modulator produces a transfer characteristics which closely approximates the ideal hysteresis curve. It is insensitive to optical power supply fluctuations, provides optical gain, and shows good input/output isolation.

Next, we presented the theory underlying noninterferometric optical subtraction using a MQW modulator and showed how this static technique could be extended to dynamic, time varying applications. We formalized several specific realizations of the optical oversampled modulator based on the concepts of optical quantization and subtraction using MQW modulators. Finally, we proposed both an electronic and an optical implementation of the digital postprocessor. Using a photodetector, the one-bit digital optical output from the modulator can be converted to an electronic signal and existing electronic techniques can be used to implement the digital postprocessor. This would provide an electronic digital output word from

the A/D converter to use in current electronic applications. As optical digital computing becomes more mature, the digital postprocessor can be implemented using the same MQW modulators which were used in the modulator. This final implementation provides the capability for all-optical A/D conversion, something that was not possible with previous implementations of optical A/D converters.

There are several advantages associated with the use of MQW modulators. MQW modulators are multi-functional devices, capable of implementing all of the functions necessary to realize an optical oversampled A/D converter. They require low operating energies, comparable with current electronic devices with similar functionality. Switching speeds have been demonstrated to be 33 psec for a symmetric modulator, and theoretical lower limits have been projected to be 1-2 psec. Two-dimensional arrays of these modulators are also currently available, making image processing applications a logical extension.

MQW modulators are by no means the panacea of optical processing devices. The operation of the MQW modulator relies on the shift of the exciton absorption peaks with applied electric field. These exciton peaks are narrow and therefore, for optimum performance, require an accurate and stable laser wavelength. Also, since the entire system is discrete-time, accurate timing synchronization is required.

Chapter 4

Performance Analysis

THE PERFORMANCE ESTIMATES FOR THE OVERSAMPLED A/D CONVERTER described in Chapter 2 were based on ideal components and therefore represent an upper bound on achievable performance. Nonidealities such as arithmetic errors in the subtraction implementation, non-white quantization noise, and stage-to-stage matching errors all contribute to converter errors which result in sub-optimum performance of the oversampled A/D converter.

In this chapter, we examine sources of error in the oversampled error diffusion modulator which could reduce the performance estimates previously established for the oversampled A/D converter. We begin by examining the robustness of the modulator to linear errors associated with the subtraction operations. Next, the quantization noise spectra are analyzed and contrasted with the typical white noise assumption. Finally, we quantify errors and performance degradations associated with stage-to-stage matching tolerances in the two-stage cascade architecture.

4.1 Linear Arithmetic Errors

One of the benefits of an oversampled modulator often cited in the literature is its robustness against circuit imperfections. In this section, we quantify this statement.

Figure 4.1 shows the model of a first-order error diffusion modulator with linear

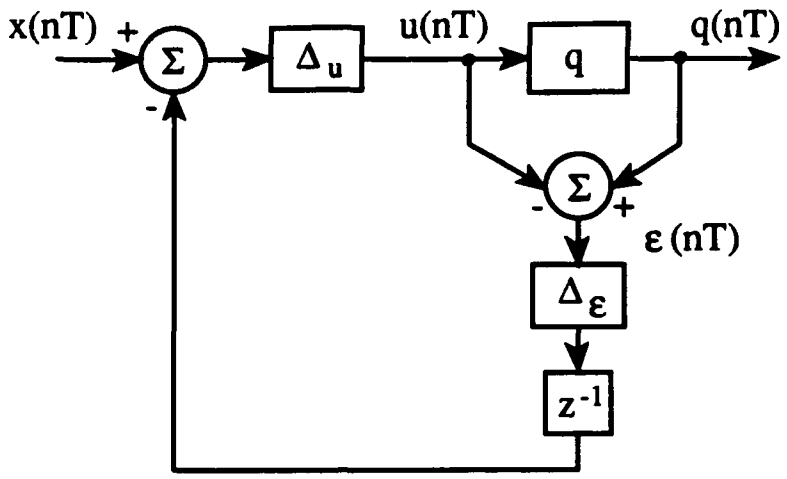

Figure 4.1: First-order error diffusion modulator error model.

errors Δ_u and Δ_ϵ. These errors represent gain errors associated with the subtraction operations in the modulator.

We begin by assuming a model for the quantizer non-linearity in the form of a linear gain plus an additive noise source,

$$q(u_n) = G_1 u_n + \epsilon_n. \tag{4.1}$$

If the operation of the feedback loop is assumed to force the effective loop gain to unity [55], then the quantizer output $q(u_n)$ is described by

$$q(u_n) = \frac{u_n}{\Delta_u \Delta_\epsilon} + \epsilon_n. \tag{4.2}$$

From Figure 4.1, the input to the memoryless uniform binary quantizer is

$$u_n = \Delta_u x_n - \Delta_u \Delta_\epsilon z^{-1} \epsilon_n \tag{4.3}$$

and therefore the output from the first-order error diffusion modulator is

$$q(u_n) = \frac{\Delta_u x_n - \Delta_u \Delta_\epsilon z^{-1} \epsilon_n}{\Delta_u \Delta_\epsilon} + \epsilon_n = \frac{x_n}{\Delta_\epsilon} + (1 - z^{-1})\epsilon_n. \tag{4.4}$$

The first term in Equation (4.4) represents a scaled version of the sampled analog input signal, where the scaling can be considered a gain mismatch. The absence of Δ_u is a direct consequence of the unity gain assumption made at the beginning of this analysis. The second term in Equation (4.4) represents the first-order noise shaping expected from this first-order modulator.

The robustness of the oversampled modulator to these linear errors can be best understood in terms of gain errors. The linear errors introduced in this analysis do not contribute to the overall quantization noise nor do they effect the noise shaping function of the modulator. As long as the gain error is independent of the input signal amplitude, no distortion occurs and the error can be accounted for and corrected in the postprocessor function. Therefore, in terms of SQNR, which is a relative rather than absolute measure of performance, linear errors do not adversely effect the overall modulator performance (assuming they are not time varying errors).

4.2 Quantization Noise Spectra

4.2.1 Background

It is extremely important to characterize the quantization noise in an oversampled modulator in terms of its statistical properties. These properties are used in the evaluation of the modulator performance and ultimately determine the resolution of the oversampled A/D converter. Previous results can be extended to new modulator configurations such as the optical error diffusion modulator.

The interferometric optical modulator processes complex amplitude optical signals and can therefore be considered an optical dual of the electronic oversampled modulator. As a result, the quantization noise characteristics can be shown to be identical to those of its electronic counterpart. We therefore refer the interested reader to the classic papers on oversampled $\Sigma\Delta$ quantization noise spectra by Gray *et al.* [56, 57, 58, 59, 26].

The noninterferometric optical modulator, however, is much more interesting

and is therefore the focus of this theoretical noise analysis. Unlike the interferometric optical modulator, the noninterferometric modulator operates only on optical intensities, and does not process phase information. Therefore all signals within the modulator are necessarily non-negative.

4.2.2 Methodology

There are several different approaches to the characterization of the quantization noise in an oversampled modulator. The most popular approach is to model the quantizer as an additive noise source where the noise is assumed to be uniformly distributed, white and uncorrelated with the input. With these assumptions the nonlinear system is linearized thereby allowing analysis with linear transform techniques. Another approach uses the describing function method from control theory, in which the quantizer non-linearity is modeled as a gain plus an additive noise source. In this case, the gain is matched to the transfer characteristic of the first harmonic of the input, which is a single sinusoid. The noise is still assumed to be uniformly distributed, white and uncorrelated, but now the variance is matched to that of the system by minimizing the mean square error [60, 61]. Both of these techniques approximate the operation of the modulator by linearizing a highly nonlinear system. Recently, Gray derived exact analytic expressions for the spectral characteristics of the quantization noise in oversampled $\Sigma\Delta$ modulators without resorting to linearizing assumptions. By restricting the quantizer operation to be within the no-overload region and recognizing the periodicity of the quantization error, Fourier series techniques were used to derive closed form solutions to the nonlinear difference equations.

4.2.3 Noninterferometric Noise Spectra

Figure 4.2 shows the equivalent block diagram of the first-order optical noninterferometric modulator. We describe the operation of this modulator by the difference

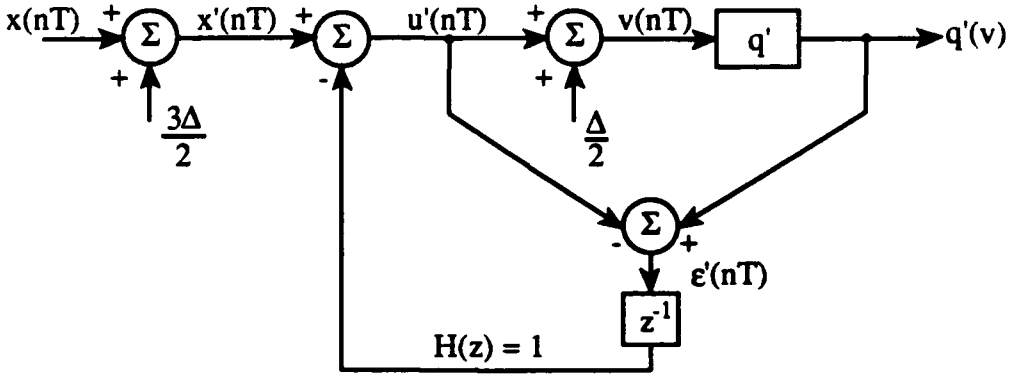

Figure 4.2: Block diagram of a first-order noninterferometric error diffusion modulator.

equations

$$v_n = \begin{cases} v_0; & \text{n=0} \\ x'_n - \epsilon'_{n-1} + \frac{\Delta}{2} = x'_n - q'(v_{n-1}) + u'_{n-1} + \frac{\Delta}{2}; & \text{n=1, 2, ...} \end{cases} \tag{4.5}$$

As in earlier analyses, $x_n \in [-b, +b)$; $n = 1, 2, \ldots$ is the discrete-time input formed by oversampling the analog input signal $x(t)$, and $[a, b) = \{x : a \leq x < b\}$ represents the half-open interval. x'_n is the non-negative input to the modulator generated by adding a bias of $3\Delta/2$ to the input thereby ensuring $x'_n \geq 0$. v_n is the quantizer input, u'_0 and subsequently v_0 are the quantizer input initial conditions and $q'(v_n)$ is the memoryless uniform binary quantizer defined by

$$q'(v_n) = \begin{cases} 2\Delta & \text{if } v_n \geq v_{th} = \frac{3\Delta}{2} \\ \\ \Delta & \text{if } v_n < v_{th} = \frac{3\Delta}{2} \end{cases} \tag{4.6}$$

where Δ is the quantizer bin width and v_{th} is the quantizer threshold. We will assume for convenience that $u'_0 = 0$, which implies $v_0 = \Delta/2$. In the optical architecture, this amounts to resetting the quantizer at the end of each bit period. Mathematically, this assumption has no effect on the asymptotic results but greatly simplifies the algebra.

We define the quantizer error sequence as

$$\epsilon_n \equiv \begin{cases} \frac{\Delta}{2}; & n=0 \\ \\ q'(v_n) - v_n = x'_{n+1} - v_{n+1}; & n=1,2,\ldots \end{cases} \tag{4.7}$$

where the definition of ϵ_0 follows from v_0 and $q'(v_n)$ and the second equality from Equation (4.5).

Before beginning the noise analysis, we must establish the relationship between Δ and b, so that Δ can be chosen to ensure the quantizer does not overload provided $x_n \in [-b, +b)$; $n = 1, 2, \ldots$. We use mathematical induction to find this relationship. If $\epsilon_0 = \Delta/2$ and $x'_n \in [-b + 3\Delta/2, b + 3\Delta/2)$, then to ensure $\Delta/2 \leq v_1 \leq 5\Delta/2$ we must have that

$$\frac{\Delta}{2} \leq x'_1 - \frac{\Delta}{2} \leq \frac{5\Delta}{2} \tag{4.8}$$

and therefore

$$b \leq \frac{\Delta}{2}. \tag{4.9}$$

We now show that this is a sufficient condition to ensure that the quantizer does not overload. We have already proven this for $n = 1$, so we proceed by induction by first assuming that it is true for $n = 1, 2, \ldots, k-1$. By definition of no overload, if $v_{k-1} = x'_{k-1} - \epsilon'_{k-2} + \Delta/2$ is within the no overload region $\Delta/2 \leq v_{k-1} \leq 5\Delta/2$ then $|\epsilon_{k-1}| \leq \Delta/2$. Therefore we need only prove that it is not possible for either $v_{k-1} > 5\Delta/2$ or $v_{k-1} < \Delta/2$. It is easy to show that if $|\epsilon_{k-1}| \leq \Delta/2$, then $0 \leq \epsilon'_{k-1} \leq \Delta$. With this property and the range of x'_n we have that

$$-b + \Delta \leq x'_k - \epsilon'_{k-1} + \frac{\Delta}{2} \leq b + 2\Delta \tag{4.10}$$

and using Equation (4.9) that

$$\frac{\Delta}{2} \leq v_k = x'_k - \epsilon'_{k-1} + \frac{\Delta}{2} \leq \frac{5\Delta}{2}, \tag{4.11}$$

proving that the quantizer does not overload for all $n = k$. The upper bound of Equation (4.9) is chosen for the quantizer bin width Δ ($\Delta = 2b$), consistent with the most common choice for oversampled quantizer output levels and providing the full extremes of the input as the possible quantizer outputs.

Now that we have proven that the quantizer does not overload, we proceed with the statistical characterization of the quantization noise. Following Gray's approach, we first recast the difference equations in an alternative form that permits us to solve the equations and directly evaluate limiting sample averages. Toward this end, we consider the normalized and shifted error sequence

$$\xi_n = \frac{1}{2} - \frac{\epsilon_{n-1}}{\Delta} = \frac{v_n}{\Delta} + \frac{1}{2} - \frac{x'_n}{\Delta};\ n=1, 2, \ldots \tag{4.12}$$

The following relations summarize the sequences of interest within the noninterferometric modulator and how each can be derived from ξ_n:

$$\zeta_n \equiv \frac{\epsilon_n}{\Delta} = \frac{1}{2} - \xi_{n+1} = \frac{x'_{n+1}}{\Delta} - \frac{v_{n+1}}{\Delta} \tag{4.13}$$

$$\frac{v_n}{\Delta} = \xi_n - \frac{1}{2} + \frac{x'_n}{\Delta} \tag{4.14}$$

$$q'_n = \frac{q'(v_n)}{\Delta} = \frac{v_n - v_{n+1}}{\Delta} + \frac{x'_{n+1}}{\Delta} + \frac{3}{2} = \xi_n - \xi_{n+1} + \frac{x'_{n+1}}{\Delta}. \tag{4.15}$$

With the exception of an additional delay incurred by the biased input, these equations represent the equivalent of those derived by Gray for the single-loop $\Sigma\Delta$ modulator [58]. Therefore, the quantization noise in the first-order noninterferometric optical modulator can be expected to have the same statistical characteristics as those of the single-loop $\Sigma\Delta$ modulator. For completeness, we summarize the quantization noise characteristics for both dc and sinusoidal input cases as well as one- and two-stage cascaded modulators below. The complete derivation of the following quantization noise characteristics can be found in [57, 58, 26].

We define the time average mean of the normalized quantizer error sequence as

$$\overline{E}\{\zeta_n\} = \lim_{N\to\infty} \frac{1}{N} \sum_{n=1}^{N} \zeta_n, \tag{4.16}$$

and the time average variance or second moment as

$$\overline{E}\{\zeta_n^2\} = \lim_{N\to\infty} \frac{1}{N} \sum_{n=1}^{N} \zeta_n^2. \tag{4.17}$$

We can show for a first-order modulator with a dc input, $x_n = x$ for all n, where $-b \leq x_n < b$ is an *irrational* number, the time-average mean of the quantizer error sequence is

$$\overline{E}\{\zeta_n\} = 0 \tag{4.18}$$

and the time-average variance is

$$\overline{E}\{\zeta_n^2\} = \frac{1}{12}. \tag{4.19}$$

Therefore, the normalized binary quantizer error sequence has mean and variance identical to those of a uniformly distributed random variable on the same interval of $[-1/2, +1/2]$.

The power spectrum of this quantizer error sequence is discrete with amplitudes given by

$$S_\epsilon(f_n) = \begin{cases} 0; & n = 0 \\ \frac{1}{(2\pi n)^2}; & n \neq 0 \end{cases} \tag{4.20}$$

located at frequencies

$$f_n = \langle \frac{n(b + x'_n)}{2b} \rangle; \quad n \neq 0 \tag{4.21}$$

where $0 \leq < r > < 1$ is the fractional part of r (r mod 1). The cross correlation between the input and the normalized quantizer error is

$$\overline{E}\{x_n \zeta_n\} = x_n \overline{E}\{\zeta_n\} = 0 \tag{4.22}$$

and therefore the input and the binary quantizer noise are uncorrelated.

For completeness, we also include the expression for the power spectrum of the quantizer output sequence which is also discrete, with amplitudes given by

$$S_{q'}(f_n) = \begin{cases} \left(\frac{x'_n}{2b}\right)^2; & n = 0 \\ \frac{\sin^2(n\pi\beta)}{(n\pi)^2}; & n \neq 0 \end{cases} \tag{4.23}$$

located at frequencies given by Equation (4.21). Here $\beta = 1/2 + x'_n/2b$.

For the first-order error diffusion modulator driven by a sinusoidal input ($x_n = a\cos(n\omega_0)$, $|a| \leq b$) and the special case of $a = b$, the time-average mean is

$$\overline{E}\{\zeta_n\} = 0 \tag{4.24}$$

and in the general case of $a \neq b$ and for large oversampling ratios

$$\overline{E}\{\zeta_n\} \approx 0. \tag{4.25}$$

The time-average variance is

$$\overline{E}\{\zeta_n^2\} = \frac{1}{12} + \frac{1}{4\pi^2}\sum_{l=1}^{\infty}\frac{1}{l^2}(-1)^l J_0(4\pi l\alpha) \tag{4.26}$$

where

$$\alpha = \frac{a}{2\Delta \sin\frac{\omega_0}{2}}. \tag{4.27}$$

Equation (4.26) is approximately 1/12 when α is large. The power spectrum again consists of discrete components, but now with amplitude

$$S_\epsilon(f_n) = \begin{cases} \frac{1}{2}; & n = 0 \\ \left(\frac{1}{\pi}\sum_{l=0}^{\infty}\frac{J_n(2\pi\alpha(2l-1))}{2l-1}(-1)^l\right)^2; & n \text{ even} \\ \left(\frac{1}{\pi}\sum_{l=0}^{\infty}\frac{J_n(4\pi\alpha l)}{2l}(-1)^l\right)^2; & n \text{ odd} \end{cases} \tag{4.28}$$

located at frequencies

$$f_n = \begin{cases} \langle\frac{n\omega_a}{2\pi} - \frac{1}{2}\rangle; & n \text{ even} \\ \langle\frac{n\omega_a}{2\pi}\rangle; & n \text{ odd} \end{cases} \tag{4.29}$$

In Equation (4.28), J_n is a Bessel function of the first kind, with order n. The input and the binary quantizer error in this case, however, are *not* asymptotically uncorrelated as in the dc input case.

In the case of a second-order modulator, an irrational dc input produces quantization noise that has the same marginal and joint moments as a uniform *white* process. If the input signal is instead a sinusoid, the resulting quantization noise is not white but becomes asymptotically uncorrelated as the oversampling ratio grows. For a sinusoidal input, a third-order modulator is required to produce uniform white quantization noise.

Observations:

From these results, we can now characterize the quantization noise in the non-interferometric optical modulator.

(1) The quantization noise in the first-order error diffusion modulator will be non-white with discrete spectral components for both dc and sinusoidal inputs.

(2) The location of the discrete spectral peaks is directly proportional to the input signal amplitude.

(3) For a second-order modulator, the quantization noise will have white noise characteristics for a dc input and non-white characteristics for a sinusoidal input.

We anticipate the optical modulator will be used in an oversampled A/D converter with a large oversampling ratio for which the input can be approximated as a slowly varying signal, *i.e.* a dc input. Therefore, a second-order modulator is necessary to achieve the desired white quantization noise characteristics.

Using a mixed digital and analog simulation program called MIDAS [62], we simulated the operation of the first-order noninterferometric modulator shown in Figure 4.2 and the second-order noninterferometric cascade modulator shown in Figure 4.3. Figure 4.4 shows the quantization noise spectrum of the quantizer in the first-order noninterferometric optical modulator. In this case the oversampling ratio, $M = f_S/f_N$ where f_S is the sampling frequency and f_N is the Nyquist frequency, was 256, 4096 data points were computed, and the dc input was irrational; $x = 1/\pi$. The spectrum of the quantization noise is clearly not white, but contains discrete spectral peaks as predicted by this analysis. Figure 4.5 shows the quantization noise spectrum for the same modulator but with a different irrational dc input value; $1/2e$. As predicted by Equation (4.21), the location of the spectral peaks changes showing the proportionality to the input amplitude.

Figure 4.6 shows the quantization noise spectrum of the second-stage quantizer in the second-order cascade modulator using the same parameters as used in Figure 4.4. This quantization noise spectrum is white and consistent with the theoretical predictions of the quantization noise spectrum of a second-order modulator with an irrational dc input.

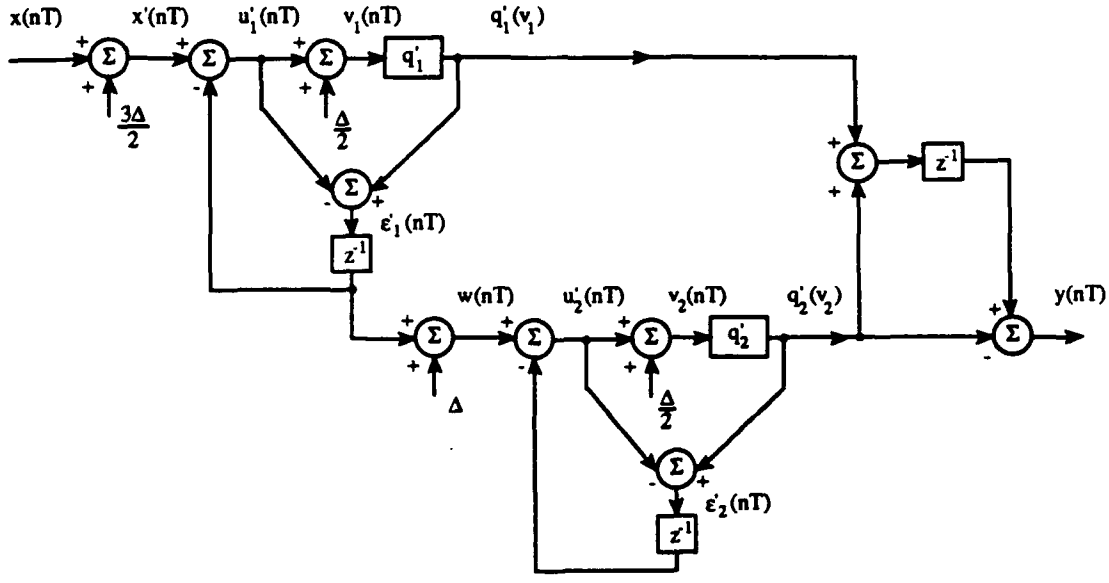

Figure 4.3: Second-order noninterferometric cascade modulator.

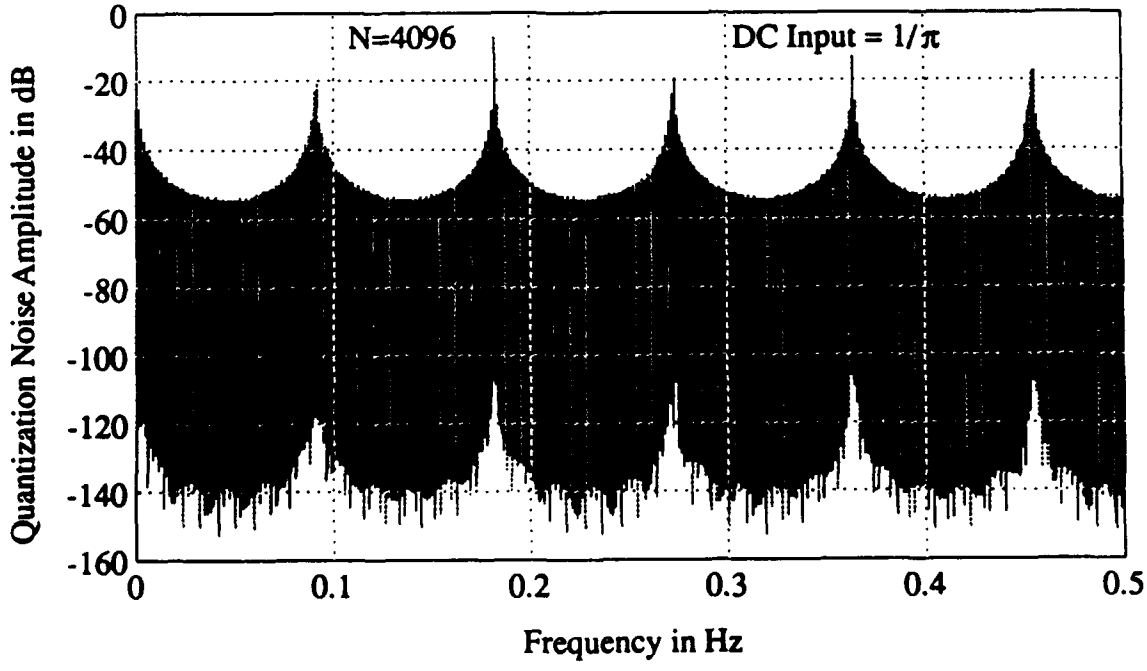

Figure 4.4: First-stage quantizer noise spectrum; $x_n = 1/\pi$.

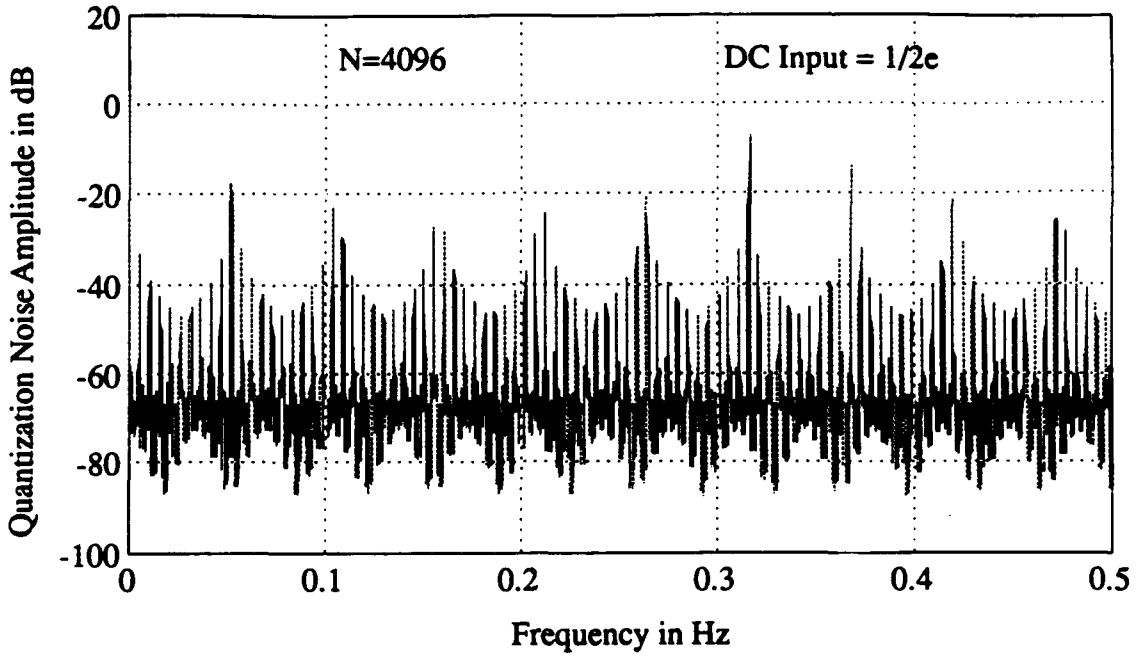

Figure 4.5: First-stage quantizer noise spectrum; $x_n = 1/2e$.

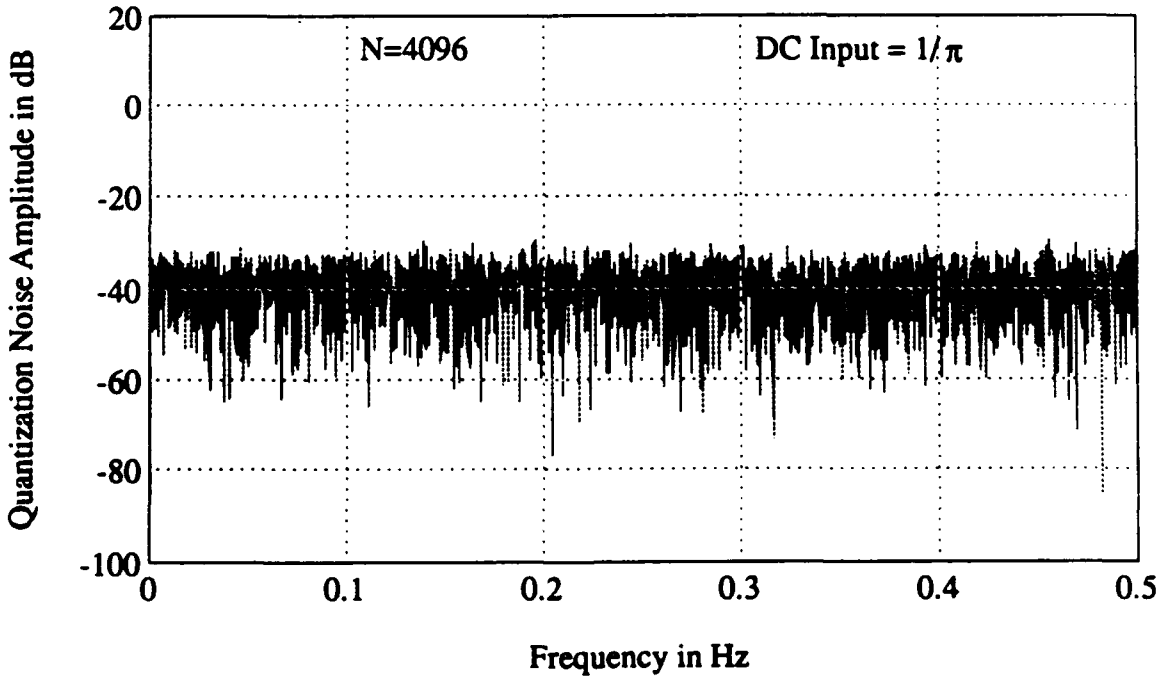

Figure 4.6: Second-stage quantizer noise spectrum; $x_n = 1/\pi$.

4.3 Cascade Error Tolerances

Multi-loop oversampled modulators provide improved amplitude resolution directly proportional to the order N of the modulator and the N_{th}-power of the oversampling ratio f_S/f_N. For $N > 2$, these modulator architectures suffer from instability resulting from limit cycles. One method of achieving higher-order noise shaping without stabilization problems is to use a cascade of single-loop modulators, often referred to as a cascade or multi-stage modulator [30]. This type of architecture can be shown to be no-overload stable, but generally requires strict stage-to-stage matching tolerances. In the following analysis, we model gain errors and errors associated with the subtraction nodes in a second-order cascade error diffusion modulator and analytically describe the impact on the noise shaping characteristics of the modulator and the overall performance of the oversampled A/D converter.

4.3.1 Ideal Noise Canceling

Consider the two-stage error diffusion coding architecture shown in Figure 4.7. The filter transfer functions $H_1(z)$ and $H_2(z)$ comprise a linear combinatorial network which is used to cancel residual quantization noise from the first-stage modulator. In the ideal case, the filter transfer characteristics which achieve this result are

$$\begin{aligned} H_1(z) &= z^{-1} \\ H_2(z) &= -(1 - z^{-1}), \end{aligned} \tag{4.30}$$

and Figure 4.7 can be equivalently represented as shown in Figure 4.8. In order to quantify the noise canceling performance, we again model the quantizer nonlinearity as a linear gain plus an additive noise source

$$\begin{aligned} q_1(u_1) &= G_1 u_1 + \varepsilon_1 \\ q_2(u_2) &= G_2 u_2 + \varepsilon_2 \end{aligned} \tag{4.31}$$

and assume that the feedback loop forces the effective loop gain to unity. From Figure 4.8, the input to each individual memoryless uniform binary quantizer is

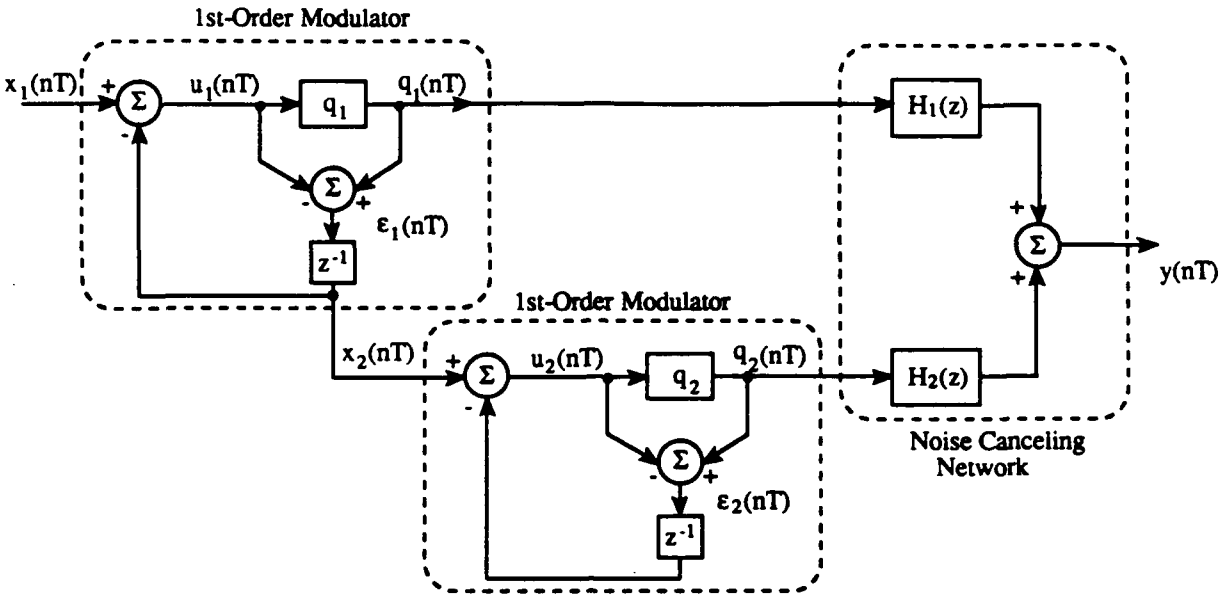

Figure 4.7: Ideal two-stage error diffusion modulator.

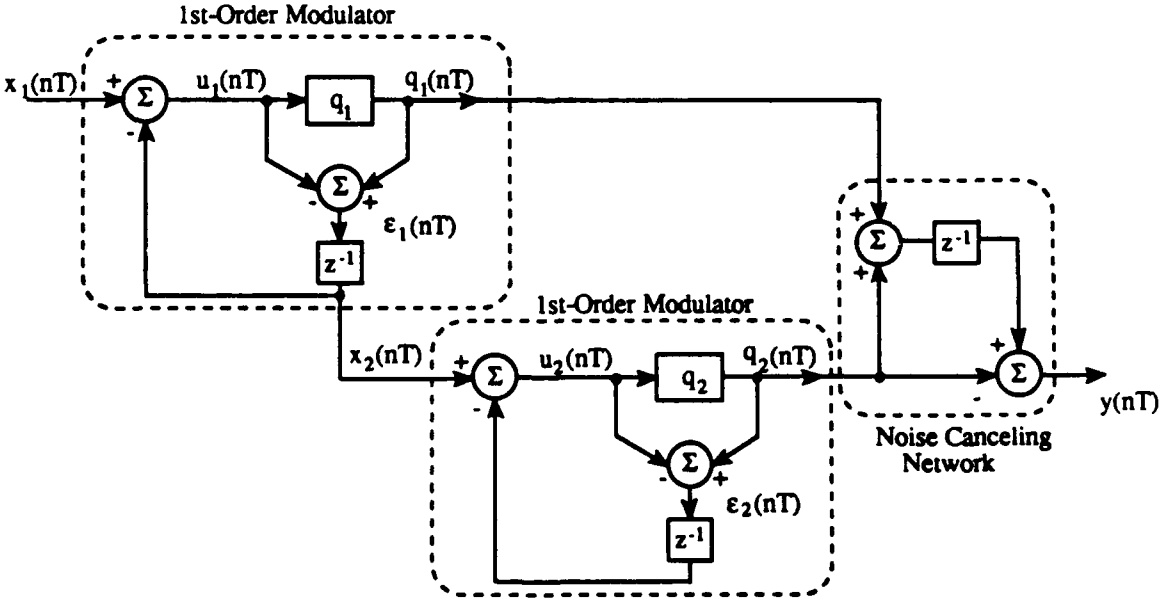

Figure 4.8: Ideal two-stage error diffusion modulator.

$$u_1 = x_1 - z^{-1}\varepsilon_1$$
$$u_2 = x_2 - z^{-1}\varepsilon_2 \tag{4.32}$$

and therefore the output from the two first-order modulators can be described as

$$q_1(u_1) = x_1 - z^{-1}\varepsilon_1 + \varepsilon_1 = x_1 + (1 - z^{-1})\varepsilon_1 \tag{4.33}$$

and

$$q_2(u_2) = x_2 - z^{-1}\varepsilon_2 + \varepsilon_2 = x_2 + (1 - z^{-1})\varepsilon_2. \tag{4.34}$$

Equations (4.33) and (4.34) clearly show the first-order noise shaping characteristics expected of both stages. We also know from Figure 4.8 that the input to the second-stage modulator is

$$x_2 = z^{-1}\varepsilon_1. \tag{4.35}$$

The modulator output y_n can be represented as a linear combination of the output from the two first-order modulators as

$$y_n = [q_1(u_1) + q_2(u_2)]z^{-1} - q_2(u_2). \tag{4.36}$$

Substitution of Equations (4.33), (4.34), and (4.35) into Equation (4.36) leads to the two-stage modulator output

$$y_n = x_1 z^{-1} - (1 - z^{-1})^2\varepsilon_2. \tag{4.37}$$

Equation (4.37) contains no first-stage quantizer noise terms which indicates that the noise canceling network has completely removed all of the first-stage quantization noise, ε_1. The only remaining quantization noise present in the output is from the second-stage quantizer and is shaped by the second-order filtering function $(1 - z^{-1})^2$, as desired.

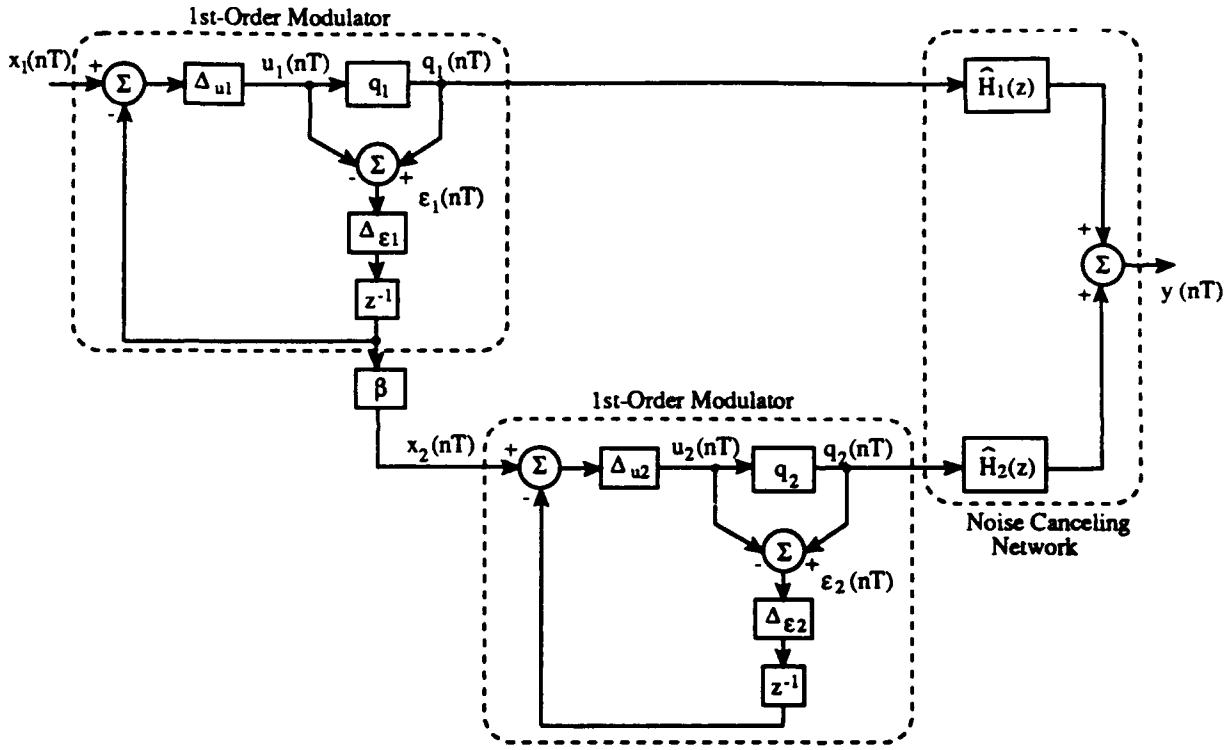

Figure 4.9: Two-stage error diffusion modulator cascade error tolerance model.

4.3.2 Non-Ideal Noise Canceling

In this section we introduce non-idealities in the two-stage cascade modulator. Figure 4.9 shows the two-stage error diffusion modulator with associated error contributions. In this analysis, we will assume that

$$\begin{aligned} \Delta_{u_i} &\equiv (1 - \delta_{u_i}), \quad i = 1, 2 \\ \Delta_{e_i} &\equiv (1 - \delta_{e_i}), \quad i = 1, 2. \end{aligned} \tag{4.38}$$

represent fractional errors in the subtraction nodes. In this case, the noise canceling network is represented by $\hat{H}_1(z)$ and $\hat{H}_2(z)$ where the $\hat{H}$ indicates the gain mismatch between the analog and digital coefficients. The filter transfer functions are now

$$\begin{aligned} \hat{H}_1(z) &= \hat{\gamma} z^{-1} \\ \hat{H}_2(z) &= -\frac{1}{\hat{\beta}}(1 - z^{-1}) \end{aligned} \tag{4.39}$$

where

$$\hat{\gamma} \equiv \frac{\hat{\Delta}_{\varepsilon_1}}{\hat{\Delta}_{\varepsilon_2}} \tag{4.40}$$

and

$$\begin{aligned} \beta &= \hat{\beta}(1-\delta_\beta) \\ \Delta_{\varepsilon_i} &= \hat{\Delta}_{\varepsilon_i}(1-\delta_{\Delta_{\varepsilon_i}}) \quad i=1,2. \end{aligned} \tag{4.41}$$

We begin with the same quantizer model assumptions as in Section 4.3.1 and therefore the quantizer outputs $q_1(u_1)$ and $q_2(u_2)$ are given by Equation (4.31) but now with unity effective loop gain, the quantizer output from each stage is described by

$$\begin{aligned} q_1(u_1) &= \frac{u_1}{\Delta_{u_1}\Delta_{\varepsilon_1}} + \varepsilon_1 \\ q_2(u_2) &= \frac{u_2}{\Delta_{u_2}\Delta_{\varepsilon_2}} + \varepsilon_2. \end{aligned} \tag{4.42}$$

From Figure 4.9, the input to each memoryless uniform binary quantizer is

$$\begin{aligned} u_1 &= \Delta_{u_1}x_1 - \Delta_{u_1}\Delta_{\varepsilon_1}z^{-1}\varepsilon_1 \\ u_2 &= \Delta_{u_2}x_2 - \Delta_{u_2}\Delta_{\varepsilon_2}z^{-1}\varepsilon_2 \end{aligned} \tag{4.43}$$

and therefore the quantizer output sequence from the two first-order modulators is

$$q_1(u_1) = \frac{\Delta_{u_1}x_1 - \Delta_{u_1}\Delta_{\varepsilon_1}z^{-1}\varepsilon_1}{\Delta_{u_1}\Delta_{\varepsilon_1}} + \varepsilon_1 = \frac{x_1}{\Delta_{\varepsilon_1}} + (1-z^{-1})\varepsilon_1 \tag{4.44}$$

and

$$q_2(u_2) = \frac{\Delta_{u_2}x_2 - \Delta_{u_2}\Delta_{\varepsilon_2}z^{-1}\varepsilon_2}{\Delta_{u_2}\Delta_{\varepsilon_2}} + \varepsilon_2 = \frac{x_2}{\Delta_{\varepsilon_2}} + (1-z^{-1})\varepsilon_2. \tag{4.45}$$

Equations (4.44) and (4.45) again show the first-order noise shaping characteristics of both stages. We know from Figure 4.9 that

$$x_2 = \Delta_{\varepsilon_1}\beta z^{-1}\varepsilon_1. \tag{4.46}$$

Representing the modulator output as a linear combination of the output from the two first-order modulators,

$$y_n = \hat{H}_1(z)q(u_1) + \hat{H}_2(z)q(u_2). \tag{4.47}$$

Substitution of Equations (4.38), (4.44), (4.45), and (4.46) into Equation (4.47) leads to the two-stage modulator output

$$y_n \approx \frac{z^{-1}}{\Delta_{\epsilon_1}} x_1 + \delta_{\epsilon_T}(1 - z^{-1})z^{-1}\epsilon_1 - \frac{1}{\hat{\beta}}(1 - z^{-1})^2\epsilon_2, \tag{4.48}$$

where

$$\delta_{\epsilon_T} \approx \delta_{\Delta_{\epsilon_1}} + \delta_{\Delta_{\epsilon_2}} + \delta_{\beta} \tag{4.49}$$

is the cumulative matching error and the approximation results from neglecting higher order terms.

The first term in Equation (4.48) represents a scaled and delayed version of the input signal x_1. The second term represents a scaled version of the first-stage quantization error which was not fully canceled by the noise canceling network as a result of stage-to-stage matching errors. The final term is a scaled version of the second-stage quantizer noise which is shaped by a second-order filter response.

Observations:

(1) If there is no cumulative matching error ($\delta_{\epsilon_T} = 0$), the first-stage quantizer noise is completely canceled, and only the quantization noise from the second-stage appears at the output after undergoing second-order noise shaping.

(2) If the matching errors are not zero, the first-stage quantization noise is not completely canceled. However, because Equation (4.48) depends on the sum of errors and not the absolute error, the errors can offset each other.

(3) Neither Δ_{u_1} nor Δ_{u_2} appear in the output of the overall modulator. This is a direct result of assuming that the feedback loop forces the loop gain to unity.

In order to determine the impact of these errors on the signal-to-quantization-noise ratio (SQNR), first assume the input x_1 is a sinusoid with peak-to-peak amplitude $2A_{x_1}$. If the error terms in the modulator are assumed to be random and uncorrelated with each other and the input, then it follows from Equations (4.47)

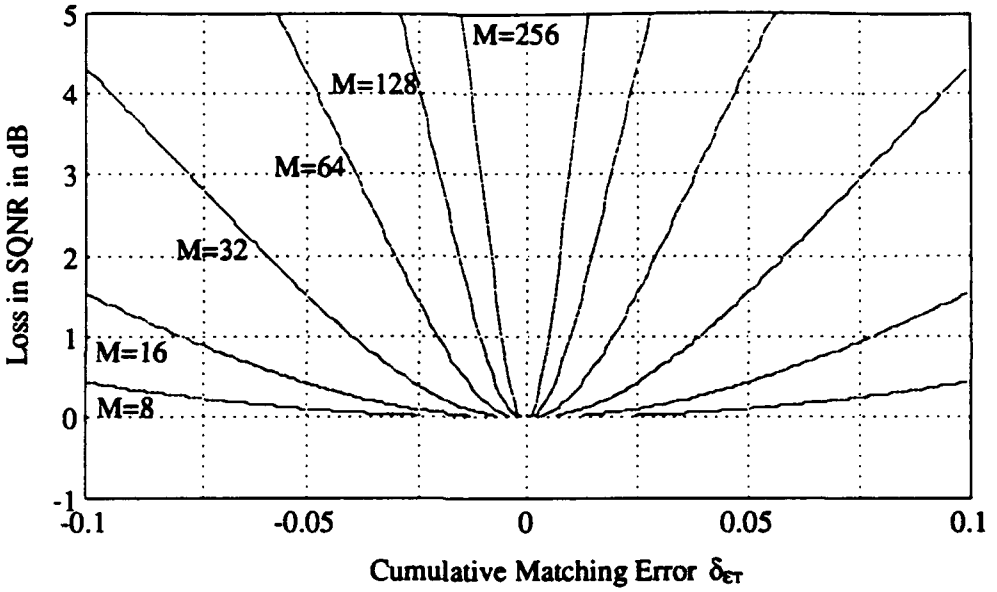

Figure 4.10: Loss in SQNR as a function of cumulative matching error δ_{ϵ_T} and oversampling ratio M.

and (2.17) with $N = 2$ that the SQNR as a function of matching errors is approximately

$$SQNR(\delta_{\epsilon_T}) \approx \left(\frac{A_{x_1}}{\Delta_{\epsilon_1}}\right)^2 \left[\delta_{\epsilon_T}^2 \frac{\pi^2}{18M^3} + \frac{1}{\hat{\beta}^2}\frac{\pi^4}{30M^5}\right]^{-1}, \tag{4.50}$$

where M is the oversampling ratio f_S/f_N.

If we define Δ_{SQNR} as the fractional reduction in the SQNR due to matching errors, then

$$\Delta_{SQNR} \equiv \frac{SQNR(0)}{SQNR(\delta_{\epsilon_T})} \approx 1 + \frac{5}{3}\hat{\beta}^2\frac{M^2}{\pi^2}\delta_{\epsilon_T}^2. \tag{4.51}$$

Therefore, the reduction in SQNR is proportional to the square of the oversampling ratio and the matching error. The loss in SQNR as a function of δ_{ϵ_T} and the oversampling ratio M is shown in Figure 4.10. In this case, $\hat{\beta}$ is assumed to be unity. This figure clearly shows the trade-off between matching tolerance accuracy and oversampling ratio. For an oversampling ratio of $M = 64$, $\pm 5\%$ cumulative matching error results in a loss in SQNR of 4.2 dB while if $M = 128$, a $\pm 2.5\%$ reduction in the cumulative matching error is required to maintain the same loss in

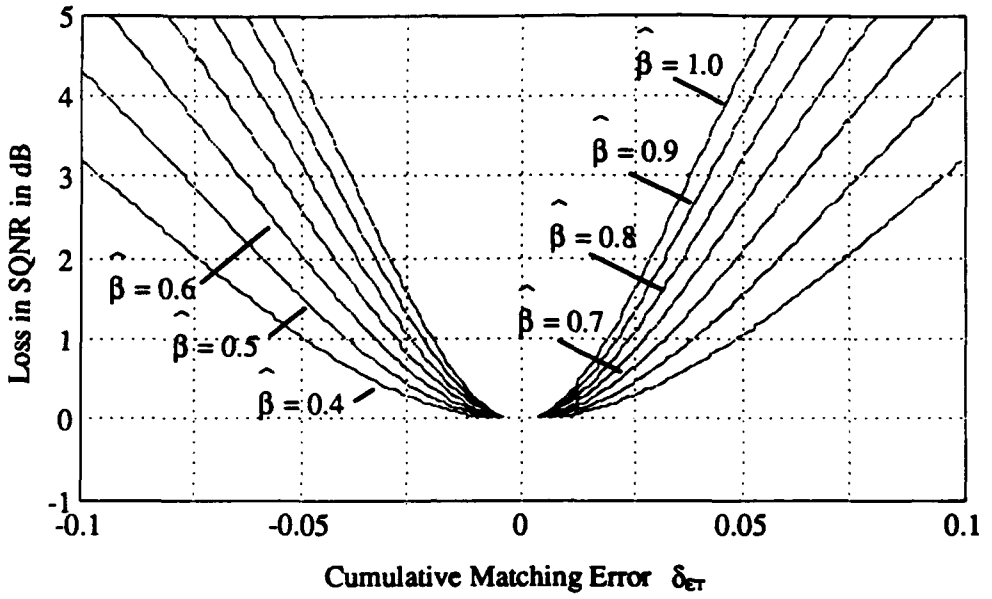

Figure 4.11: Loss in SQNR as a function of cumulative matching error δ_{ϵ_T} and digital filter coefficient $\hat{\beta}$.

SQNR. Figure 4.11 shows the loss in SQNR as a function of δ_{ϵ_T} and $\hat{\beta}$ for the case $M = 64$.

In order to verify these analytic results, we simulated the operation of the cascade modulator under conditions of cumulative matching errors using the special purpose simulator MIDAS [62], which has previously shown good agreement with experiment. MIDAS is a functional simulator for mixed digital and analog sampled-data systems which is well suited to the evaluation of the long data traces needed to study the behavior of oversampled modulators.

To examine the consequences of the cumulative matching error on the performance of the two-stage cascade oversampled modulator, a number of simulations were performed in a Monte Carlo fashion using random values for the errors $\delta_{\Delta_{\epsilon_1}}$, $\delta_{\Delta_{\epsilon_2}}$, and δ_{β}. The resulting loss in SQNR as a function of the cumulative matching error δ_{ϵ_T} is shown in Figure 4.12 for the case $\hat{\beta} = 1$ and M=64. Figure 4.12 shows that the analytic model of Equation (4.51) agrees well with the simulation results and also confirms the assertion that the loss in SQNR is dependent on the sum of

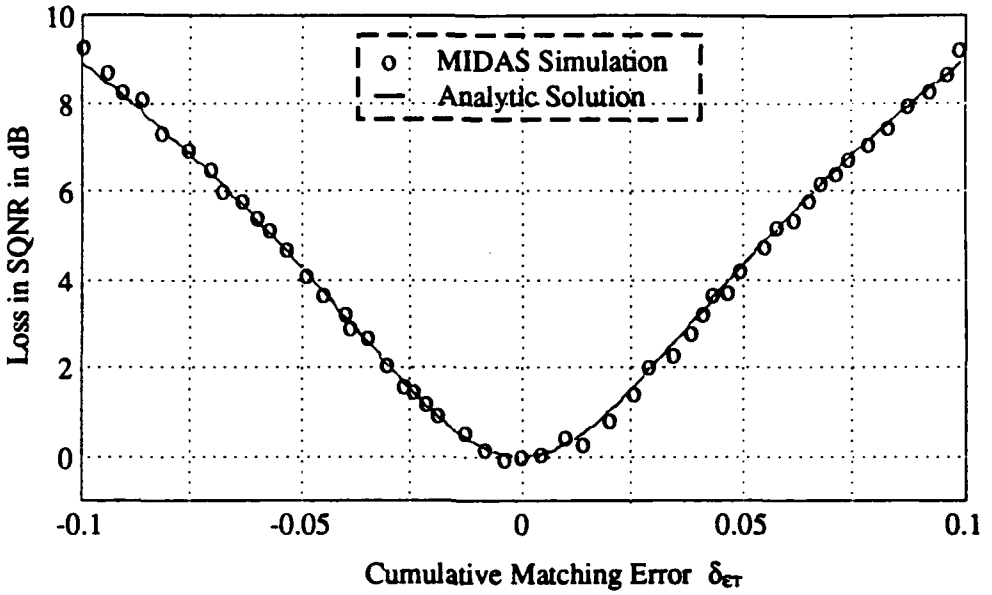

Figure 4.12: Loss in SQNR as a function of δ_{ϵ_T} where $\hat{\beta} = 1$ and M=64.

the matching errors and not on the absolute error. In executing the simulation, each error was selected from a zero-mean, uniformly distributed ensemble that was constrained to satisfy $|\delta_{\epsilon_T}| \leq 0.1$, where recall that $\delta_{\epsilon_T} \approx \delta_{\Delta_{\epsilon_1}} + \delta_{\Delta_{\epsilon_2}} + \delta_{\beta}$.

4.4 Summary

In this chapter, we modeled three types of errors in the oversampled modulator and determined the impact each had on overall converter performance. Linear arithmetic errors resulting from non-ideal subtraction operations result in a linear scaling of the analog sampled input signal at the modulator output. This scaling or gain mismatch can be accounted for and corrected in the postprocessor, as long as the linear errors are signal independent and known a priori. These linear modulator errors do not change the noise shaping characteristics of the modulator nor do they introduce additional noise sources and therefore do not degrade the overall converter SQNR performance.

Discrete spectral tones, which result from non-white quantization noise can, however, produce serious performance degradations depending on the particular A/D converter application. The spectral characteristics of the quantization noise were shown to be closely related to the order of the modulator and whether the input is a dc or sinusoidal signal. In order to reduce the spectral tones, higher-order modulators which whiten the quantization noise characteristics are required. In order to ensure white quantization noise characteristics, a second-order modulator is required for a dc input and a third-order modulator is required for a sinusoidal input, respectively.

Finally, stage-to-stage cascade matching tolerances were investigated and found to be a major influence on converter performance. For a two-stage cascade modulator with an oversampling ratio of $M = 128$, we found that a cumulative matching error of $\pm 2.5\%$ resulted in a degradation in the converter SQNR of 4 dB.

Chapter 5

Optical Modulator Demonstration

THE DESIGN CONSIDERATIONS AND ANALYSES ADDRESSED IN CHAPTERS 3 and 4 have been applied to the implementation of a first-order noninterferometric optical modulator. The fundamental optical device used in this design is the reflection-type MQW modulator with a Fabry-Perot cavity. The objective of this demonstration is to verify theoretical concepts developed previously and to show the feasibility of optical oversampled modulation. It must be emphasized that this demonstration is to show proof-of-concept operation only, and not to demonstrate the full potential of an optical oversampled modulator.

In this chapter, we describe experimental demonstration of the theoretical concepts developed earlier. Specifically, we demonstrate, for the first time, the operation of noninterferometric optical subtraction using a reflection-type MQW modulator with a Fabry-Perot cavity and analyze the accuracy of this subtraction technique. We then demonstrate dynamic operation of a first-order optical error diffusion modulator with a constant optical input. From this data, we compute the accuracy of the quantizer output sample average and analyze sources of error in the experimental modulator. Next, the experimental power spectral density of the modulator output is compared with the analytic expression developed in Chapter 4. From the results of this experimental demonstration, we are then able to predict operating characteristics and performance capabilities of the optical modulator and optical oversampled A/D converter.

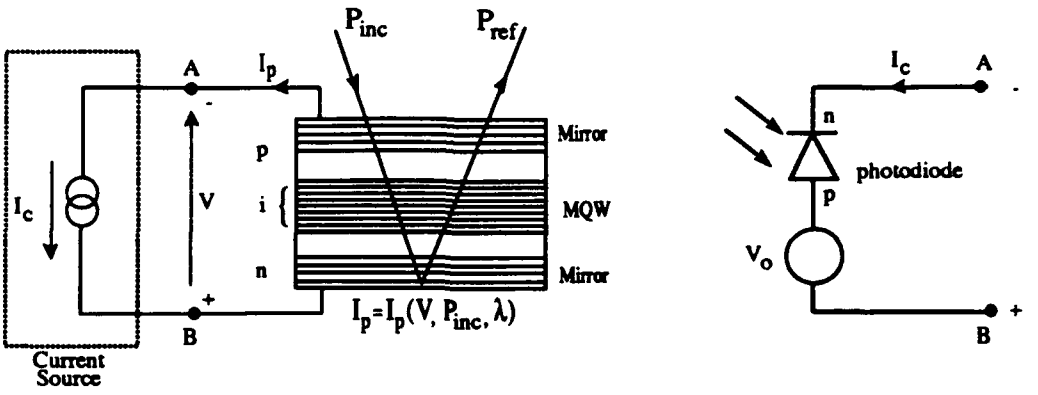

Figure 5.1: Structure and configuration of the reflection electroabsorption modulator for noninterferometric subtraction. (a) idealized circuit with a constant current source, (b) an optical realization of the constant current source.

5.1 Noninterferometric Optical Subtraction

In this section, we present experimental results of noninterferometric optical subtraction using a MQW modulator. The modulator used was a normally-on reflection electroabsorption modulator (REAM) with a Fabry-Perot cavity [63].

Figure 5.1 shows the structure of the modulator and the circuit configuration used to implement noninterferometric optical subtraction. The modulator was fabricated using molecular beam epitaxial growth techniques explained in [46]. Quantum well layers are placed within the intrinsic region of a *p-i-n* diode structure to facilitate the application of an external electric field. A Fabry-Perot étalon is created by the *p*- and *n*-doped mirrors on the front and rear of the device, respectively. The cavity is undoped with 19 X 50 Å GaAs quantum wells and 75 Å $Al_{0.33}Ga_{0.67}As$ barriers. The rear mirror is composed of 19.5 pairs of AlAs/$Al_{0.33}Ga_{0.67}As$ quarter-wave layers with a calculated reflectivity of 98.8%. The front mirror is constructed with two similar pairs yielding 50.3% reflectivity. The reflectivity was measured using a white tungsten lamp and a 1/2 meter spectrometer. The reflectivity was

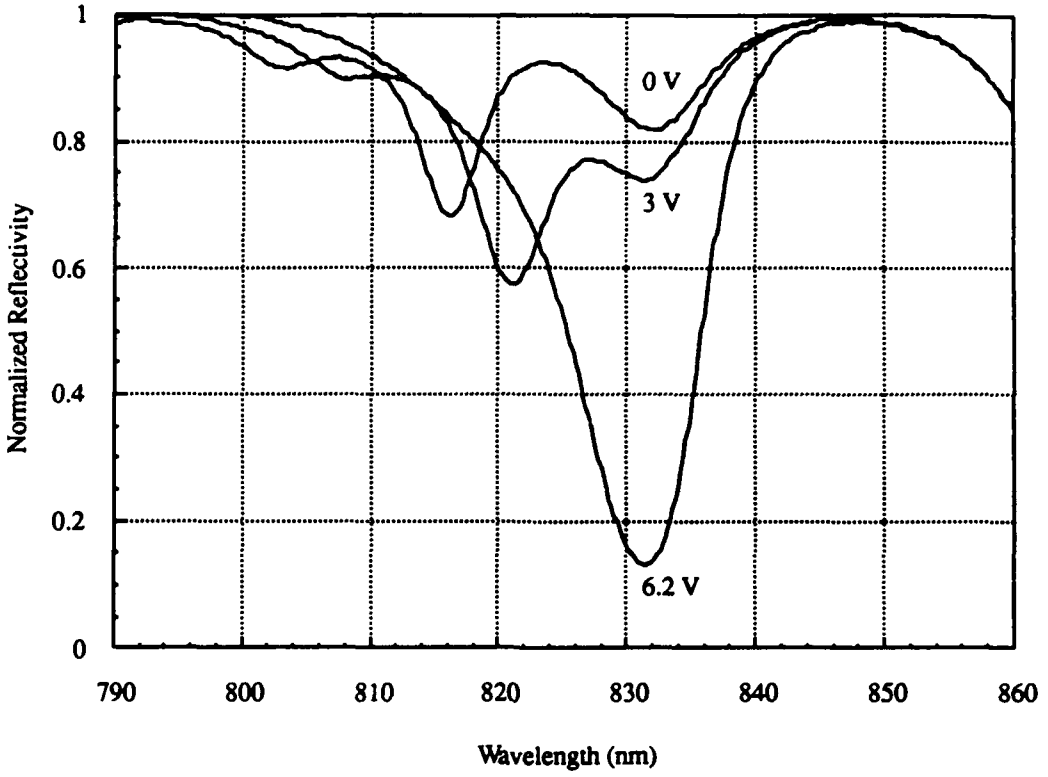

Figure 5.2: Normalized reflectivity versus wavelength.

then normalized to that of freshly evaporated gold and multiplied by the absolute reflectivity of gold to obtain the spectrum shown in Figure 5.2. At zero bias, the Fabry-Perot resonance can be seen at 831.5 nm, the heavy hole exciton at 817.0 nm, and the light hole exciton at 803.0 nm. As the bias voltage increases, the excitons red shift and approach the Fabry-Perot resonance of the cavity. Higher absorption yields lower reflectivity at the resonance wavelength. At 6.2 volts reverse bias, the heavy hole exciton and the Fabry-Perot resonance coincide, corresponding to the minimum reflectivity of the device. At this point, the reflectivity changes from 82% to 12%, yielding a contrast ratio of 6.8 and a maximum reflectivity change of 70%.

Recall from Chapter 3 that this method of noninterferometric subtraction requires negative feedback operation of the MQW modulator and a constant current source as the electronic bias circuit. Under these conditions, the absorbed power of

the modulator can be described by

$$P_a = \frac{h\nu}{\eta e} I_c, \tag{5.1}$$

and the resulting reflected power P_{ref} is described by the subtraction relation

$$P_{ref} = P_{inc} - P_a. \tag{5.2}$$

The operation of the modulator with a constant bias current is fairly simple to understand. The current I_c from the constant current source acts to charge the capacitance of the REAM diode, while the photocurrent I_p generated by the REAM acts to discharge it. If $I_p < I_c$, the voltage across the diode rises and since $dS/dV > 0$, I_p also rises. If however $I_p > I_c$, the voltage across the diode falls which in turn causes a decrease in I_c. Consequently, the equilibrium state corresponds to a stable operating point at which $I_p = I_c$.

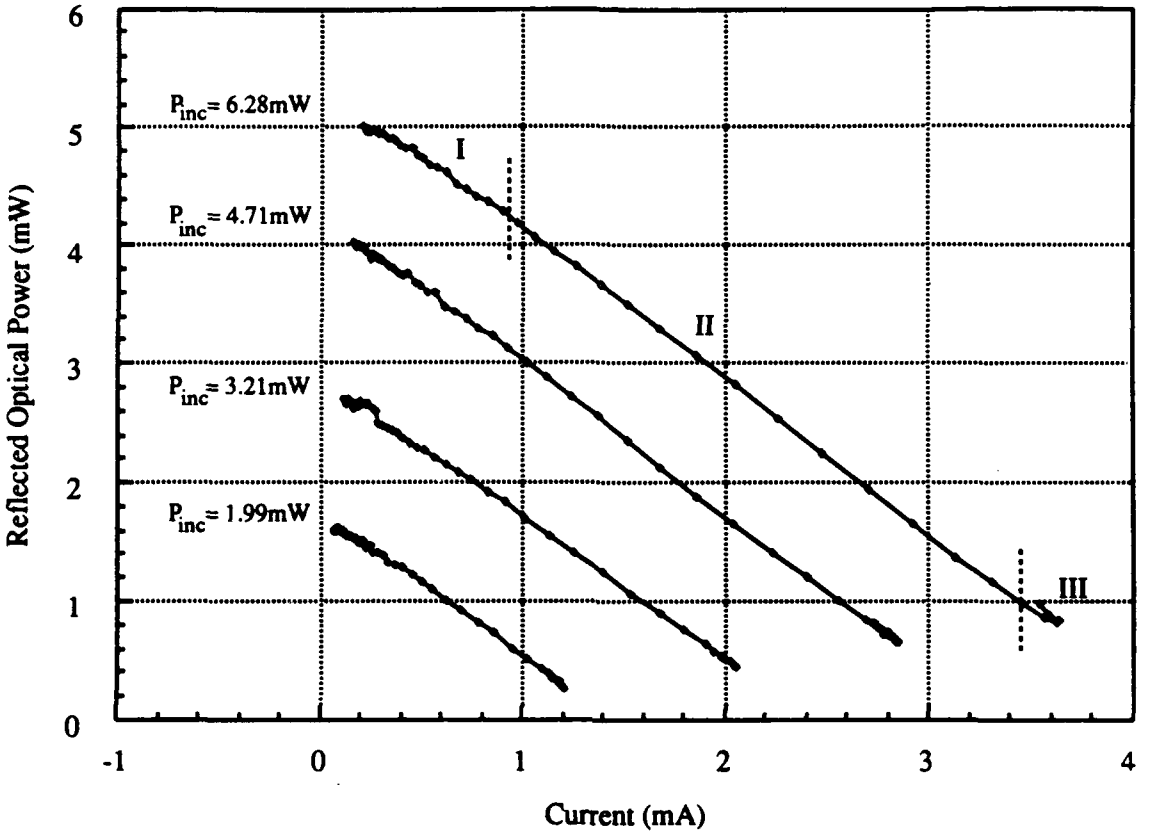

Figure 5.3: Reflected power versus control current. Regions I, II, and III represent the three operating regions of the modulator.

Figures 5.3 and 5.4 show measured results using an experimental configuration similar to that in Figure 5.1(a). A tunable Ti:sapphire laser and a constant current source were used to test the device operation. The laser was tuned to the Fabry-Perot mode of the device and focused onto the modulator using a single lens. In Figure 5.3, the incident power was held constant and the bias current was varied using the constant current source. Detailed analysis shows that each curve is comprised of three segments, shown for the P_{inc}= 6.28 mW curve by two vertical dashed lines. At low applied voltages, the field strength across the quantum wells is insufficient to sweep all of the carriers out of the wells and therefore, the quantum efficiency is less than unity, varying with applied voltage. This characteristic defines the first segment (I) of each curve. When the field reaches sufficient strength

to sweep out all of the carriers, corresponding to approximately 4 volts in this device, unity quantum efficiency is achieved and the second segment (II) which is linear according to Equation (5.1) is achieved. The electric field required to achieve unity quantum efficiency is approximately 160 kV/cm, which is not atypical for this type of modulator [64]. The third segment (III) corresponds to conditions under which the field continues to increase, the maximum absorption of the modulator is reached, and the device eventually breaks down. From this discussion and the theory of the QCSE, it becomes clear that the voltage required to achieve unity quantum efficiency is a function of the quantum well barrier height and therefore becomes a modulator design parameter. The experimental data was fit to a linear equation using least-squares linear regression techniques. Over the range for which the quantum efficiency was unity, the slope of each regression line corresponded to $-h\nu/e$, as expected from Equation (5.1). The correlation coefficient for each curve was 0.999, indicating nearly perfect linear regression. The insertion loss of the modulator was computed to be $17 \pm 1\%$ which corresponds within experimental error to the minimum absorption state of this device. The worst-case error, defined as the ratio of the absolute value of the maximum deviation of the measured data from that predicted by Equation (5.2) to the value predicted by Equation (5.2), was less than 0.5% over the operating range of the device for which η=1. By fitting a linear equation to the entire operating range of the device, the worst-case error was computed to be less than 2%.

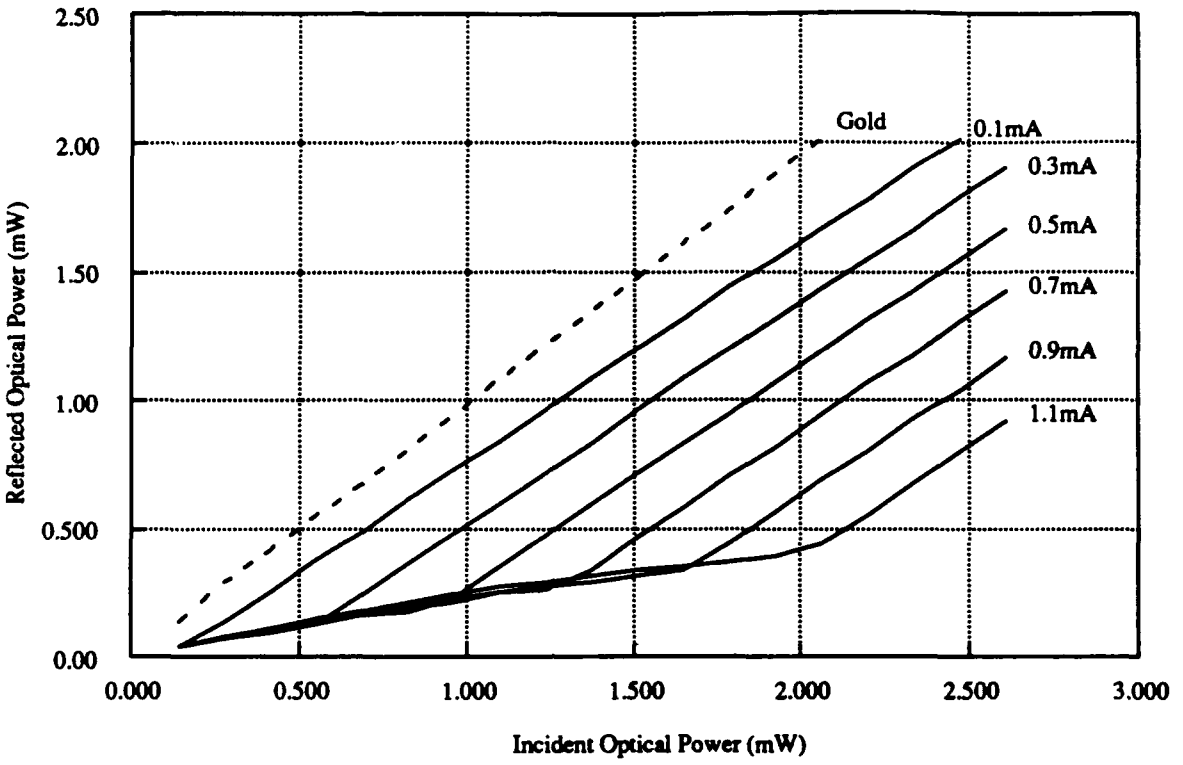

Figure 5.4: Reflected power versus input power as a function of constant bias current.

Figure 5.4 shows experimental results for P_{ref} versus P_{inc} for several different values of bias current. Here the reflectivity response of gold was included only as a reference. Each curve again consists of three linear segments. The lower segment corresponds to the case in which the maximum absorption of the modulator is reached, and insufficient photocurrent is generated to reach an equilibrium state. In this case, the slope of the segment corresponds to the high absorption state of the device, or a reflectivity of 18%. Ideally, the slope of this segment should be 12% reflectivity. The difference in slope occurs because the constant current source could provide no further increase in voltage and results in less than the 6.2 volts necessary for maximum modulator absorption. The upper segment corresponds to conditions under which an equilibrium state is reached, $I_p = I_c$, and Equation (5.1) is valid. The slope of this segment, although ideally 1, was measured to be 0.87 with deviations from unity being attributable to variations in quantum efficiency

and loss from the back mirror resulting from changes in cavity absorption. Over this segment, each curve was again fit to a linear equation with the resulting correlation coefficients being 0.9999. There is a final segment, not shown in Figure 5.4, in which the minimum absorption of the device is reached, no further increase in reflectivity is possible, and again equilibrium is unattainable. Here the slope corresponds to the minimum absorption of the device, or 82% reflectivity. From Figures 5.3 and 5.4 it is clear that we can achieve noninterferometric optical subtraction with extremely good linearity using this technique.

In the next section, this noninterferometric optical subtraction technique will be used as the building block to implement the negative feedback architecture for the first-order modulator. In this application, however, dynamic noninterferometric subtraction will be required since both P_{inc} and I_c are explicit functions of time.

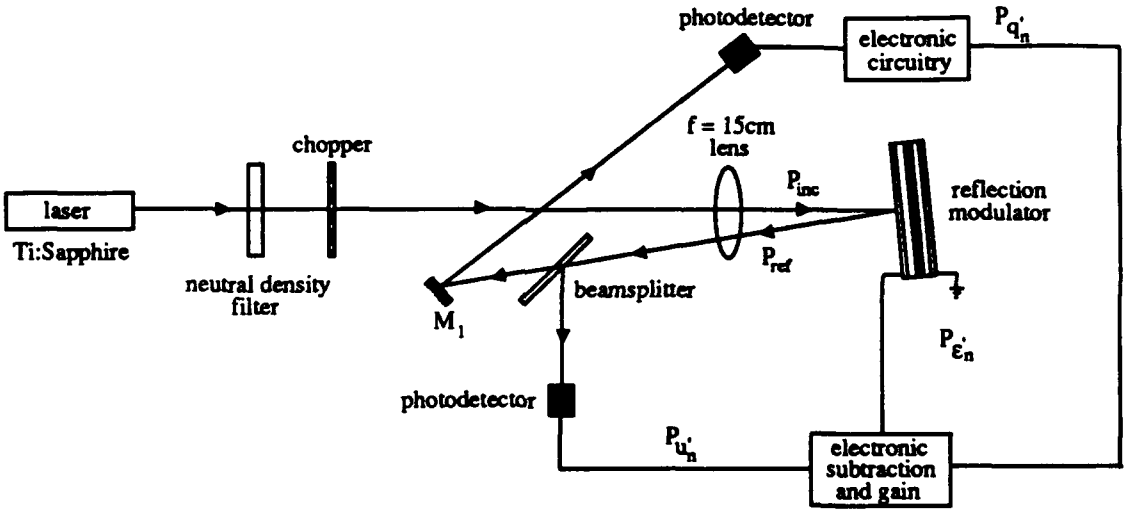

Figure 5.5: Experimental setup for the first-order noninterferometric modulator demonstration.

5.2 Experimental First-Order Modulator

The objective of this section is to demonstrate dynamic operation of the first-order noninterferometric optical modulator and compare key operating characteristics to those theoretically predicted in previous chapters. Since this is a proof-of-concept demonstration and we have previously experimentally demonstrated the operation of noninterferometric optical subtraction using a MQW modulator, only one of the subtraction nodes in the modulator will be implemented optically. Also, as a result of device availability, a photodetector and feedback electronic circuitry will be used to generate the one-bit optical quantization.

The experimental setup for the proof-of-concept demonstration of the first-order noninterferometric modulator is shown in Figure 5.5. In this configuration, $P_{inc} \equiv P_{x_n'}$, $P_{ref} \equiv P_{u_n'}$, the reflection modulator implements the noninterferometric optical subtraction $P_{x_n'} - P_{\varepsilon_n'} = P_{u_n'}$, electronic circuitry is used to implement the subtraction $P_{q_n'} - P_{u_n'} = P_{\varepsilon_n'}$, and a photodetector and electronic feedback circuitry generates the

necessary thresholding function.

In the actual demonstration, tunable Ti:sapphire laser operating at the Fabry-Perot mode of the modulator ($\lambda = 831.5$ nm) was used as the optical source. A variable neutral density filter provided the mechanism by which the constant input optical power level was manually adjusted. A mechanical chopper, operated between 300 Hz and 1 kHz, was used to sample the constant optical analog input. The sampled analog optical signal was focused onto the reflection modulator which implemented the first subtraction node in the modulator. A glass beamsplitter with a reflectivity of approximately 8% was used to develop the feedback signal $P_{w'_n}$ from the reflected optical signal P_{ref} for use in the second subtraction node. The remainder of P_{ref} was focused onto the photodetector which, along with the feedback electronic circuitry, performed the one-bit optical quantization. The signal $P_{e'_n}$ is an electronic current signal which controls the absorption of the reflection modulator and completes the feedback loop.

In this demonstration, the constant optical input was constrained to $P_{x'_n} \in [\Delta, 2\Delta)$ mW which corresponds to the no-overload range of the one-bit quantizer. The electronic circuitry and photodetector were calibrated to produce quantizer output states $P_{q'_n} \in \{\Delta, 2\Delta\}$ mW with a quantizer step size of $\Delta = 1$ mW and optical threshold $P_{th} = 3\Delta/2$ mW. The output of the quantizer, which is an electronic signal representing $P_{q'_n}$, is then directed to the electronic subtraction and gain circuitry which electronically implements the subtraction $P_{q'_n} - P_{w'_n} = P_{e'_n}$. Here a two-stage operational amplifier circuit is used to provide gain for the feedback signal $P_{w'_n}$, a differential amplifier implements the $P_{q'_n} - P_{w'_n}$ subtraction, and an operational amplifier is used as a voltage-to-current converter to produce $I_c \propto P_{e'_n}$.

The quantizer output data sequence was acquired using a digital storage oscilloscope. The time average of the quantizer output sequence is shown in Figure 5.6 for a constant optical biased input of $P_{x'_n} = 1.743$ mW. Figure 5.6 clearly shows the same modulator operating characteristics predicted in Chapter 2, and shown in Figure 2.7 with the exception of an offset. This offset, which equals 1.5 mW, corresponds to the $3\Delta/2$ bias offset used to ensure non-negative signal operation within the modulator.

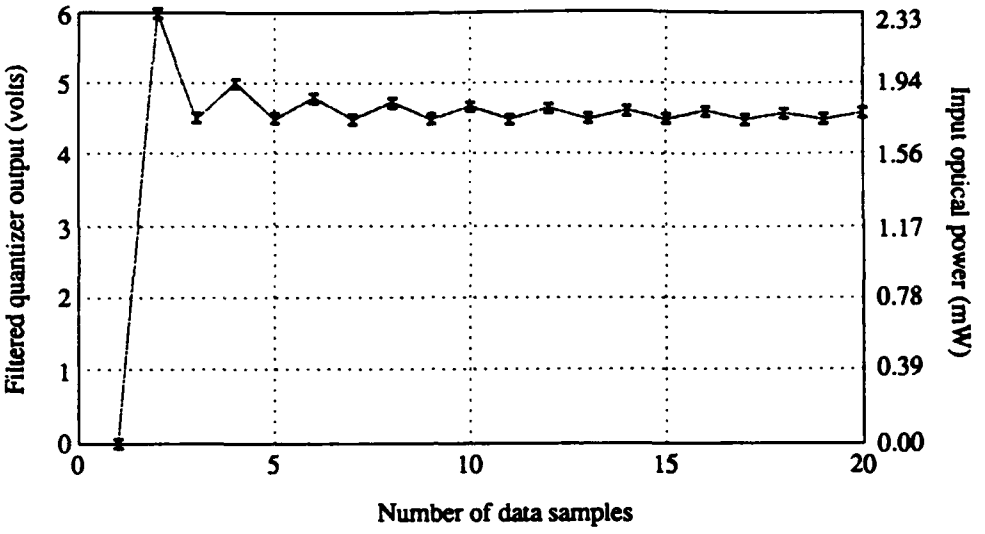

Figure 5.6: Sample average of the quantizer output sequence.

In order to get a quantitative estimate of the modulator performance, we define the worst-case error as

$$\sigma_{max} \equiv \max_{all\ n} \left\{ \frac{\left| P_{q_n} - \hat{P}_{q_n} \right|}{P_{q_n}} \right\}, \tag{5.3}$$

where P_{q_n} is the theoretically predicted value of the quantizer output power and $\hat{P}_{q_n}$ is the measured value. Over the entire operating range of the quantizer, we found that $\sigma_{max} \leq 2\%$. Most of this error was traced to amplifier noise and calibration errors in the electronic subtraction and gain circuitry. The experimental error was a result of linear errors in the subtraction operations and is therefore equivalent to the gain mismatch error discussed in Section 4.2. Since this error is linear, it can be accounted for in the modulator design and compensated in the postprocessor.

Another important characterization of modulator operation is the quantizer noise spectrum. Using the data acquired from the modulator output, we computed the power spectrum of the quantizer output sequence using the Fast Fourier Transform and compared it to the analytic results of Equation (4.23) for the case of an irrational dc input. The choice of an irrational dc input is justifiable since, if the input is selected at random using a continuous probability distribution, then

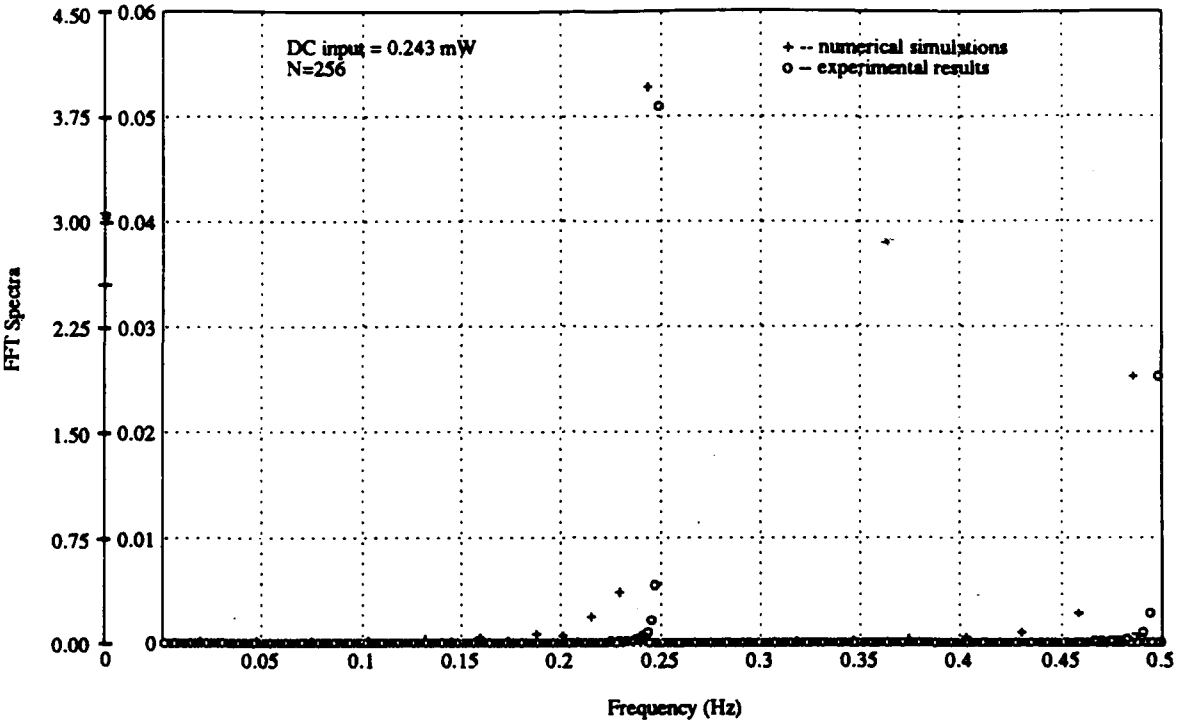

Figure 5.7: Power spectrum of the quantizer output sequence.

with probability one the resulting input will be an irrational number [57]. Figure 5.7 shows the power spectral density for both the theoretical and experimental first-order modulator quantizer output sequences for a constant unbiased analog input of 0.243 mW. The experimental power spectrum clearly shows the discreteness of the spectral tones which the theory predicts. Also, the difference between the theoretical and experimental plots corresponds to an error of approximately 2%, which agrees with the worst-case error computed earlier. The quantizer output power spectral density was computed for other constant optical input values and confirmed that the frequency of the spectral tones does in fact change with changes in the amplitude of the input as predicted by Equation (4.23).

From the results of this section, we can now make some general statements regarding the optical oversampled modulator. First, it is possible to implement dynamic noninterferometric optical subtraction with sufficient accuracy for use in

an optical oversampled modulator. Next, the linear errors associated with the noninterferometric optical subtraction result in gain mismatch errors in the modulator output, as predicted by Equation (4.4). These errors were shown to be independent of signal amplitude and can in principle be corrected in the digital postprocessor. As a result, no additional noise sources or errors in the noise shaping function are introduced by the optical implementation. The discrete power spectrum of the quantizer output sequence confirms the behavior of the quantizer error sequence. From these results, we are confident that a second-order optical modulator with a constant input will have a quantization noise spectrum with statistical characteristics consistent with a uniform white process. Finally, the experimental noninterferometric realization proved to be robust against thermal and vibrational variations which would typically render a free-space interferometric architecture unusable.

5.3 Summary

In this chapter, we experimentally demonstrated noninterferometric optical subtraction and dynamic operation of a first-order noninterferometric optical modulator. Noninterferometric optical subtraction using a reflection-type MQW modulator with a Fabry-Perot cavity was demonstrated for the first time and shown to be linear to within 0.5% of theoretical predictions, over the operating range for which the modulator achieved unity quantum efficiency. This subtraction technique was then used to implement the negative feedback architecture necessary for the first-order noninterferometric optical modulator. The modulator operated at sampling frequencies up to 1 kHz and demonstrated output sample average accuracy to within 2% of that predicted by theory. The experimental results of the first-order modulator operation also verified previous analytic predictions regarding the impact of linear subtraction errors on the modulator output and the discreteness of the quantization noise spectra.

Chapter 6

Multidimensional Extensions

UNTIL NOW, WE HAVE ADDRESSED ONE-DIMENSIONAL (1-D) TEMPORAL error diffusion coding as applied to oversampled A/D conversion. With the optical implementation came the possibility of two-dimensional (2-D) extensions using arrays of MQW modulators. In this chapter, we present multidimensional extensions of the basic optical oversampled A/D converter architecture developed previously and examine both 2-D temporal and 2-D spatial optical error diffusion applications. We also investigate the possibility and benefits derived from 3-D optical error diffusion coding.

Figure 6.1 shows a generic multidimensional extension of the first-order optical error diffusion coding architecture which uses MQW modulators as the fundamental optical devices. Here, u and v represent two orthogonal sampled spatial dimensions and n is the sampled time dimension. The input to the optical processor is a 2-D image, where the information about each image pixel is contained in the optical power $P_x(u, v, n)$. The first array of devices (I) consists of transmissive-type MQW modulators integrated with photodetectors to implement noninterferometric optical subtraction. This array of devices performs the subtraction operation of the first subtraction node in the temporal architectures described earlier. The second array of devices (II) consists of reflection-type symmetric-MQW modulators and implements the one-bit optical quantization function, pixel by pixel. The third array of

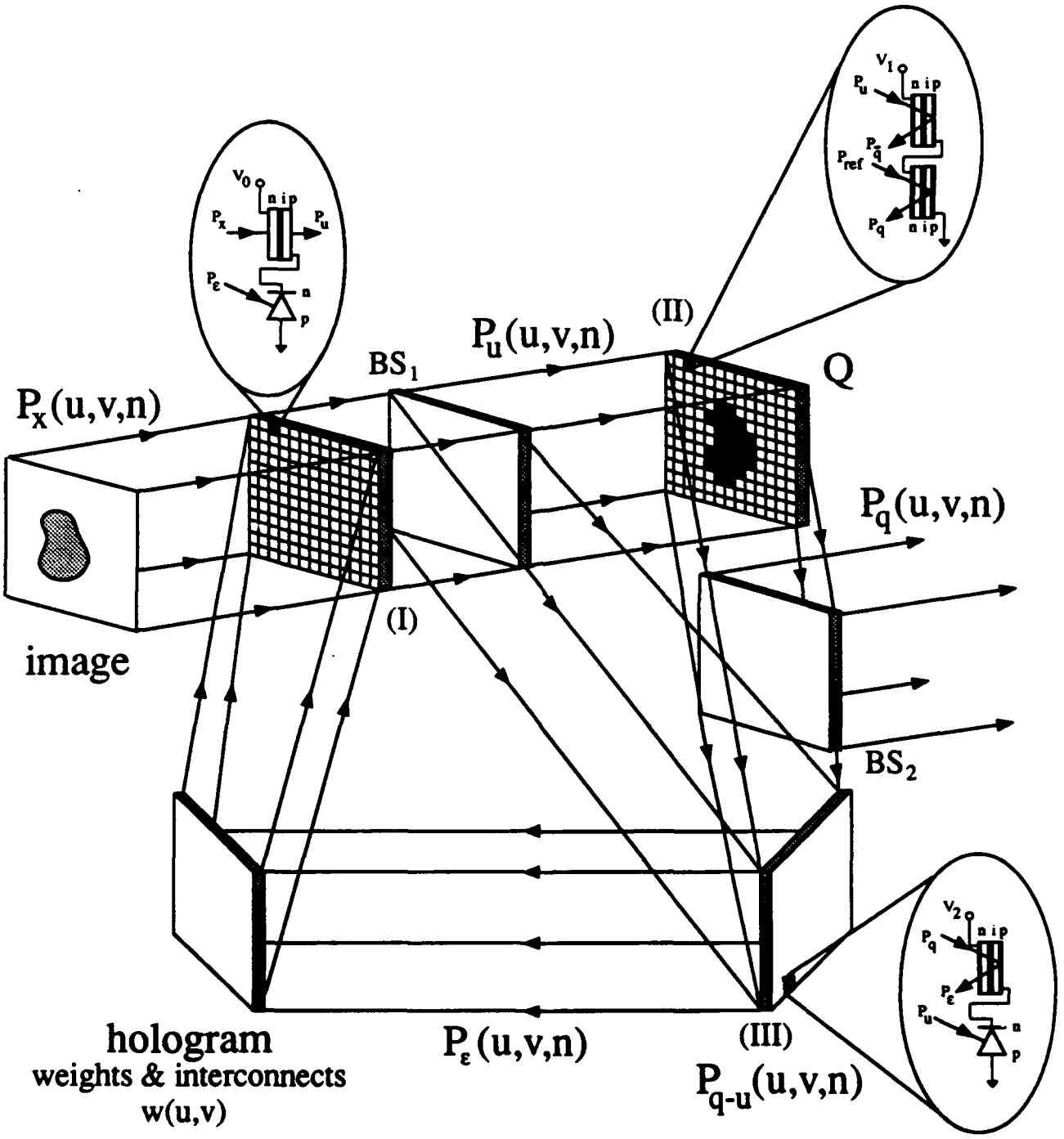

Figure 6.1: Multidimensional extension of optical error diffusion coding.

devices (III) is identical to the first, with the exception that reflection-type MQW modulators are used instead. This array of devices implements the feedback subtraction function. The hologram is fixed according to the particular application and implements the weights and interconnects required for the specific error diffusion algorithm. It is this hologram that determines whether 2-D temporal, 2-D spatial, or 3-D error diffusion coding is performed. Before proceeding, we note that the architecture presented in Figure 6.1 fits the framework of a symmetric (Hopfield-type) optical neural network [65]. Next, we present with the analysis and application of each of these cases.

6.1 Pixel-by-Pixel A/D Conversion

Optical oversampled pixel-by-pixel A/D conversion of a 2-D image is the most direct extension of the 1-D temporal optical oversampled A/D conversion presented previously. In this case, no spatial error diffusion is required of the hologram. In order to describe the weighting and interconnect operation of the hologram, we define new coordinate sets around the hologram. The input to the hologram is described by the coordinates (U, V), the hologram pixel location by (u, v), and the output of the hologram by (u, v). For all the applications considered here, (U, V) = (u, v). The weighting and interconnect operation of the hologram can, in general, be described by $w(\mathrm{u}, \mathrm{v}; u, v, n)$. Here, the optical information at the hologram coordinate (u,v) is weighted and interconnected to the coordinates (u,v). As in previous analyses, n represents the sampled temporal dimension.

2-D pixel-by-pixel A/D conversion, which diffuses errors only in the temporal dimension, can be described by (U, V) = (u, v) = (u, v) and $w(\mathrm{u}, \mathrm{v}; \mathrm{u}, \mathrm{v}) = 1$. The hologram interconnect and weight definitions are important for this application in the event that a reconfigurable hologram such as a computer generated hologram is used. If the pixel-by-pixel A/D architecture is designed as a special purpose optical processor, the hologram can be eliminated and the output from the third device array $P_e(\mathrm{u}, \mathrm{v}, \mathrm{n})$ can be interconnected directly to the first device array.

The operation of this 2-D optical oversampled A/D converter follows from a

direct extension of the 1-D temporal case presented in Chapter 3. The sampled analog signal $P_x(u,v,n)$ is incident on the 2-D array of transmissive-MQW modulators which perform the pixel-by-pixel noninterferometric optical subtraction $P_x(u,v,n) - P_e(u,v,n) = P_u(u,v,n)$. BS_1 directs a portion of $P_u(u,v,n)$ to the 2-D array of reflective-MQW modulators which perform the noninterferometric optical subtraction $P_q(u,v,n) - P_u(u,v,n) = P_e(u,v,n)$ and the remainder of $P_u(u,v,n)$ is incident on the quantizer array Q. A 2-D array of symmetric reflective modulators constitutes the quantizer array Q. BS_2 directs a portion of $P_q(u,v,n)$ to the 2-D array of reflective-MQW modulators and the balance to the modulator output. The output of the 2-D optical oversampled modulator corresponds to the output of BS_2. Here, the temporal data sequence from each individual pixel represents the high-rate, 1-bit, digital optical word which will be subsequently low pass filtered and decimated by the digital postprocessor. The hologram performs no spatial error diffusion but simply optically interconnects each pixel of the second array of reflection modulators to the corresponding pixel in the first array of transmissive modulators according to a one-to-one mapping.

This first-order 2-D optical modulator architecture can be extended to higher-order using techniques similar to those described in Chapter 2.

The usefulness and application of this 2-D extension is in the area of image preprocessing. If the input analog image is time-varying, this 2-D optical implementation can provide the front-end A/D processor by producing a high resolution pixel-by-pixel digital representation of the image. This 2-D digital representation of the input image can then be used as the input for subsequent digital signal processors or computers.

6.2 Digital Image Halftoning

Digital image halftoning is the process by which a gray scale image is reproduced on a bilevel printer or display such as a cathode ray tube (CRT). There are several different techniques by which digital image halftoning can be implemented [66, 67], with error diffusion coding [22] providing the most accurate digital representation of

the original image. Although error diffusion coding is desirable because it provides the best binary representation of the gray scale image, it is also the most computationally intensive. In an electronic realization, the algorithm scans through the image, line by line, and for each pixel, a binary quantization decision is made based on the intensity of the individual pixel and the weighted error from pixels in the diffusion region. Since this algorithm scans the image in a raster fashion, the error diffusion filter is necessarily causal and therefore can introduce undesirable visual artifacts. Also, substantial storage and signal processing are required for this implementation. By using a 2-D optical implementation of error diffusion coding, each pixel quantization decision can be computed in parallel and therefore the optical filter need not be causal. Visual artifacts resulting from the causality of the diffusion filter can therefore be eliminated. Also, the optical implementation should reduce the computational requirements while decreasing the total convergence time of the halftoning process.

If we use the same coordinate definitions as in the pixel-by-pixel A/D conversion case, the following constraints apply to the hologram for optical digital image halftoning:

$$\sum_{(u,v)\in N} w(\mathrm{u},\mathrm{v};u,v,n) = 1, \tag{6.1}$$

and

$$w(u,v;u,v,n) = 0, \tag{6.2}$$

where N defines the 2-D spatial region over which the error is to be diffused

$$\sqrt{|(u)|^2 + |(v)|^2} < N. \tag{6.3}$$

From these equations we can make some general comments about the hologram weights and interconnects in the digital image halftoning configuration. First, no temporal error diffusion occurs in the digital image halftoning error diffusion architecture as demonstrated by Equation (6.1). Equation (6.2) ensures that the hologram weights sum to one so that the exact value of the quantizer error is diffused. The region of diffusion N identifies a 2-D region over which the error is

to be diffused and is defined by the specific error diffusion filter and algorithm selected. Equation (6.3) mathematically defines a circular template which bounds this diffusion region.

The operation of the optical digital image halftoning architecture is similar to that described in Section 6.1 with the exception of the hologram functionality. Here, each pixel of the hologram assigns weights and interconnects according to the specific filter diffusion algorithm.

In the digital image halftoning case, the output from BS_2 constitutes the binary digital representation of the input image. No digital postprocessing is required as the human visual system performs the low pass filtering function when viewing the output on a bilevel display.

The digital image halftoning optical oversampled A/D converter provides several distinct advantages over electronic digital image halftoning. As a result of the 2-D nature of the optical implementation, a non-causal error diffusion filter can be implemented. The non-causal structure of the filter allows symmetric filters to be implemented which can reduce visual artifacts such as Moiré patterns from the final halftone image. Also, since each individual pixel quantization decision and the weighting and interconnect operations are performed in parallel, the speed of convergence to the optimum halftone image should be faster. Similarly, decreased convergence time suggests that an error diffusion filter with larger spatial dimensions can be utilized thereby reducing the individual pixel error and improving overall performance.

6.3 3-D Error Diffusion

By combining the techniques of temporal error diffusion and spatial error diffusion, it is also possible to implement 3-D optical error diffusion coding with the architecture shown in Figure 6.1. This 3-D error diffusion can be implemented simply by changing the functionality of the hologram. Here, the optical interconnections over the region N are complete. Also, the digital postprocessor will be required to perform *both* temporal *and* spatial low-pass filtering operations as the human

visual system will not be the principal recipient of the digital output.

At this juncture, we do not know the usefulness or specific applications of this 3-D optical error diffusion system. This will be a topic of future research.

6.4 Summary

In this chapter, we have discussed multidimensional extensions of optical error diffusion coding and focused primarily on two applications: pixel-by-pixel A/D conversion and digital image halftoning. By simply extending the 1-D temporal architectures presented in Chapters 2 and 3 to 2-D architectures, pixel-by-pixel oversampled A/D conversion can be implemented. Pixel-by-pixel A/D conversion can be used for real-time image processing applications where a continuous tone image first needs to be A/D converted and then subsequently processed using digital signal processing techniques. Digital image halftoning is the process by which a gray scale image is digitized for reproduction on a bilevel printer or display. The implementation of these two applications differs only in the functionality of the hologram which assigns weights and interconnects for the error diffusion process. In pixel-by-pixel oversampled A/D conversion, the hologram performs no spatial error diffusion but simply connects the incoming optical signal coordinates to the same outgoing coordinates with a weight of unity. In digital image halftoning, the hologram assigns the input optical signal coordinates to several output coordinates defined by the diffusion region N with weights according to the specific diffusion filter algorithm. In this case, the output of the 2-D optical oversampled modulator constitutes the final digital output since the human visual system performs the low pass filtering function usually associated with the digital postprocessor. The concepts used for pixel-by-pixel oversampled A/D conversion and digital image halftoning can also be extended to implement a 3-D optical error diffusion architecture. In this case, the hologram performs error diffusion in two spatial dimensions as well as the temporal dimension.

Chapter 7

Conclusion

THE IMPORTANCE OF A HIGH-SPEED A/D INTERFACE FOR USE WITH BOTH electronic and optical applications cannot be overstated. In this research, we have developed a new approach to optical A/D conversion based on oversampling and error diffusion coding techniques which can extend the resolution and conversion rates beyond those currently possible with other electronic or electrooptic A/D conversion techniques.

This new optical A/D conversion technique provides several advantages over other optical and electronic approaches. First, this new technique is simple and fundamentally device independent, requiring only optical quantizers, arithmetic operators, and common optical components. As optically bistable devices and sampling speeds become faster, the resolution and conversion rates of this optical converter can be expected to increase, as predicted in Chapter 2. The optical oversampled A/D converter can be operated in conjunction with high-speed optical sampling techniques which provide advantages in terms of decoupling of sampled and sampling signal as well as improved sampling precision. Recently, mode-locked semiconductor lasers have demonstrated 16 Gbps pulse rates with timing jitter less than 1 psec [68]. For the specific realizations which incorporate MQW modulators, these devices also provide some distinct advantages from which the optical oversampled A/D converter can profit. MQW switching speeds as fast as 33 psec

have been demonstrated [51], and theoretical speeds have been projected to approximately $1 - 5$ psec [69]. MQW modulators require low operating energy compared to previous optical devices with similar functionality. Also, because of the MQW modulator's 'three-terminal' operation, the need for critical biasing is eliminated, thereby providing an optical device with good input-output isolation characteristics [70]. The GaAs-based implementation is compatible with both diode lasers and electronics and suggests the possibility of system integration. Finally, the availability of arrays of MQW modulators [71] makes this method of A/D conversion particularly attractive for image processing applications.

There are several limitations associated with this new optical method of A/D conversion. The operation of the MQW modulators rely on shifts of the exciton absorption peak with applied electric field. These exciton peaks are narrow and therefore, for optimum performance, require an accurate and stable laser wavelength. Also, since the entire system is discrete-time, accurate timing synchronization is required.

Based on current device specifications [51, 72] and the results of this research, a two-stage optical oversampled A/D converter based on MQW devices should be capable of operating at a 16 Gbps sampling rate and providing resolution of 8 bits at a Nyquist conversion rate of 1 GHz. This performance assumes a cumulative matching error of $\pm$ 2.5 % and therefore a loss in $SQNR$ of 0.1 dB. Similarly, a two-stage converter operating at a sampling rate of 20 Gbps can provide 16 bits resolution at a conversion rate of 100 MHz. Here, the cumulative matching error is still assumed to be $\pm$ 2.5 %, but now corresponds to a 7.2 dB loss in $SQNR$. These performance estimates compare favorably with those of current electronic and electrooptic A/D converters. Bell *et al.* have recently described a hybrid electronic/electrooptic A/D converter, using demultiplexing techniques, which they predict can achieve resolution on the order of 6 bits at 4 GHz [13]. Current electronic technology supports approximately 8 bits resolution at 100 MHz for conventional Nyquist rate flash converters [4] and 12 bits at 1.5 MHz for oversampled converters [73].

7.1 Contributions

As a result of this research, a number of new concepts have been presented.

- The optical oversampled A/D converter proposed in this dissertation is the first optical converter of its type. It is the only optical A/D converter to date which uses optical quantization and therefore provides the potential for all-optical A/D conversion. All of the designs and analyses associated with this approach are new.

- The architecture of the optical oversampled modulator differs from other electronic oversampled converters such as $\Sigma\Delta$ converters in that an error diffusion coding architecture is used. As a result, the analyses of linear arithmetic errors, quantization noise spectra, and cascade error tolerances, although extensions of those used for $\Sigma\Delta$ modulators, are also new.

- Until now, MQW modulators have been used almost exclusively for optical interconnect and digital logic applications. As a result of this research, we have demonstrated the usefulness of MQW modulators to analog information processing applications.

- Previously, the concept of *self-linearized modulation* and *optical level shifting* using MQW modulators had been proposed for only static applications. We extended this concept to the application of noninterferometric optical subtraction in which both the incident optical light and the control current are explicitly time-varying signals.

- We experimentally demonstrated noninterferometric optical subtraction using a reflection electroabsorption modulator with a Fabry-Perot cavity and characterized the linearity and errors associated with this operation.

- Another novel use for dynamic noninterferometric optical subtraction which was demonstrated, but not discussed in this dissertation, is laser power stabilization [74].

- We experimentally demonstrated proof-of-concept operation of the first-order noninterferometric optical modulator using MQW modulators.
- We proposed the first multidimensional optical A/D converters for use in image A/D conversion and digital image halftoning applications.

7.2 Future Work

In this research, we have proposed the concept of an optical oversampled A/D converter and developed several methods by which to achieve its realization. We have focused primarily on the oversampled optical modulator while recommending methods for the implementation of the digital postprocessor. During the course of this research, we have identified several open issues which warrant further investigation.

One of the first logical extensions of this research is the experimental demonstration of a high-speed all-optical error diffusion modulator. In this research, we *demonstrated proof-of-concept* operation of the noninterferometric optical modulator only. Following the logical sequence of experimental progression, the next step would be a free-space demonstration of higher-speed operation using smaller and faster MQW devices. The ultimate goal is to realize a completely integrated optical oversampled modulator which operates at sampling rates in excess of 15 GHz.

In Chapter 3, we suggested the use of MQW modulators as the fundamental optical device for the implementation of the digital postprocessor. Recently, a significant effort has been made to develop digital optical logic using MQW modulators [53, 49, 75]. This basis for optical logic operations could be extended to the operations of full-adders and multi-bit storage registers, and used to build an optical digital postprocessor.

The analyses presented in Chapter 4 implicitly assumed generic noise sources which contributed to errors in the A/D conversion process. For a given optical architecture, noise sources and sources of error specific to the optical devices need to be quantified and compared to the errors used in these analyses.

The multidimensional extensions and applications discussed in Chapter 6 warrant further investigation. In the case of pixel-by-pixel A/D conversion, further

analysis of error sources peculiar to the arraying of the devices is necessary. Issues such as optical crosstalk, beam divergence, and cross coupling of the devices need to be investigated. For the 2-D optical digital image halftoning, more analysis is needed to quantify the amount of reduction in image artifacts resulting from the use of a non-causal error diffusion filter. Also, improvements in the convergence time resulting from fully-parallel operation need to be verified. The 3-D spatial and temporal error diffusion extension of the optical architecture provides the capability of 3-D error diffusion, something never before proposed.

Appendix A

Homomorphic Proof

IN THIS APPENDIX, WE ANALYTICALLY DEMONSTRATE THE HOMOMORPHIC relationship between the error diffusion coding and classic $\Sigma\Delta$ modulation architectures.

A.1 $\Sigma\Delta$ Modulator

Consider the ideal first order $\Sigma\Delta$ modulator shown in Figure A.1. We can describe the input to the quantizer as

$$u_n = x_{n-1} - q(u_{n-1}) + u_{n-1}. \tag{A.1}$$

The uniform binary quantizer assigns the digital output level according to

$$q(u_n) = \begin{cases} +\frac{\Delta}{2} & \text{if } u_n \geq 0 \\ \\ -\frac{\Delta}{2} & \text{otherwise} \end{cases} \tag{A.2}$$

where Δ is the quantizer step size and u_n is the quantizer input. We define the quantizer error as the difference between the output and input of the quantizer

$$\varepsilon_n \equiv q(u_n) - u_n. \tag{A.3}$$

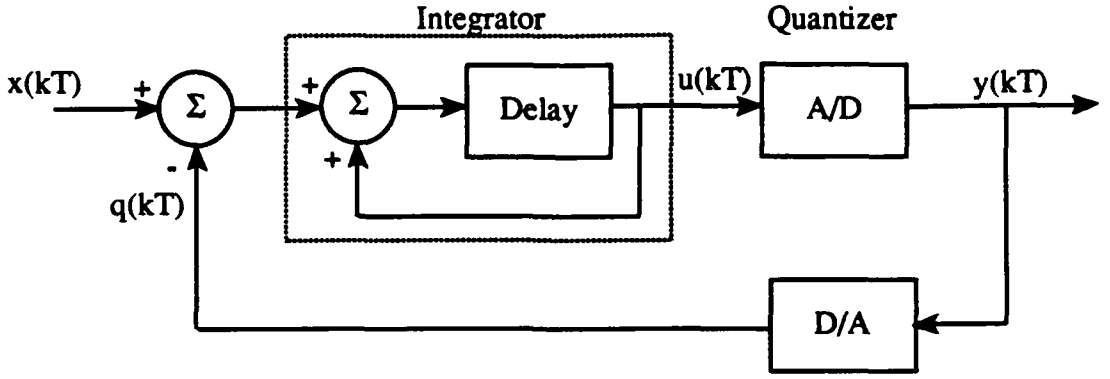

Figure A.1: Ideal first order ΣΔ modulator.

Rearranging Equation (A.1) using Equation (A.3) we have

$$q(u_n) = \underbrace{x_{n-1}}_{signal} - \underbrace{\varepsilon_n - \varepsilon_{n-1}}_{quantization\ error}. \tag{A.4}$$

If we assume the quantization noise is uniform and uncorrelated with the input, we can develop the noise shaping function for the modulator. The noise shaping function $H_N(z)$ of a ΣΔ modulator is the inverse of the transfer function $H(z)$ in the forward path of the modulator. For an N^{th} -order modulator with N integrators in the forward path, the noise shaping function is an N^{th} -order difference with the following transfer function:

$$H_N(z) = \frac{1}{H(z)} = (1 - z^{-1})^N. \tag{A.5}$$

For $N \geq 2$, a multi-loop ΣΔ architecture is required to achieve the noise shaping function described by Equation (A.5).

A.2 Error Diffusion Modulator

The recursive error diffusion modulator is shown in Figure A.2. If we assume $H_N(z) = 1$, then the input to the quantizer is

$$u_n = x_n - \varepsilon_{n-1}. \tag{A.6}$$

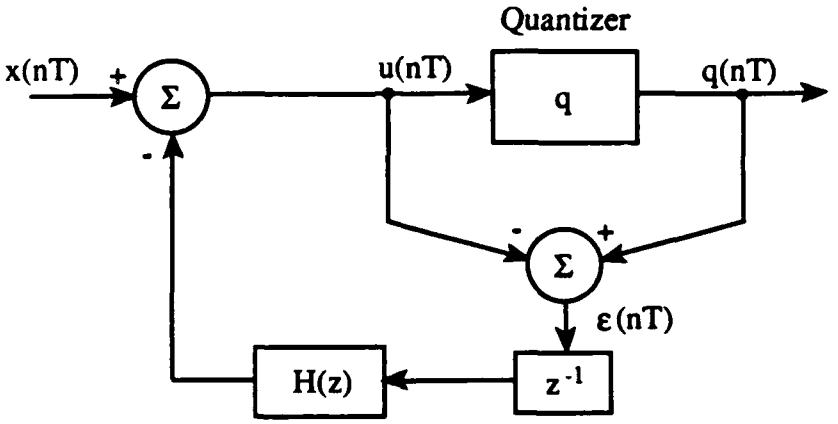

Figure A.2: Ideal N^{th}-order error diffusion modulator.

The quantizer output takes on the same states as defined in Equation (A.2) and the error is now an explicit variable in the architecture

$$\varepsilon_n = q(u_n) - u_n. \tag{A.7}$$

From these equations is is easy to show that

$$q(u_n) = \underbrace{x_n}_{signal} - \underbrace{\varepsilon_n - \varepsilon_{n-1}}_{quantization\ error}. \tag{A.8}$$

With the exception of the additional delay encountered by the signal in the $\Sigma\Delta$ modulator, Equations (A.4) and (A.8) are identical.

If we again make the assumption of uniform and uncorrelated quantization noise, we can develop the noise shaping function for the error diffusion modulator. Observe that $E(Z) = Q(z) - U(Z) = Q(z) - X(z) + H_N(z)E(z)z^{-1}$. The quantization error sequence $\hat{\epsilon}_n = q_n - x_n$ can be related to the quantizer error sequence $\epsilon_n = q_n - u_n$ through the transfer function

$$G(z) = \frac{\hat{E}(z)}{E(z)} = 1 - H_N(z)z^{-1} \tag{A.9}$$

where $\hat{E}(z)$ and $E(z)$ are the z -transforms of $\hat{\epsilon}_n$ and ϵ_n, respectively. If $H_N(z)$ is a

transversal filter with weights taken from the binomial coefficients

$$h_i = -(-1)^i \begin{pmatrix} N \\ i \end{pmatrix} \qquad \text{for i = 1, 2,..., N} \tag{A.10}$$

then Equations (A.5) and (A.9) produce identical noise shaping characteristics for a given N.

Appendix B

Interferometric Phase Detection

AS PART OF THE INTERFEROMETRIC MODULATOR, PHASE DETECTION IS required to accomplish the zero-threshold detection in the binary quantizer. Here we present the theory behind this development [76, 77].

Consider the interferometric configuration shown in Figure B.1. The two point sources $ae^{-(j\omega t+\phi)}$ and $ae^{-j\omega t}$ represent the quantizer input signal $u(nT)$ and the mutually coherent reference, respectively. The spatial dimensions d and f are selected according to physical implementation considerations. Let the intensity distribution at the object plane, x', be described as

$$f(x') = [a\delta(x'-d) + a\delta(x'+d)e^{\phi}]e^{-j\omega t}. \tag{B.1}$$

Using the Fourier transforming property of the lens, the distribution in the Fourier plane, x, is

$$F(x) = \int_{-\infty}^{\infty} a[\delta(x'-d) + \delta(x'+d)e^{\phi}]e^{-j\omega t}e^{-j\frac{2\pi}{\lambda f}xx'}dx'. \tag{B.2}$$

Define $K \equiv ae^{-j\omega t}$, then

$$\begin{aligned} F(x) &= K[e^{-j\frac{2\pi}{\lambda f}dx} + e^{j\frac{2\pi}{\lambda f}dx+\phi}] \qquad (B.3)\\ &= K[cos(\frac{2\pi}{\lambda f}dx) - jsin(\frac{2\pi}{\lambda f}dx+\phi) + cos(\frac{2\pi}{\lambda f}dx+\phi) + jsin(\frac{2\pi}{\lambda f}dx+\phi)]\\ &= K[2cos(\frac{2\pi}{\lambda f}dx+\frac{\phi}{2})cos(\frac{\phi}{2}) + j2cos(\frac{2\pi}{\lambda f}dx+\frac{\phi}{2})sin(\frac{\phi}{2})]. \end{aligned}$$

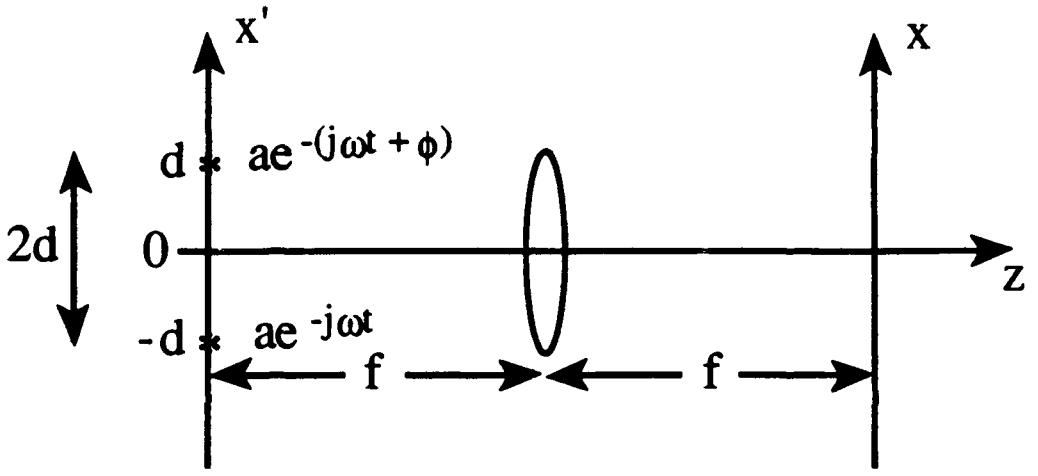

Figure B.1: Phase detector for interferometric modulator.

Next consider the real ($\Re$) and imaginary ($\Im$) parts of $F(x)$

$$\begin{aligned} \Re[F(x)] &= 2K\cos(\frac{2\pi}{\lambda f}dx + \frac{\phi}{2})\cos(\frac{\phi}{2}) \\ \Im[F(x)] &= 2K\cos(\frac{2\pi}{\lambda f}dx + \frac{\phi}{2})\sin(\frac{\phi}{2}). \end{aligned} \tag{B.4}$$

Described in phasor notation as

$$\begin{aligned} |F(x)| &= (\Re[F(x)]^2 + \Im[F(x)]^2)^{\frac{1}{2}} \\ &= 2K\cos(\frac{2\pi}{\lambda f}dx + \frac{\phi}{2}) \\ Arg[F(x)] &= tan^{-1}[tan(\frac{\phi}{2})] = \frac{\phi}{2}. \end{aligned} \tag{B.5}$$

And finally, the intensity distribution in the Fourier plane can be described as

$$\begin{aligned} I &= |[F(x)]|^2 \\ &= 2K\cos^2(\frac{2\pi}{\lambda f}dx + \frac{\phi}{2}) \\ &= K^2[1 + \cos(\frac{4\pi}{\lambda f}dx + \phi)]. \end{aligned} \tag{B.6}$$

The final representation in Equation (B.6) completely describes the operation of the phase detector in terms of phase difference between the two light distributions, the distances between the two sources, and the expected Fourier plane locations to observe peak intensity distributions. Knowing the physical dimensions of the phase detector and the wavelength of operation, the locations of the intensity maxima in the Fourier plane for both 0 and π phase differences can be computed using Equation (B.6).

Bibliography

[1] D. J. Knuth, *The TEXbook*. Reading, Massachusetts: Addison-Wesley, 1984.

[2] L. Lamport, LATEX: *A Document Preparation System*. Reading, Massachusetts: Addison-Wesley, 1986.

[3] T. Takemoto, M. Inoue, H. Sadamatsu, A. Matsuzawa, and K. Tsuji, "A fully parallel 10-bit A/D converter with video speed," *IEEE J. Solid-State Circuits*, vol. 17, no. 6, pp. 1133–1138, 1982.

[4] A. Yukawa, "A CMOS 8-bit high speed A/D converter IC," *IEEE J. Solid-State Circuits*, vol. 20, no. 3, pp. 775–779, 1985.

[5] H.-S. Lee, D. Hodges, and P. Gray, "A self-calibrating 15 bit CMOS A/D converter," *IEEE J. Solid-State Circuits*, vol. 19, no. 6, pp. 813–819, 1984.

[6] H. F. Taylor, "An electrooptic analog-to-digital converter," *Proc. IEEE*, vol. 63, no. 10, pp. 1524–1525, 1975.

[7] R. A. Becker, C. E. Woodward, F. J. Leonberger, and R. W. Williamson, "Wide-band electrooptic guided-wave analog-to-digital converters," *Proc. IEEE*, vol. 72, no. 7, pp. 802–819, 1984.

[8] Y. Tsunoda and J. W. Goodman, "Combined optical A/D conversion and page composition for holographic memory applications," *Applied Optics*, vol. 16, no. 10, pp. 2607–2609, 1977.

[9] L. J. Cutrona, *Optical and Electro-Optical Information Processing*, ch. 6. Cambridge, Massachusetts: MIT Press, 1965.

[10] H. K. Liu, "Coherent optical analog-to-digital conversion using a single halftone photograph," *Applied Optics*, vol. 17, no. 14, pp. 2181–2185, 1978.

[11] K. Takizawa and M. Okada, "Analog-to-digital converter: a new type using an electrooptic light modulator," *Applied Optics*, vol. 18, no. 18, pp. 3148–3151, 1979.

[12] N. N. Evtikheiv, D. I. Mirovitskii, N. V. Rostovtseva, and O. B. Serov, "Multilayer holographic functional element in an analog-to-digital converter," *Sov. J. Quantum Electron.*, vol. 16, no. 9, pp. 1180–1184, 1986.

[13] J. A. Bell, M. C. Hamilton, D. A. Leep, T. D. Morgan, H. F. Taylor, and Y.-H. Lee, "Extension of electronic A/D converters to multi-gigahertz sampling rates using optical sampling and demultiplexing techniques," in *Proceedings of the Twenty-Third Asilomar Conference on Signals, Systems and Computers* (Pacific Grove, California), November 1989.

[14] A. D. McAulay, "Optical analog-to-digital converter using optical logic and table look-up," *Optical Engineering*, vol. 29, no. 2, pp. 114–120, 1990.

[15] Y. Li and Y. Zhang, "Optical analog-to-digital conversion using acousto-optic theta modulation and table lookup," *Applied Optics*, vol. 30, no. 30, pp. 4368–4371, 1991.

[16] C. C. Cutler. Transmission systems employing quantization. U.S. Patent No. 2,927,962, 1960.

[17] H. Inose and Y. Yasuda, "A unity bit coding method by negative feedback," *Proc. IEEE*, vol. 51, no. 11, pp. 1524–1535, 1963.

[18] J. C. Candy, "A use of limit cycle oscillations to obtain robust analog-to-digital converters," *IEEE Trans. Commun.*, vol. 22, no. 3, pp. 298–305, 1974.

[19] J. C. Candy, Y. C. Ching, and D. S. Alexander, "Using triangularly weighted interpolation to get 13-bit PCM from a sigma-delta modulator," *IEEE Trans. Commun.*, vol. 24, no. 11, pp. 1268–1275, 1976.

[20] J. C. Candy, "A use of double integration in sigma-delta modulation," *IEEE Trans. Commun.*, vol. 33, no. 3, pp. 249–258, 1985.

[21] J. C. Candy, "Decimation for sigma-delta modulation," *IEEE Trans. Commun.*, vol. 34, no. 1, pp. 72–76, 1986.

[22] R. Floyd and L. Steinberg, "An adaptive algorithm for spatial gray scale," *SID 75 Digest*, vol. 36, pp. 35–37, 1975.

[23] D. Anastassiou, "Error diffusion coding for A/D conversion," *IEEE Trans. Circuits Syst.*, vol. 36, no. 9, pp. 1175–1186, 1989.

[24] S. K. Tewksbury and R. W. Hallock, "Oversampled, linear predictive and noise shaping coders of order N > 1," *IEEE Trans. Circuits Syst.*, vol. 25, no. 7, pp. 436–447, 1978.

[25] D. J. Goodman and L. J. Greenstein, "Quantizing noise of DM/PCM encoders," *Bell Syst. Tech. J.*, vol. 52, no. 2, pp. 183–204, 1973.

[26] R. M. Gray, "Quantization noise spectra," *IEEE Trans. Inform. Theory*, vol. 36, no. 6, pp. 1220–1244, 1990.

[27] E. F. Stikvoort, "Some remarks on the stability and performance of the noise shaper or sigma-delta modulator," *IEEE Trans. Commun.*, vol. 36, no. 10, pp. 1157–1162, 1988.

[28] K. Uchimura, T. Hayashi, T. Kimura, and A. Iwata, "VLSI A-to-D and D-to-A converters with multi-stage noise shaping modulators," in *Proceedings of ICASSP* (Tokyo, Japan), pp. 1545–1548, 1986.

[29] T. Hayashi, Y. Inabe, K. Uchimura, and T. Kimura, "A multi-stage delta-sigma modulator without double integration," in *Digest of Technical Papers of ISSCC* (San Fransisco, California), pp. 182–183, 1986.

[30] K. Uchimura, T. Hayashi, T. Kimura, and A. Iwata, "Oversampled A-to-D and D-to-A converters with multistage noise shaping modulators," *IEEE Trans. Acoust. Speech Signal Processing*, vol. 36, no. 12, pp. 1899–1905, 1988.

[31] E. B. Hogenauer, "An economical class of digital filters for decimation and interpolation," *IEEE Trans. Acoust. Speech Signal Processing*, vol. 29, no. 2, pp. 155–162, 1981.

[32] D. Goodman and M. Carey, "Nine digital filters for decimation and interpolation," *IEEE Trans. Acoustics, Speech and Signal Processing*, vol. 25, no. 2, pp. 121–126, 1977.

[33] J. C. Candy, B. A. Wooley, and O. J. Benjamin, "A voiceband codec with digital filtering," *IEEE Trans. Commun.*, vol. 29, no. 6, pp. 815–830, 1981.

[34] B. E. Boser, *Design and implementation of oversampled analog-to-digital converters.* PhD thesis, Stanford University, October 1988.

[35] B. Widrow, "A study of rough amplitude quantization by means of Nyquist sampling theory," *IRE Trans. Circuit Theory*, vol. 3, pp. 266–276, 1956.

[36] D. A. B. Miller, "Bistable optical devices: physics and operating characteristics," *Laser Focus*, pp. 79–84, April 1982.

[37] H. M. Gibbs, ed., *Optical bistability: controlling light with light.* New York: Academic Press, 1985.

[38] N. Peyghambarian and H. M. Gibbs, "Optical bistability for optical signal processing and computing," *Optical Engineering*, vol. 24, no. 1, pp. 68–73, 1985.

[39] D. A. B. Miller, D. S. Chemla, T. C. Damen, A. C. Gossard, W. Wiegmann, T. H. Wood, and C. A. Burrus, "Band-edge electroabsorption in quantum well structures: The quantum-confined Stark effect," *Phys. Rev. Lett.*, vol. 53, no. 22, pp. 2173–2177, 1984.

[40] D. A. B. Miller, "Optical bistability and differential gain resulting from absorption increasing with excitation," *J. Opt. Soc. Am. B*, vol. 1, no. 6, pp. 857–864, 1984.

[41] H. Haug, ed., *Optical nonlinearities and instabilities in semiconductors.* San Diego: Academic Press, 1988.

[42] S. Schmitt-Rink, D. S. Chemla, and D. A. B. Miller, "Linear and nonlinear optical properties of semiconductor quantum wells," *Adv. Phys.*, vol. 38, no. 2, pp. 89–188, 1989.

[43] D. A. B. Miller, D. S. Chemla, T. C. Damen, T. H. Wood, J. C. A. Burrus, A. C. Gossard, and W. Wiegmann, "The quantum well self-electrooptic effect device: optoelectronic bistability and oscillation, and self-linearized modulation," *IEEE J. Quantum Electron.*, vol. 21, no. 9, pp. 1462–1475, 1985.

[44] M. Whitehead, A. Rivers, G. Parry, J. S. Roberts, and C. Button, "Low-voltage multiple quantum well modulator with on:off ratio > 100:1," *Electron. Lett.*, vol. 25, no. 15, pp. 984–985, 1989.

[45] R. H. Yan, R. J. Simes, and L. A. Coldren, "Electroabsorptive Fabry-Perot reflection modulators with asymmetric mirrors," *IEEE Photon. Technol. Lett.*, vol. 1, no. 9, pp. 273–275, 1989.

[46] B. Pezeshki, D. Thomas, and J. S. Harris, Jr., "Optimization of modulation ratio and insertion loss in reflective electroabsorption modulators," *Appl. Phys. Lett.*, vol. 57, no. 15, pp. 1491–1493, 1990.

[47] K.-K. Law, R. H. Yan, L. A. Coldren, and J. L. Merz, "Self-electro-optic device based on superlattice asymmetric Fabry-Perot modulator with an on/off ratio > 100," *Appl. Phys. Lett.*, vol. 57, no. 13, pp. 1345–1347, 1990.

[48] R. A. Morgan, G. Livescu, L. M. F. Chirovski, M. W. Focht, and R. E. Leibenguth, "Fabry-Perot enhanced self-electro-optic-effect devices," *Optics Lett.*, vol. 17, no. 6, pp. 423–425, 1992.

[49] A. L. Lentine, H. S. Hinton, D. A. B. Miller, J. E. Henry, J. E. Cunningham, and L. M. F. Chirovsky, "Symmetric self-electro-optic effect device: Optical set-reset latch, differential logic gate, and differential modulator/detector," *IEEE J. Quant. Electron.*, vol. 25, no. 8, pp. 1928–1936, 1989.

[50] B. Pezeshki, D. Thomas, and J. S. Harris Jr., "Novel cavity design for high reflectivity changes in a normally off electroabsorption modulator," *Appl. Phys. Lett.*, vol. 58, no. 8, pp. 813–815, 1991.

[51] G. D. Boyd, A. M. Fox, D. A. B. Miller, L. M. F. Chirovsky, L. A. D'Asaro, J. M. Kuo, R. F. Kopf, and A. L. Lentine, "33 ps optical switching of symmetric self-electro-optic effect devices," *Appl. Phys. Lett.*, vol. 57, no. 18, pp. 1843–1845, 1990.

[52] K. Sasayama, M. Okuno, and K. Habara, "Coherent optical transversal filter using silica-based single mode waveguides for high-speed signal processing," *J. Lightwave Technol.*, vol. 9, no. 10, pp. 1225–1230, 1991.

[53] T. Doi and J. W. Goodman, "Application of MQW devices to Boolean logic operations," in *Optical Society of America 1991 Annual Meeting Technical Digest* (San Jose, California), November 1991.

[54] T. Doi. Personal communication.

[55] L. Williams III and B. A. Wooley, "Third-order cascaded sigma-delta modulators," *IEEE Trans. Circuits Syst.*, vol. 38, no. 5, pp. 489–498, 1991.

[56] R. M. Gray, "Oversampled sigma-delta modulation," *IEEE Trans. Commun.*, vol. 35, no. 5, pp. 481–489, 1987.

[57] R. M. Gray, "Spectral analysis of quantization noise in a single-loop sigma-delta modulator with dc input," *IEEE Trans. Commun.*, vol. 37, no. 6, pp. 588–599, 1989.

[58] R. M. Gray, W. Chou, and P. W. Wong, "Quantization noise in a single-loop sigma-delta modulator with sinusoidal inputs," *IEEE Trans. Commun.*, vol. 37, no. 9, pp. 956–968, 1989.

[59] W. Chou, P. W. Wong, and R. M. Gray, "Multistage sigma-delta modulation," *IEEE Trans. Inform. Theory*, vol. 35, no. 4, pp. 784–796, 1989.

[60] S. H. Ardalan and J. J. Paulos, "An analysis of nonlinear behavior in delta-sigma modulators," *IEEE Trans. Circuits Syst.*, vol. 34, no. 6, pp. 593–603, 1987.

[61] C. Wolff and L. R. Carley, "Modeling the quantizer in high-order delta-sigma modulators," in *Proceedings of ISCAS* (Espoo, Finland), June 1988.

[62] L. Williams III, B. E. Boser, E. Liu, and B. A. Wooley, *MIDAS User Manual, version 2.0.* Stanford University, Stanford, California: Integrated Circuits Laboratory, 1989.

[63] B. Pezeshki, D. Thomas, and J. S. Harris, Jr., "Optimization of reflection electro-absorption modulators," in *Proceedings of SPIE* (Aachen, Federal Republic of Germany), November 1990.

[64] K. Hu, L. Chen, A. Madhukar, P. Chen, K. C. Rajkumar, K. Kaviani, Z. Karim, C. Kyriakis, and A. R. Tanguay, Jr., "High contrast ratio asymmetric Fabry-Perot reflection light modulator based on GaAs/InGaAs multiple quantum wells," *Appl. Phys. Lett.*, vol. 59, no. 9, pp. 1108–1110, 1991.

[65] D. W. Tank and J. J. Hopfield, "Simple "neural" optimization networks: A/D converter, signal decision circuit, and linear programming circuit," *IEEE Trans. Circuits Syst.*, vol. 33, no. 5, pp. 533–541, 1986.

[66] J. F. Jarvis, C. N. Judice, and W. J. Ninke, "A survey of techniques for the display of continuous-tone pictures on bilevel displays," *Computer Graphics and Image Processing*, vol. 5, pp. 13–40, 1976.

[67] R. A. Ulichney, *Digital Halftoning.* Cambridge, Massachusetts: MIT Press, 1987.

[68] J. E. Bowers, P. A. Morton, A. Mar, and S. W. Corzine, "Actively mode-locked semiconductor lasers," *IEEE J. Quantum Electron.*, vol. 25, no. 6, pp. 1426–1439, 1989.

[69] D. A. B. Miller. Personal communication.

[70] D. A. B. Miller, "Quantum-well self-electro-optic effect devices," *Optical Quantum Electron.*, vol. 22, pp. S61–S98, 1990.

[71] A. L. Lentine, F. B. McCormick, R. A. Novotny, L. M. F. Chirovsky, L. A. D'Asaro, R. F. K. J. M. Kuo, and G. D. Boyd, "A 2kbit array of symmetric self-electrooptic effect devices," *IEEE Photon. Technol. Lett.*, vol. 2, no. 1, pp. 51–53, 1990.

[72] I. Kotaka, K. Wakita, O. Mitomi, H. Asai, and Y. Kawamura, "High-speed InGaAlAs/InAlAs multiple quantum well optical modulators with bandwidths in excess of 20 GHz at 1.55 μm," *IEEE Photon. Technol. Lett.*, vol. 1, no. 5, pp. 100–101, 1989.

[73] B. P. Brandt, *Oversampled analog-to-digital conversion.* PhD thesis, Stanford University, August 1991.

[74] B. L. Shoop, B. Pezeshki, J. W. Goodman, and J. S. Harris, Jr., "Laser-power stabilization using a quantum-well modulator," *IEEE Photon. Technol. Lett.*, vol. 4, no. 2, pp. 136–139, 1992.

[75] A. L. Lentine, H. S. Hinton, D. A. B. Miller, J. E. Henry, J. E. Cunningham, and L. M. F. Chirovsky, "Symmetric self-electro-optic effect device: Optical set-reset latch," *Appl. Phys. Lett.*, vol. 52, no. 17, pp. 1419–1421, 1988.

[76] M. Born and E. Wolf, *Principles of Optics, Sixth Edition.* Elmsford, New York: Pergamon Press, 1991.

[77] J. W. Goodman, *Introduction to Fourier Optics.* New York: McGraw-Hill, 1968.